2013

# Modeling Cortical Folding Patterns of the Brain Using a Growing Domain

Gregory Toole

THE FLORIDA STATE UNIVERSITY

COLLEGE OF ARTS AND SCIENCES

# MODELING CORTICAL FOLDING PATTERNS OF THE BRAIN USING A GROWING DOMAIN

By

GREGORY TOOLE

A Dissertation submitted to the
Department of Mathematics
in partial fulfillment of the
requirements for the degree of
Doctor of Philosophy

Degree Awarded:
Spring Semester, 2013

Gregory Toole defended this dissertation on March 18, 2013.

The members of the supervisory committee were:

Monica K. Hurdal
Professor Directing Dissertation

Oliver Steinbock
University Representative

Richard Bertram
Committee Member

Nick Cogan
Committee Member

Brian Ewald
Committee Member

The Graduate School has verified and approved the above-named committee members, and certifies that the dissertation has been approved in accordance with the university requirements.

*For my beautiful wife, Jennifer*

# ACKNOWLEDGMENTS

First and foremost, I would like to thank my major professor, Dr. Monica Hurdal. I couldn't have asked for a better advisor. I have appreciated her advice, assistance, and support more than any words I can put here could ever describe. Thank you for helping me make this dream a reality.

I would like to thank my committee members: Dr. Richard Bertram, Dr. Nick Cogan, Dr. Brian Ewald, and Dr. Oliver Steinbock. Thank you for all your time, assistance, and encouragement throughout my graduate career.

I would like to thank Dr. Penelope Kirby for helping me become the teacher that I am today. Thanks for always being there to give me teaching tips and showing me how to handle all the interesting challenges that being a college math instructor presents.

I would like to thank Josh Bowen as well as all the rest of the FSU Math Department staff for lending a helping hand throughout my time as a graduate student.

I would like to thank Danielle Cusmano and Celes and Brent Woodruff for being the best friends anyone could ever have. You guys are like family to me.

Thank you to all the other friends and family that have been there for me during my time at Florida State.

Last but not least, I would like to thank my amazing wife, Jennifer, for her incredible love and support during this whole process, and for always being there to lend an ear or deliver a Krispy Kreme donut when I needed someone to lean on.

# TABLE OF CONTENTS

# LIST OF TABLES

# LIST OF FIGURES

# LIST OF ABBREVIATIONS

ATH – axonal tension hypothesis
BVM – Barrio-Varea-Maini
CIMA – chlorite-iodide-malonic acid
CNS – central nervous system
CP – cortical plate
CSF – cerebrospinal fluid
GA – gestational age
GIP – global intermediate progenitor
GM – germinal matrix
IPC – intermediate progenitor cell
IPH – intermediate progenitor hypothesis
IPM – intermediate progenitor model
IZ – intermediate zone
LV – lateral ventricle
MRI – magnetic resonance imaging
NRS – Norman-Roberts syndrome
PMG – polymicrogyria
PNS – peripheral nervous system
RGC – radial glial cell
RUH – radial unit hypothesis
SVZ – subventricular zone
VZ – ventricular zone

# ABSTRACT

The brain is one of nature's greatest mysteries. The mechanism by which the folds of the brain's cerebral cortex, called gyri (hills) and sulci (valleys), are formed remains unknown. Existing biological hypotheses that attempt to explain the underlying mechanism of cortical folding conflict. Some hypotheses, such as the Intermediate Progenitor Model, emphasize genetic chemical factor control. Others, such as the Axonal Tension Hypothesis, emphasize the influence of physical tension due to axonal connections.

To bring mathematics into this debate, this dissertation presents two biomathematical models of cortical folding that utilize a Turing reaction-diffusion system on an exponentially or logistically growing prolate spheroidal domain. These models are used to investigate the validity of the Intermediate Progenitor Model, thereby investigating the role of genetic chemical factor control of the development of cortical folding patterns. We observe that the presence of domain growth drives the patterns generated by our growing prolate spheroidal Turing systems to become transient. An exponentially growing prolate spheroidal domain generates a pattern that continually evolves, while a logistically growing prolate spheroidal domain generates a pattern that evolves while the domain is growing but then converges to a final pattern once the domain growth asymptotically stops.

Patterns generated by the model systems represent genetic chemical prepatterns for self-amplification of intermediate progenitor cells, which may be correlated to cortical folding patterns according to the Intermediate Progenitor Model. By altering system parameters, we are able to model diseases of cortical folding such as polymicrogyria where the cortex possesses too many folds as well as diseases where the cortex has too few cortical folds such as Norman-Roberts Syndrome (microcephalic lissencephaly) and normocephalic lissencephaly. Our ability to model such a variety of diseases lends support to the role of genetic control of cortical folding pattern development and therefore to the Intermediate Progenitor Model.

# CHAPTER 1

# INTRODUCTION

> "In this section a mathematical model...will be described. This model will be a simplification and an idealization, and consequently a falsification. It is to be hoped that the features retained for discussion are those of greatest importance in the present state of knowledge." *–A.M. Turing, The Chemical Basis of Morphogenesis, 1952*

Though many advances in biology have been made over the course of human history, few things remain as mysterious as the human brain. In particular, the mechanism by which the folds of the cerebral cortex, called gyri (hills) and sulci (valleys), are formed remains unknown. Existing biological hypotheses that try to explain the underlying mechanism of cortical folding disagree with one another; some emphasize the role of genetic factors [45], while others highlight the importance of axonal tension [22]. Furthermore, it is extremely difficult to perform cortical folding experiments on living humans, as many of the important events of cortical folding take place during fetal development [28].

To bring mathematics into this debate, this dissertation presents biomathematical models of cortical folding that incorporate an exponentially or logistically growing prolate spheroidal domain into a Turing reaction-diffusion system. We utilize the Intermediate Progenitor Model, a biological hypothesis describing a possible genetically-controlled mechanism of cortical folding, as the biological foundation of our biomathematical models [45]. A growing domain Turing system model of cortical folding is more realistic than previous static domain Turing system models of cortical folding [13, 86], as it captures the growth that naturally occurs as the brain develops. Using exponential domain growth echoes the growth of a biologically relevant brain structure, while employing logistic growth provides a way to include domain growth in a Turing model of cortical folding in an overall more biologically realistic fashion.

Chapter 2 discusses brain anatomy and cells of the central nervous system which are key to cortical development. Several biological hypotheses and mathematical models of cortical development and folding are presented. In Chapter 3, Turing reaction-diffusion systems on static and growing domains are introduced. The key properties and characteristics of a Turing system are presented. Different types of Turing system reaction kinetics and the intuition behind Turing systems' pattern-generating capabilities are discussed. Lastly, a prolate spheroidal domain is incorporated into the growing domain Turing system framework.

Chapters 4 and 5 investigate the pattern-generating behavior of a Turing system on a growing prolate spheroidal domain under different types of domain growth. Numerical simulations are conducted to visualize the evolution of the generated patterns. Chapter 4 incorporates exponential domain growth into the system and uses linear stability analysis to derive mathematical conditions which ensure that an exponentially growing Turing system can generate patterns. Chapter 5 incorporates logistic domain growth into the system to further illustrate the role of domain growth in a Turing system's pattern-generating behavior.

Chapter 6 utilizes the results of Chapters 4 and 5 to construct two biomathematical Turing system models of cortical folding on growing prolate spheroidal domains. Motivation for the models and the link between the math and the biology are discussed. The models' ability to capture various diseases of cortical folding is also demonstrated. Finally, Chapter 7 concludes the investigation by discussing challenges and future directions for biomathematical Turing research of cortical folding patterns.

In sum, this dissertation demonstrates that a growing domain Turing system can generate patterns that can serve as a genetic chemical prepattern for the development of cortical folds in the brain, lending support to both the role of genetic morphogen control in cortical folding pattern development and the Intermediate Progenitor Model. Along the way, we will observe that the incorporation of domain growth into a Turing system induces a key change in the system's pattern generating behavior: while static domain Turing systems generate a convergent pattern, domain growth drives the system to produce transiently evolving patterns. Exponentially growing domains generate continuously evolving patterns, while logistically growing domains generate a pattern that rapidly evolves but then converges to a final pattern. The research presented in this dissertation could serve as a key stepping stone in the evolution of mathematical modeling of cortical folding patterns, establishing a strong foundation for future biomathematical investigations into the subject.

# CHAPTER 2

# THEORIES AND MODELS OF CORTICAL FOLDING

## 2.1 Neuroanatomy

The nervous system is intricately composed of many unique pieces which work together to transmit information throughout the body via electrical impulses [80]. The nervous system can be divided into the central nervous system (CNS), consisting of the brain and spinal cord, and the peripheral nervous system (PNS), which consists of the nerves that relay information back and forth between the CNS and the rest of the body [80]. The following sections will outline some of the major features of the CNS, many of which are of critical importance in the process of cortical development and folding.

### 2.1.1 The Brain: Major Macroscopic Features

At the macroscopic level, the brain is composed of the cerebrum, brain stem, and cerebellum [80]. The cerebrum is divided into two hemispheres (left and right), and the outer layer of the two hemispheres is called the cerebral cortex. The cerebral cortex, which consists of six layers of neurons [30], is intricately folded into gyri (hills) and sulci (valleys) (see Figure 2.1a). Each hemisphere is divided into four lobes, named the frontal, parietal, occipital, and temporal lobes (see Figure 2.1b), based on their anatomical locations and specialized functions. A structure called the corpus callosum provides connections between neurons in opposite hemispheres (see Figure 2.1c) [80].

### 2.1.2 The Ventricular System

The ventricular system of the brain is composed of the two lateral ventricles (LVs) as well as the third and fourth ventricles (see Figure 2.2). Early in neurogenesis, which in humans occurs during gestational weeks 7 to 18, the LVs are approximately prolate spheroidal in shape as they account for nearly all the volume of the prolate spheroidal cerebral hemispheres [26, 38, 75] (see Figure 2.3). At maturity, the LVs are c-shaped with posterior horns that stretch backwards toward the occipital lobes (see Figure 2.4). Inside the ventricles is cerebrospinal fluid (CSF), which flows throughout the CNS [80]. CSF is generated within the ventricles by structures called choroid plexuses (see Figure 2.2). CSF plays many roles in the CNS, including removal of toxins from the brain and provision of

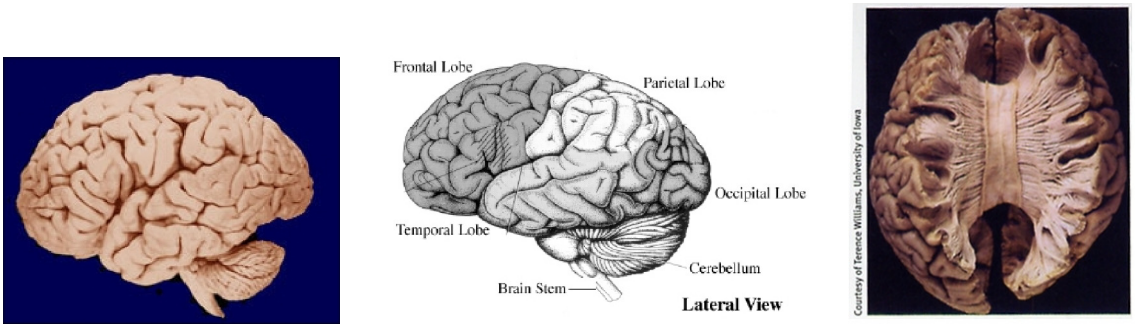


(a) (b) (c)

Figure 2.1: The human brain. (a) The cerebral cortex is folded into many gyri and sulci. Figure from [69]. (b) The brain is divided into frontal, parietal, occipital, and temporal lobes. Figure adapted from [104]. (c) Communication between neurons in the left and right hemispheres of the brain is provided by the corpus callosum. Figure from [60].

nutrients to the brain. CSF also provides the brain with physical protection, forming a cushion-like barrier between the brain and skull [80].

The walls of the developing LVs are lined by the ventricular zone (VZ) and subventricular zone (SVZ) [45, 66, 74]. Both the VZ and SVZ are layers of proliferative cells that play a role in cortical development [45, 66, 74]. Continuing radially outward from the inside of the LVs, one passes from the VZ to the SVZ. In particular, the SVZ serves as the site of self-amplification of intermediate progenitor cells (IPCs), which will be further discussed in Section 2.2.

### 2.1.3 Germinal Matrix

During development, the SVZ produces a structure called the germinal matrix (GM), which contains progenitors of neurons and glial cells [2]. The literature uses the term GM to either represent the part of the SVZ located ventrolateral to the LV and extending along the lateral wall of the LV [2, 44], or as a collective synonym for the VZ and SVZ, referring to the mass of germ cells that give rise to cortical neurons [33]. Regardless, the GM is a key component in neurogenesis. The GM appears at 7 weeks gestational age (GA) and exists only until term [2, 44]. Growth of the GM has been investigated with magnetic resonance imaging (MRI) and computational reconstruction of 3-D images of the developing brain [44] (see Figure 2.5). MRIs were obtained from the brains of 13 legally aborted fetuses ranging from 7-28 weeks GA. The fetuses died from reasons other than CNS disease or body malformation, so their brains were viable representatives of human development. GM volume was found to increase exponentially from 11-23 weeks GA and then decrease rapidly from weeks 25-28 GA. LV volume was found to linearly increase up to week 23 GA, then gradually decrease (see Figure 2.4) [2, 44].

During weeks 5-25 GA, IPCs and other neural progenitors proliferate and generate neurons, which also migrate to the developing cortex during this period (see Figure 2.6) [35, 45, 51, 75, 103]. Furthermore, cortical folding is considered to begin at week 10, 14,

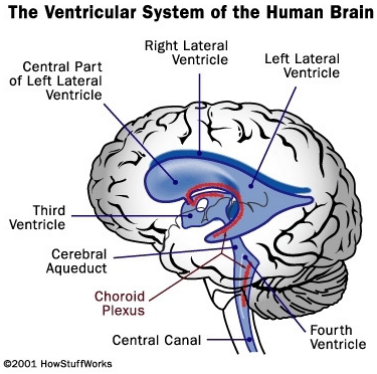


Figure 2.2: The ventricular system. The human ventricular system is composed of the lateral ventricles, third ventricle, and fourth ventricle. Cerebrospinal fluid is produced by choroid plexuses, shown in red. Figure from [27].


(a)

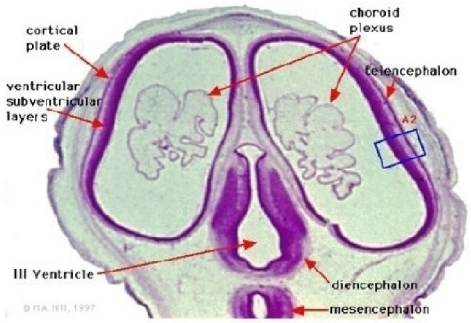


(b)

Figure 2.3: Shape of lateral ventricles early in development. (a) The developing cerebral hemispheres are prolate spheroidal in shape at 48 days GA. Figure adapted from [26]. (b) The LVs account for nearly the entire volume of the developing cerebral hemispheres at 54-56 days GA. The LVs are thus prolate spheroidal in shape at this time of development. Figure from [38].


Figure 2.4: Growth of brain, germinal matrix, and ventricular system. Growth of the brain is shown from 7 weeks gestational age (GA) to 28 weeks GA (top). The GM (middle, shown in orange) grows exponentially from weeks 11-23 GA but then rapidly loses volume beginning at week 25 GA. The LVs (bottom, shown in blue) grow linearly before their volume reaches a maximum near week 23 GA. Early in development, the LVs are approximately prolate spheroidal in shape and are *c*-shaped at maturity. Figure from [44].

Figure 2.5: Fetal brain (top) and its computer reconstruction from MRI (middle). The GM is labeled in orange and the LVs are labeled in blue (bottom). Figure from [44].

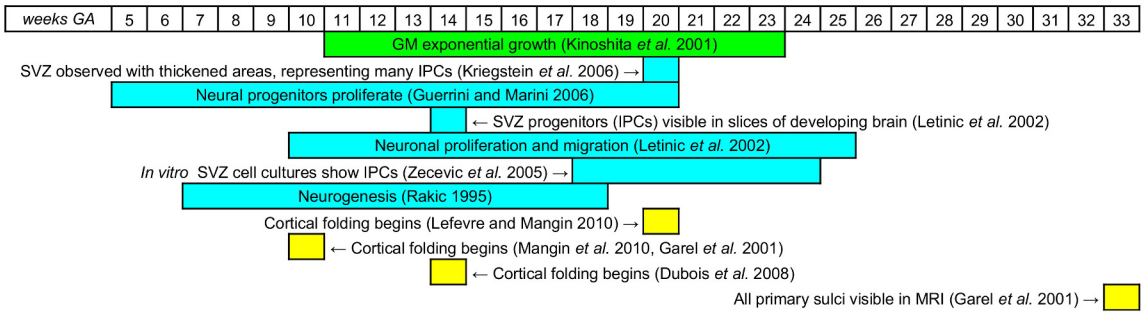


Figure 2.6: Chronology of selected cortical development events. Dates relevant to cortical folding appearance (yellow), IPC proliferation and neuron generation (blue), and exponential growth of GM (green) are plotted on a common time axis. While the literature does not agree on exact dates for cortical development events, it is clear that there is overlap among periods of GM exponential growth, IPC proliferation, neurogenesis, and cortical folding. Data obtained from [19, 28, 35, 44, 45, 47, 51, 59, 75, 103].

or 20 GA, depending on the literary source [19, 28, 47, 59]. Although there is a lack of consensus in the literature about the precise dates of these biological events, it is obvious that the period of exponential GM growth (11-23 weeks GA) coincides with many important events of cortical folding development.

### 2.1.4 Key Cells of the CNS

The principal types of cells in the CNS are neurons and glial cells, with glial cells accounting for 90% of all cells in the CNS [67, 80]. Neurons form the information highways of the CNS, encoding information in electrical impulses called action potentials that are transmitted from one neuron to another. The brain alone contains approximately 100 billion neurons. Glial cells serve as caregivers for neurons, performing jobs such as providing structural support and helping messages travel more quickly from neuron to neuron [80].

The main structures of the neuron are the dendrites, soma, axon hillock, axon, and presynaptic terminal (see Figure 2.7). The soma, or cell body, contains the cell's nucleus and performs essential tasks needed for the cell to survive. Dendrites receive information from other neurons, while the axon uses action potentials to transmit outgoing information from the neuron. The axon hillock, located where the axon originates from the soma, is the place from which action potentials are generated. The presynaptic terminal is responsible for the actual transmission of the "message" to the next neuron, usually via chemicals called neurotransmitters.

Cortical neurons will either make corticocortical or corticothalamic connections in the brain. Corticocortical connections occur when the axons of cortical neurons connect to dendrites of other cortical neurons. Corticothalamic connections occur between the axons of cortical neurons and the thalamus, an area of the brain responsible for directing sensory inputs to their corresponding cortical processing areas [67, 80].

Radial glial cells (RGCs) are special glial cells that have an important role in brain development. The soma of each RGC is anchored to a specific place in the VZ [75]. Each

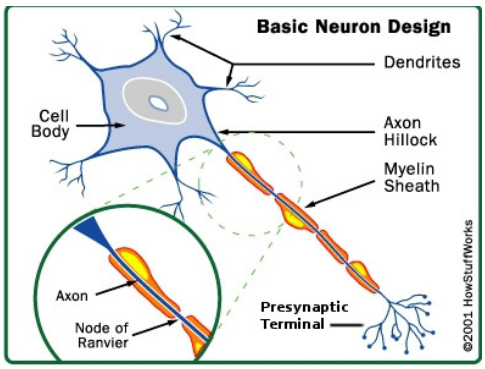


Figure 2.7: Neuron anatomy. The principal structures of the neuron are the dendrites, soma, axon hillock, axon, and presynaptic terminal. Figure adapted from [27].

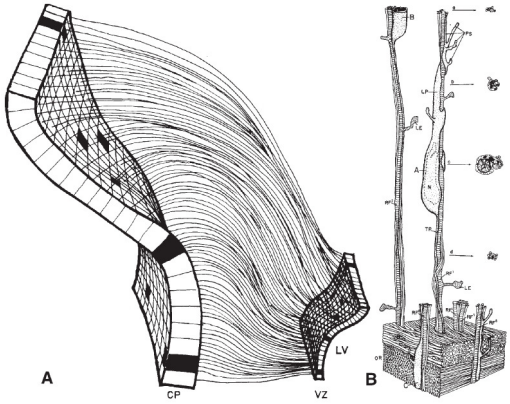


Figure 2.8: Radial glial cells. (a) RGCs establish a 1-1 correspondence between the VZ and cortical plate (CP). (b) Neuroblasts travel up the RGC's radial fiber to the CP. Figure adapted from [76].

RGC has a radial fiber shaft that extends out to the cortical plate (CP), the developmental precursor of the cerebral cortex [75, 76]. During development, RGCs create neuroblasts (developmental precursors of neurons), which then travel up the radial fiber of the RGCs to the CP [76]. These neuroblasts, along with others, will form the cerebral cortex [66]. RGCs are also responsible for the production of special proliferative cells called intermediate progenitor cells (IPCs) [66], which will be further discussed in Section 2.2. The radial fibers and somas of RGCs create a one-to-one correspondence between the VZ and CP (see Figure 2.8a) [76].

## 2.2 Biological Hypotheses of Cortical Development and Folding

There are numerous biological hypotheses that attempt to explain the process of cortical folding, and there is great debate as to what is the true underlying mechanism. While some hypotheses share common characteristics, others, such as the Intermediate Progenitor Model [45] and the Axonal Tension Hypothesis [22], are in direct opposition with one another. The following sections will discuss some of the most important biological viewpoints on the mechanism of cortical folding.

It is prudent to note that biologists often use the word "model" in place of "hypothesis". Thus, though the Intermediate Progenitor Model contains the word "model" in its name, it is simply another hypothesis that attempts to describe the biological mechanism behind cortical folding.

### 2.2.1 Radial Unit Hypothesis

The Radial Unit Hypothesis (RUH) [74] describes the formation of the CP and the 1-1 correspondence between the CP and VZ. The RUH proposes two stages of cellular division, namely, a symmetric RGC cellular division stage followed by an asymmetric RGC cellular division stage. In symmetric cellular division, the mother cell divides into two identical daughter cells; in asymmetric cellular division, the mother cell divides into daughter cells of two different cellular types.

During the symmetric cellular division stage, RGCs in the VZ divide into two RGCs (one to replace the original RGC and one new RGC), doubling the number of RGCs with each round of cellular division (see Figure 2.9a). Next, during the asymmetric cellular division stage, each RGC divides into a neuroblast and another RGC that replaces the original RGC. The newly produced neuroblasts then travel across the intermediate zone (IZ), which separates the VZ and CP during development [45, 74], and up to the CP along the radial fiber of the RGC from which they were generated (see Figure 2.9b). As more asymmetric divisions occur, multiple neuroblasts can be formed in the same location in the VZ and travel to the same location in the CP. When this occurs, the newer neuroblasts pass over any neuroblasts that are already there and travel to the outermost area of the CP. This process forms columns of neuroblasts called ontogenic columns [75]. When linked with the RGC from which they originated, the ontogenic columns form a 1-1 correspondence between the VZ and CP (see Figure 2.8a). The number of RGC symmetric and asymmetric divisions in a particular area of the developing brain are controlled by specific genes [77].

### 2.2.2 Intermediate Progenitor Hypothesis

The Intermediate Progenitor Hypothesis (IPH) [66] takes the ideas of the RUH one step further. The IPH states that while lower layers of the CP are created according to the RUH, upper cortical layers are created differently. After the creation of the lower cortical layers, the IPH proposes that the upper layers of the CP are formed in two stages. First, RGCs undergo a round of asymmetric divisions, dividing into a replacement RGC and an IPC. The IPC then migrates into the SVZ and undergoes either (i) a terminal symmetric division into two neuroblasts (see Figure 2.10) or (ii) up to two symmetric self-amplifications into

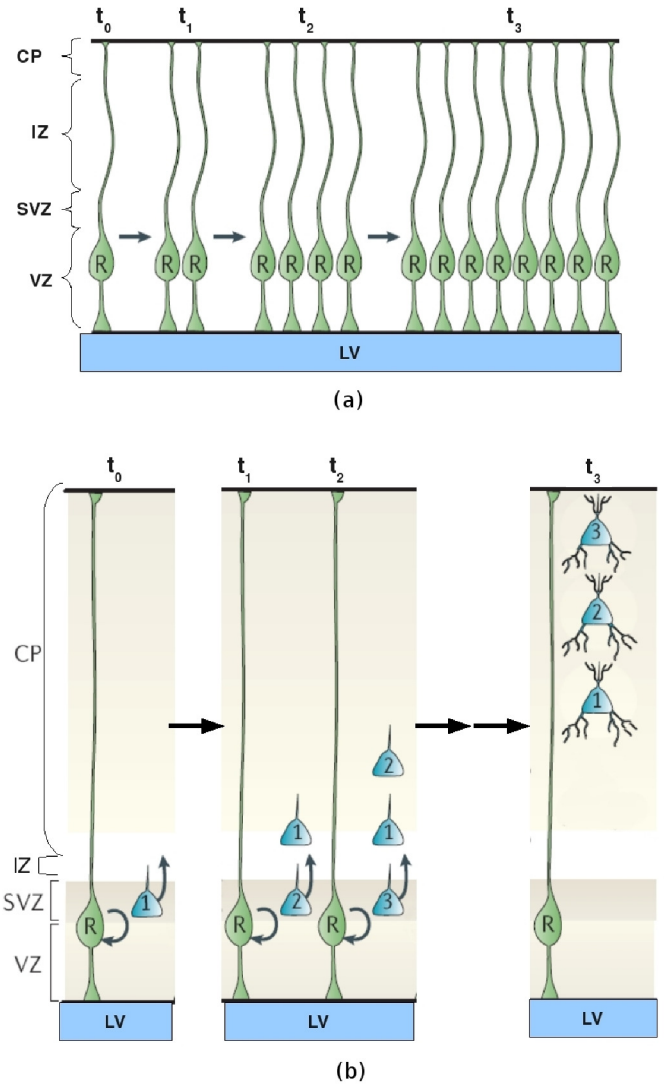


Figure 2.9: Cortical development according to the Radial Unit Hypothesis. (a) In the symmetric cellular division stage, the number of RGCs is doubled over time with each round of cellular division. (b) In the asymmetric cellular division stage, RGCs divide to produce one neuroblast and one replacement RGC per round of cellular division. Multiple neuroblasts can thus be produced from the same location in the VZ and migrate to the same location in the CP, forming ontogenic columns. Neuroblasts are numbered in decreasing age order. Figure adapted from [45].

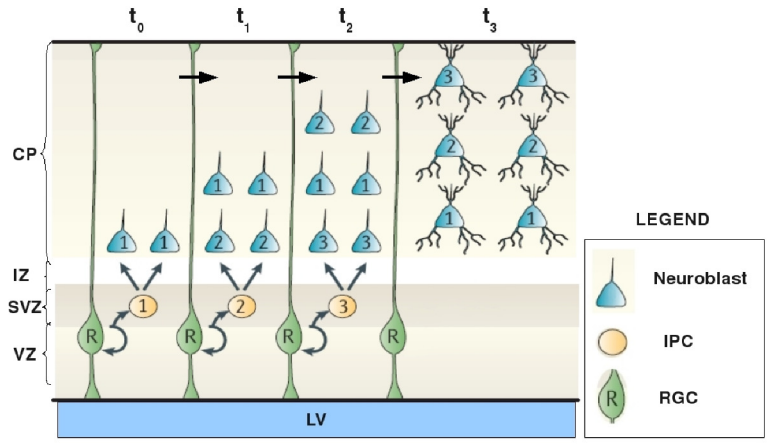


Figure 2.10: Cortical development according to the Intermediate Progenitor Hypothesis. At time $t_0$, a RGC asymmetrically divides to yield a replacement RGC and an IPC. This IPC undergoes a terminal symmetric division into two neuroblasts. At time $t_1$, another asymmetric RGC division occurs, yielding a replacement RGC and a new IPC. This IPC undergoes a terminal symmetric division into two neuroblasts which will eventually migrate above the neuroblasts produced at time $t_0$. Figure adapted from [45].

two IPCs, each of which eventually divides into two neuroblasts (see Figure 2.11) [73]. The neuroblasts migrate along the radial fiber of the corresponding RGC across the IZ and up to the very outermost area of the CP, above any neuroblasts already there. Any neuroblasts that originate at the same time end up in the same cortical layer, stacking outwardly in the CP by age.

### 2.2.3 Intermediate Progenitor Model

The Intermediate Progenitor Model (IPM) [45] expands upon the IPH. Overall, the IPM states that *regional* patterning of IPC self-amplification in the SVZ could lead to regional neuron amplification in the upper cortical layers, forming patterns of gyri and sulci in the cortex (see Figure 2.12). IPC neuronal amplification for the upper cortical layers would allow for increased cortical surface area while maintaining the size of the VZ, enabling the formation of a gyrencephalic cortex [45].

The IPM states that the number of IPCs occupying a region of the SVZ, and therefore the SVZ thickness, may be directly correlated with cortical fold formation. Areas of the SVZ in which the IPCs have undergone many rounds of self-amplification are thickened due to the many cells there, while areas of the SVZ where IPCs have not self-amplified much are thin. Recall that after self-amplification, each IPC becomes two neuroblasts which populate the upper layers of the developing cortex. Areas of the cortex corresponding to thick SVZ areas are thus populated by large numbers of neurons, forming gyri (hills), while areas corresponding to thin SVZ areas are populated by fewer neurons, forming sulci (valleys). In this fashion, the IPM dictates that regional patterns of IPC self-amplification would be correlated with SVZ thickness and could be used to predict cortical folding patterns.

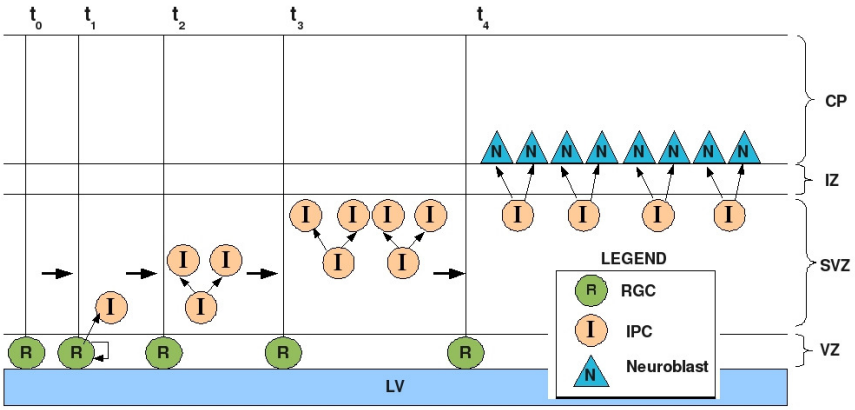


Figure 2.11: Intermediate progenitor cell self-amplification. After originating from a RGC, an IPC can undergo up to two rounds of self-amplification into two IPCs before a terminal symmetric division into neuroblasts.

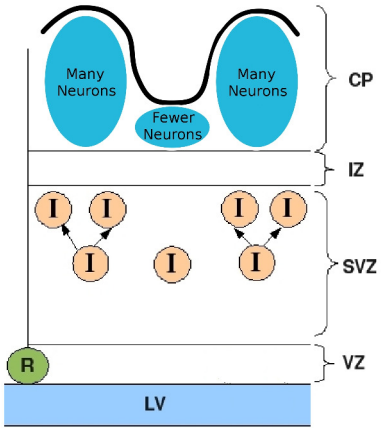


Figure 2.12: Intermediate Progenitor Model and cortical folding. According to the IPM, patterns of regional IPC self-amplification in the SVZ may be correlated with cortical folding patterns. Areas of high IPC self-amplification lead to neuron proliferation, corresponding with the formation of gyri. Areas of low IPC self-amplification lead to a lack of neuron proliferation that corresponds with the formation of sulci.

This correlation between SVZ thickness and gyrus/sulcus formation has been supported by observations in both developing monkeys and humans (see Figure 2.13).

Evidence suggests that self-amplification of IPCs in the SVZ, and therefore patterning of cortical folding, is genetically regulated. Genes such as *Pax6* have been shown to regulate cortical folding via modulating proper IPC development in mice [73]. Furthermore, several diffusible morphogens that affect cell proliferation, such as those of the *Wnt* pathway, have been shown to affect the number of IPCs in mice [73]. The *Wnt* pathway (pronounced 'wint') is a signaling pathway involved in neurogenesis [53].

### 2.2.4 Axonal Tension Hypothesis

The Axonal Tension Hypothesis (ATH) [22] provides an explanation of cortical folding that directly conflicts with that of the IPM. The ATH states that cortical folding is a direct consequence of tension resulting from corticocortical connections. Axonal tension of highly interconnected areas in the cortex pulls the cortical walls together, forming gyri (see Figure 2.14). Cortical areas joined by few corticocortical connections (or none at all) lack the axonal tension to pull towards each other, forming sulci.

Recent experimental investigations into the prefrontal cortex of adult rhesus monkeys have lent support to the ATH [37]. Tracing chemicals were injected into the brain to trace neuronal connections in the prefrontal cortex. The neuronal connections were then analyzed using photomicrography of coronal sections of the prefrontal cortex. The experiments demonstrated that the majority of axons of highly interconnected cortical regions followed straight paths, while axons of weakly connected regions followed curved paths around sulci. This result agrees with the ATH prediction that axonal paths of strongly interconnected cortical regions will be pulled straight as they form gyri (see the transition from the top right panel to bottom left panel in Figure 2.14).

## 2.3 Mathematical Models of Cortical Development and Folding

In this section, we outline three recent investigations into creating biomathematical models of cortical folding. We discuss a model that emphasizes morphogen gradient control of cortical precursor cells via a Turing system [86], a model that uses a Turing system to create chemical gradients that abstractly represent axonal tension [13], and a pair of finite element models that emphasize axonal tension without any morphogen involvement [29]. The Turing system models and one of the finite element models presented here utilize a static domain, while one of the finite element models incorporates domain growth.

### 2.3.1 Static Prolate Spheroid Turing Model

Striegel and Hurdal [86] used a two-equation activator-inhibitor Turing reaction-diffusion system on a static prolate spheroidal domain to hypothesize a new biological model of cortical folding called the Global Intermediate Progenitor (GIP) model [86]. The equations were

$$\left.\begin{aligned} u_t &= D\delta\nabla^2 u + \alpha u\left(1 - r_1 v^2\right) + v\left(1 - r_2 u\right), \\ v_t &= \delta\nabla^2 v + v\left(\beta + \alpha r_1 u v\right) + u\left(\gamma + r_2 v\right), \end{aligned}\right\}$$

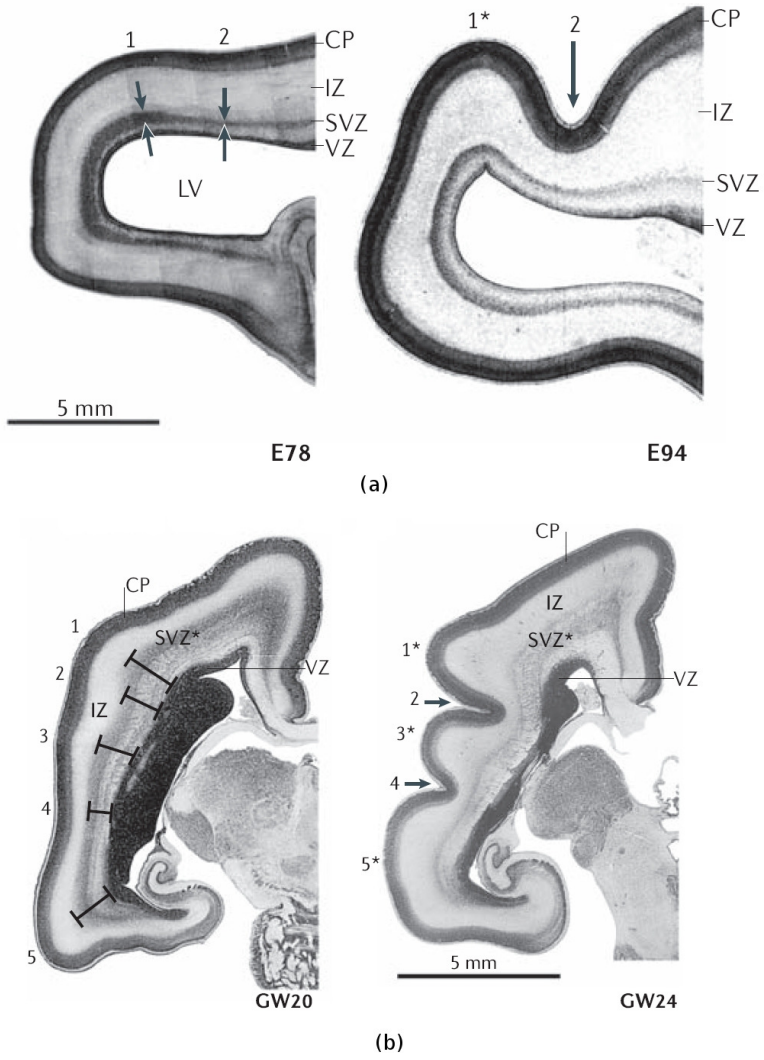


Figure 2.13: Intermediate Progenitor Model, subventricular zone thickness, and cortical folding. (a) In the developing macaque monkey brain, SVZ thickening (indicated by arrows under 1, left panel) leads to gyrus formation about two weeks later (1*, right panel). A thin area of SVZ (indicated by arrows under 2, left panel) leads to sulcus formation (2, right panel). (b) In the developing human brain, thick areas of SVZ (1, 3, and 5, left panel) lead to gyrus formation (1*, 3*, and 5*, right panel) four weeks later. Thin areas of SVZ (2 and 4, left panel) lead to sulcus formation (2 and 4, right panel). Figure from [45].

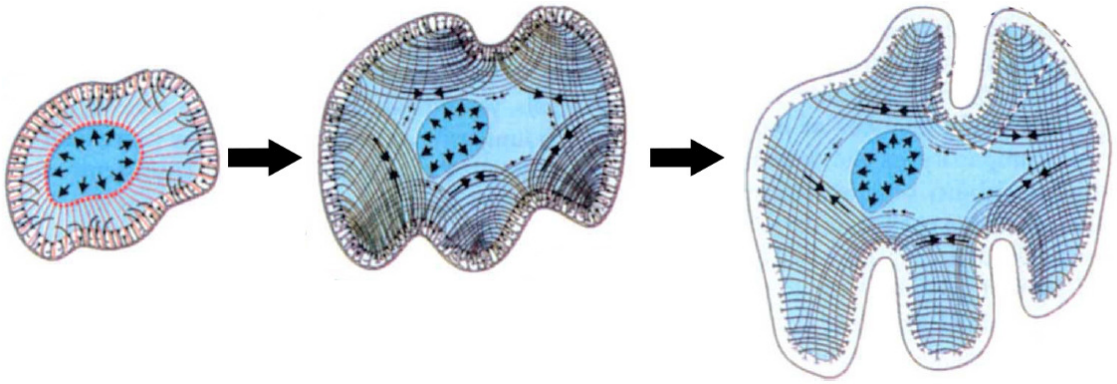

Figure 2.14: Axonal Tension Hypothesis mechanism for cortical folding. The ATH states that cortical folds result from axonal tension of highly interconnected cortical regions pulling the cortical walls together, forming gyri. The path followed by axons linking highly interconnected cortical regions straightens out as gyri are formed (transition from left to right). Figure adapted from [22].

where $u$, $v$ are the concentrations of activator and inhibitor, respectively, $D = \frac{D_u}{D_v}$ is the ratio of diffusion coefficients, $\delta > 0$ is inversely proportional to the domain scaling, and $\alpha, \beta, \gamma, r_1, r_2$ are parameters for Barrio-Varea-Maini (BVM) kinetics (see Section 3.1.3) [85]. The Turing system generated patterned regions of activation and nonactivation on the prolate spheroidal surface [42]. The activated regions represented activation of RGCs to form IPCs, which, according to the GIP model, is directly correlated with cortical folding. The GIP model concluded that cortical folding patterns are largely related to the size and shape of the LV, which are captured in the static domain mathematical model as size and eccentricity of the prolate spheroid. The static domain model was also applied to study evolutionary changes in cortical development between different species by predicting the order of sulcal development.

### 2.3.2 Labyrinthine Turing Model

Cartwright [13] constructed a Turing system model to generate labyrinthine patterns of cortical folds in the brain. The model used a nondimensionalized Turing system with van der Pol-FitzHugh-Nagumo kinetics [23, 24, 64, 96] on a two-dimensional static domain,

$$\left.\begin{aligned} \frac{\partial u}{\partial t} &= \nabla^2 u + \gamma\left(v - \frac{u^3}{3} + u\right), \\ \frac{\partial v}{\partial t} &= \delta\nabla^2 v - \gamma^{-1}\left(u + \nu + \beta v\right), \end{aligned}\right\} \tag{2.1}$$

where $u$ is an axon guidance chemical which activates axon growth, $v$ is an axon guidance chemical which inhibits axon growth, $\delta, \gamma$ govern relative activator/inhibitor range and strength, and $\nu$, $\beta$ are kinetics parameters. Newly formed axons follow chemical gradient signals as they migrate to their connection destination [3, 34, 88]. System 2.1 produced patterned areas of axon growth activation and nonactivation in the developing cortex, with

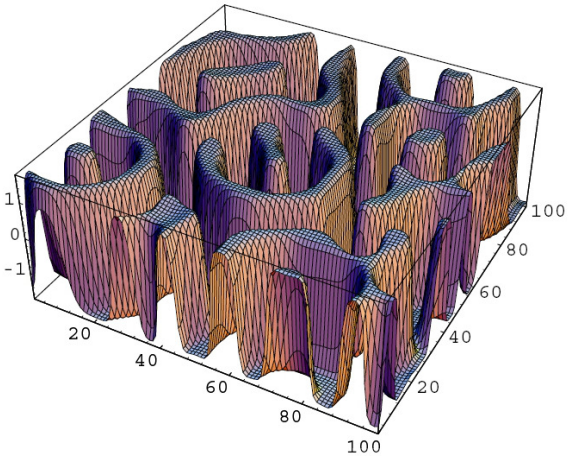


Figure 2.15: Labyrinthine Turing pattern of cortical folding. Cartwright [13] generated a labyrinthine Turing model which he interpreted as axonal migration and axonal tension leading to cortical folding. Activator concentration is represented by the vertical axis; the other two axes represent the two-dimensional domain. Figure from [13].

activated cortical regions exhibiting a high number of corticocortical connections and nonactivated cortical regions exhibiting a low number of corticocortical connections. Following the ideas of the ATH, activated cortical regions lead to gyrus formation, while nonactivated cortical regions lead to sulcus formation. By plotting the activator concentration on the $z$-axis against the rectangular domain, the patterns generated by System 2.1 were visualized as three-dimensional labyrinthine patterns that represent folding patterns in the cortex (see Figure 2.15). In this fashion, Cartwright built a chemical gradient-driven model of cortical folding that abstractly represented concepts from axonal pathfinding and axonal tension.

### 2.3.3 Turing Finite Element Model

Lefevre and Mangin [47] created a morphogen-based model of cortical folding by employing a Turing system with Gray-Scott kinetics on a self-deforming spherical domain using finite elements. Growth of the underlying spherical domain was not included in the model. The model system was

$$\begin{aligned} \partial_t u + u\partial_t \log\sqrt{g_t} &= d_1\nabla^2 u + F(1-u) - uv^2, \\ \partial_t v + v\partial_t \log\sqrt{g_t} &= d_2\nabla v + uv^2 - (F+k)v, \end{aligned}$$

where $F, k$ are the kinetics parameters, $g$ is the surface metric with determinant denoted by $\sqrt{g_t}$, and $d_1, d_2$ are the respective diffusion coefficients of inhibitor morphogen $u$ and activator morphogen $v$. Patterns of activator and inhibitor generated by the Turing system represented growth factor concentration patterns that act directly on the spherical surface by deforming it up or down after each iteration in time. This self-deformation resulted in labyrinthine patterns that represented cortical folding patterns (see Figure 2.16). Beginning with random initial conditions, the model was able to generate one fold that consistently

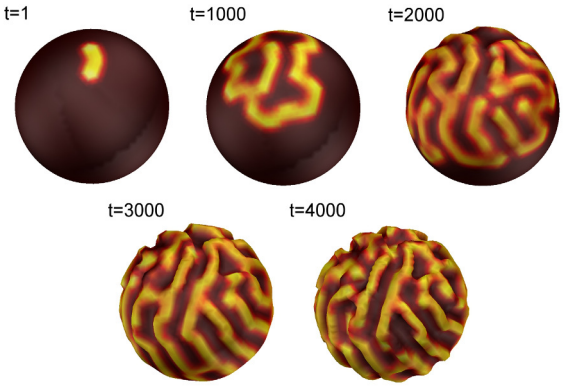


Figure 2.16: Turing system finite element model of cortical folding. A Turing system on a finite element self-deforming spherical domain was employed to generate patterns that represent cortical folding patterns. Figure adapted from [47].

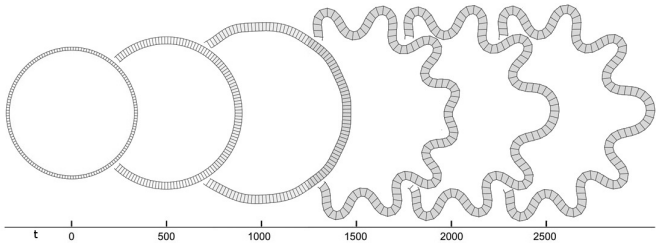


Figure 2.17: Two-dimensional tension-based finite element model of cortical folding. Logistically growing finite elements lining a circular domain with radial tension forces represented the development of cortical folds. Figure adapted from [93].

appeared, representing a primary cortical fold. The model was also able to generate some folds that were slightly less reproducible between simulations, representing the more variable secondary cortical folds in the brain.

### 2.3.4 Two-Dimensional Tension-Based Finite Element Model

Toro and Burnod [93] create a tension-based finite element model of human cortical folding on a growing 2-D circular domain. The boundary of the circle represented the developing cortex and was divided into finite elements whose area increased via a logistic growth function. Forces representing tension from axons and glial cells pulled on the circular boundary in the radial direction, yielding a wavy 2-D boundary representing cortical folding (see Figure 2.17). The model concluded that growth of the developing cortex is the driving force for the formation of cortical folds. The model also observed that including asymmetries in the geometry, the tension forces, or the carrying capacity of the growth function for different parts of the domain influenced the formation of folds.

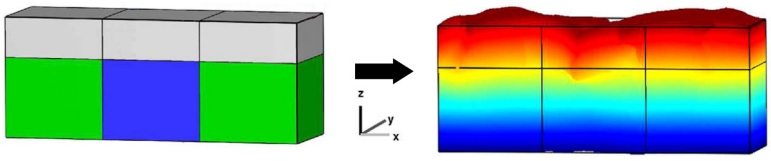

Figure 2.18: Three-dimensional tension-based finite element method model of cortical folding with tangential domain growth. Cortical areas with low axonal tension lead to sulci (center of domain), while cortical areas with high axonal tension lead to gyri (left and right of domain). Figure adapted from [29].

### 2.3.5 Three-Dimensional Tension-Based Finite Element Model

Geng *et al.* [29] used finite element methods to construct two 3-D axonal tension-based biomathematical models of cortical folding in sheep. Data was obtained via MRI images of fetal sheep brains. In their first model, the 3-D computational mesh was initialized directly from a portion of 70 day GA sheep MRI data (the entire MRI data could not be used all at once due to computational constraints). Physical axonal tension forces, CSF pressure forces, and forces due to growth were mathematically incorporated into the model, though dynamic domain growth was not included. Simulations were conducted with the aim of trying to reproduce the corresponding 90 day GA sheep MRI data. This first model was able to accurately predict the cortical folding geometry as well as the cortical thickness of gyri and sulci.

The inclusion of cortical growth distinguished the second finite element model from the first. Due to the increased computational demand from the addition of growth, the domain was selected to be a simple 3-D rectangle rather than a piece of actual MRI data. The sheep MRI data showed that the fetal sheep cortex grows anisotropically, with the growth rate tangential to the cortical surface greatly exceeding the growth rate radial to the cortical surface. Anisotropic cortical growth was mathematically incorporated into the model via an osmotic expansion representation. Osmotic expansion analogously represented cortical growth in that an increase in concentration of osmotically active particles (as a result of cell division, for example) in the cortex causes an increase in cortical volume. To capture tangentially preferred anisotropic growth, the cortical surface was only allowed to grow in the direction of the $xy$-plane, which represented the tangential direction in the model (see Figure 2.18). The sheep MRI data also suggested that subcortical axonal tension underlying sulci was less than subcortical axonal tension underlying gyri. For this reason, the rectangular domain was split into three regions from left to right in the $x$-direction, with the two outer regions initialized with high axonal tension and the inner region initialized with low axonal tension. As expected, numerical simulations resulted in the center region folding inward to form a sulcus surrounded by a gyrus on either side (see Figure 2.18). This second model supported the idea that a combination of axonal tension and tangential growth serves as a driving force for cortical fold development.

## 2.4 Motivation

As outlined in Section 2.2, there is debate amongst biologists over the underlying mechanisms of cortical folding, with hypotheses based on genetic chemical control (such as the IPM) competing against physical tension (ATH). To investigate the credence of the IPM and thereby the validity of genetic morphogen control of cortical folding, we use mathematical modeling and adopt a prolate spheroidal domain Turing system model of cortical folding. We use a prolate spheroid because it accurately models the shape of the LV and SVZ during early neurogenesis as discussed in Section 2.1.2 (see Figure 2.3); more details will be provided in Chapter 6. As discussed in Section 2.3, previous Turing system biomathematical models of cortical folding in the brain utilized a static, non-growing domain. To build a model which more accurately reflects the biology, we construct Turing models of cortical folding utilizing an exponentially or logistically growing domain. The mathematical details of our models are presented in Chapters 3–5, and their application to cortical folding is presented in detail in Chapter 6.

## 2.5 Conclusions

In this chapter, the major anatomical features of the brain and the key cells involved in cortical development were presented. Several biological hypotheses of how the cerebral cortex develops and folds were outlined. This chapter also discussed prior biomathematical models of cortical folding and outlined motivation for investigating a growing prolate spheroidal domain Turing system model of cortical folding.

Our mathematical models of cortical folding, which are presented in Chapter 6, assume the IPM view that regional patterns of IPC self-amplification might be directly correlated with cortical folding patterns. A Turing-reaction diffusion system is employed to create prepatterns of activation and nonactivation of IPC self-amplification in the SVZ. Activated regions represent areas of high IPC self-amplification, leading to gyri, while nonactivated regions represent areas of low IPC self-amplification, leading to sulci.

Turing reaction-diffusion systems and their ability to generate patterns are introduced in the following chapter. Chapter 4 discusses Turing systems on an exponentially growing prolate spheroid, while Chapter 5 discusses Turing systems on a logistically growing prolate spheroid. Further details of our mathematical models of cortical folding are discussed in Chapter 6.

# CHAPTER 3

# TURING REACTION-DIFFUSION SYSTEMS

In his classic 1952 paper, Alan M. Turing used a system of two reaction-diffusion equations to generate patterns representing chemical morphogen concentration gradients on the developing embryo [95]. The principal characteristic of what would come to be known as a "Turing system" was its ability to generate spatially inhomogeneous patterns from a spatially homogeneous steady state. This pattern-generating capability, now referred to as Turing behavior [18, 20, 41], has made Turing systems useful for mathematical modeling of numerous developmental biology phenomena such as the formation of leopard spots and zebra stripes as well as the initiation of alligator teeth [63]. Specifically, patterns generated by Turing systems serve as prepatterns of genetic factors to which cells of the developing organism can later differentially respond [63, 95].

In this chapter, general static and growing domain Turing systems are presented. The biological plausibility of Turing systems, the types of reaction kinetics they use, and an intuitive explanation of their pattern-generating capabilities are discussed. Lastly, a prolate spheroidal domain is incorporated into the growing domain Turing system framework, establishing the foundation for later chapters.

## 3.1 Static Domain Turing Systems

Consider a static domain with position vector $\mathbf{X}$ where $u(\mathbf{X},t)$ and $v(\mathbf{X},t)$ are concentrations of an activator morphogen $u$ and an inhibitor morphogen $v$. Let the diffusion coefficient $D_v$ of the inhibitor be greater than the diffusion coefficient $D_u$ of the activator, so that $0 < D_u < D_v$. Then the classic nondimensionalized Turing reaction-diffusion system is

$$\left.\begin{aligned} \frac{\partial u}{\partial t} &= D\nabla^2 u + \omega f(u,v), \\ \frac{\partial v}{\partial t} &= \nabla^2 v + \omega g(u,v), \end{aligned}\right\} \tag{3.1}$$

where $D = D_u/D_v \in (0,1)$, $\omega > 0$ arise from nondimensionalization and functions $f, g$ represent the reaction kinetics (source terms) [63, 95]. Refer to Section A.1 for a derivation of the generic reaction-diffusion equation. The diffusion coefficient ratio $D$ is required to satisfy $D < 1$ in order to reproduce the "short range activation, long range inhibition" [31]

phenomenon observed in numerous biological systems such as organogenesis in transplants [31] and hair follicle development in mice [82].

The reaction terms of System (3.1) create peaks of $u, v$ concentration, while the diffusion terms smooth out these peaks. The end result of this competition between peak creation and peak smoothing is the generation of characteristic Turing patterns. System (3.1) possesses the characteristic Turing pattern-generating behavior when two criteria are satisfied: (i) the system must tend to a linearly stable spatially uniform steady state $(u_0, v_0)$ in the absence of diffusion, and (ii) the steady state is driven unstable by random perturbations in the presence of diffusion. We call these two properties the Turing criteria.

### 3.1.1 Diffusion-Driven Instability and Pattern Formation

The second Turing criterion, often referred to as diffusion-driven instability [57, 63], can at first seem counterintuitive. Many learn in basic chemistry or biology class that diffusion acts as a stabilizing force between two areas of unequal solute concentration, but in a Turing system, diffusion acts as a destabilizing force. To illustrate the idea of how diffusion-driven instability occurs, consider the analogy of a generic reaction tank with two well-mixed reactants [62]. If there is no diffusion, the reactants will react with one another according to the law of mass action and reach a uniform steady state. This is linear stability in the absence of diffusion, the first Turing criterion. If diffusion is allowed at equal rates for each reactant, then any perturbations from the steady state will cause the reactants to react with each other and return to the steady state. However, if diffusion is allowed at greatly unequal rates, then the reaction rates cannot keep up with diffusion to return the system to the uniform steady state, and a spatially inhomogeneous pattern is formed. This is diffusion-driven instability, the second Turing criterion.

To describe how a Turing activator-inhibitor system generates spatially inhomogeneous patterns, consider the analogy of a dry forest that is prone to forest fires [62]. Suppose that firefighters on helicopters equipped with flame-retardant chemical cannon are dispersed randomly throughout the forest. Suppose also that the helicopters can fly faster than fire can spread, so that the helicopters can fly ahead of a fire to spray the flame retardant on trees and prevent them from being burned. Now suppose that fires (the "activator") break out in several random places throughout the forest; the breakout of fires represents the perturbation to the homogeneous steady state. As the fires begin to spread, the firefighting helicopters race ahead of the fires and spray unburned trees with flame retardant (the "inhibitor"). The end result is a forest patterned with areas of black burned trees and green unburned trees.

In a similar fashion, Turing systems generate spatially inhomogeneous patterns of activator and inhibitor morphogens. Recall that the diffusion coefficients of the activator $u$ and inhibitor $v$ in Turing System (3.1) must satisfy $D_u < D_v$. When the system is perturbed from its steady state in the presence of diffusion, the inhibitor morphogen can thus diffuse much faster than the activator morphogen. This leads to a pattern with areas of high activator concentration separated by areas of high inhibitor concentration, analogous to the black and green tree pattern in the aforementioned forest.

### 3.1.2 Biological Existence of Turing Patterns

Turing systems require the existence of chemicals which can form concentration gradient patterns; in the context of biology, these chemicals are morphogens that serve to influence the development of cells into specialized tissues and organs [57]. The validity of using a Turing system to model biological systems was debated for many years, as experimental evidence in *Drosophila* embryonic stripe development showed that Turing systems could not accurately describe the multiple underlying genetic interactions [1, 57].

Recent research, however, supports the plausibility and existence of Turing patterning in biological development. Evidence suggests that the density of hair follicles in developing mice is controlled by the expression of activator and inhibitor proteins [57, 82]. The activator protein WNT is much larger than the inhibitor protein DKK, thus WNT diffuses slower than DKK and can be modeled with a smaller diffusion coefficient than DKK. This fits the Turing system requirement of $D_u < D_v$, and so a Turing system model of mouse hair follicle patterning was proposed by Sick *et al.* [57, 82]. The Turing system was used to predict patterns of mouse hair follicle density that were confirmed experimentally using transgenic mice, supporting the use of Turing systems to model biological pattern formation.

### 3.1.3 Reaction Kinetics

In order to accurately model patterns in biological systems, a Turing system's reaction kinetics $f, g$ must be nonlinear functions [95]. Turing systems can be classified into four groups based on the type of kinetics selected [55]. Reaction kinetics are chosen based on the amount of information known about the underlying reactions of the system in question.

In a phenomenological Turing system, nothing is known about the actual reactions involved in the system. In this case, one selects or constructs kinetics that can reproduce the observed pattern. An example of a phenomenological Turing system is the Barrio-Varea-Maini (BVM) system [9], which will be discussed in more detail in Section 3.2.

Hypothetical Turing systems use kinetics based on a set of hypothetical chemical reactions satisfying the law of mass action. The Schnakenberg system is one example of a hypothetical Turing system [78]. While originally created to describe general chemical reactions that exhibit limit cycle oscillatory behavior, Schnakenberg kinetics have been used to investigate Turing pattern behavior in biological applications such as embryonic fluid flow asymmetry in the mouse [6, 58, 78, 81, 100].

An empirical Turing system uses kinetics that have been fit to reproduce known experimental data from the system to be modeled. The Thomas uric acid-oxygen system is an example of an empirical Turing system [89]. If the actual chemical reactions in the system are precisely known, the kinetics functions are calculated using the law of mass action. An example of a system in which the actual kinetics can be calculated is the chlorite-iodide-malonic acid starch (CIMA) reaction, which was the first experimentally observed Turing pattern [14, 55].

## 3.2 Growing Domain Turing Systems

To incorporate domain growth into System (3.1), let $S_t \subset \mathbb{R}^3$ be a two-dimensional regular growing surface with position vector $\mathbf{X}(\zeta, \eta, t)$ where $\zeta, \eta$ are spatial parameters for

$S_t$ and $t \geq 0$. If we let $h_1 = |\mathbf{X}_\zeta|, h_2 = |\mathbf{X}_\eta|$, then the incorporation of domain growth allows System (3.1) to become

$$\left.\begin{aligned} u_t &= D\Delta_s u - \partial_t(\ln(h_1 h_2))u + \omega f(u,v), \\ v_t &= \Delta_s v - \partial_t(\ln(h_1 h_2))v + \omega g(u,v), \end{aligned}\right\} \tag{3.2}$$

where $u_t = \frac{\partial u}{\partial t}, v_t = \frac{\partial v}{\partial t}$ and $\Delta_s$ is the Laplace-Beltrami operator on $S_t$ defined by

$$\Delta_s \phi = \frac{1}{h_1 h_2}\left[\left(\frac{h_2}{h_1}\phi_\zeta\right)_\zeta + \left(\frac{h_1}{h_2}\phi_\eta\right)_\eta\right] \tag{3.3}$$

for $\phi = u, v$ [72]. Refer to Section A.2 for a complete derivation of System (3.2).

Notice that including domain growth in a Turing system causes the formation of a new third term $-\partial_t(\ln(h_1 h_2))\phi$ (for $\phi = u, v$) in each equation of System (3.2) as compared to System (3.1). These terms represent dilution of the chemical concentrations due to domain growth [72]. The parameter $\omega$, often called the domain scale parameter [63], allows one to adjust the strength of the reaction terms relative to the strength of the diffusion and the dilution terms; this affects the pattern generated by the system as will be discussed in Chapters 4 and 5. System (3.2) allows one to construct a Turing system on an isotropically growing domain when $\mathbf{X}(\zeta, \eta, t) = \rho(t)\mathbf{X}_0(\zeta, \eta)$, where $\rho(t)$ is the domain growth function and $\mathbf{X}_0(\zeta, \eta)$ defines the domain at $t = 0$ [72].

Turing systems have also been generalized to encompass convection/advection-reaction-diffusion systems on growing domains [54]. However, since traditional reaction-diffusion systems have been demonstrated to exist in biological pattern development (see Section 3.1.2) and also have been used in previous biomathematical models of cortical folding (see Section 2.3), we will proceed using System (3.2).

We select nondimensional BVM kinetics [7, 9, 98] so that

$$\begin{aligned} f(u,v) &= u + av - Cuv - uv^2, \\ g(u,v) &= bv + hu + Cuv + uv^2, \end{aligned}$$

where $a, b, C, h$ are kinetics parameters (see Sections A.3 and A.4). BVM kinetics, classified as phenomenological, are constructed to primarily give striped patterns when $C = 0$ and spotted patterns when $C > 0$ [9, 21]. Since the biological mechanism of cortical folding is not completely understood, BVM kinetics are a reasonable choice for a model of cortical folding.

## 3.3 Growing Prolate Spheroid

System (3.2) is implemented on a growing prolate spheroidal domain. Two different biologically relevant growth functions are utilized to investigate the versatile pattern-generating capabilities of a growing domain Turing system. Exponential growth is implemented in Chapter 4 and logistic growth is presented in Chapter 5. Motivation for a growing prolate spheroidal domain and each type of domain growth is discussed in Chapter 6.

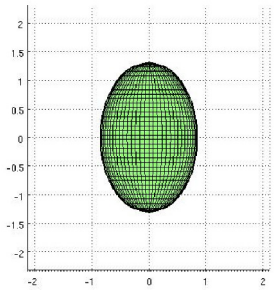

(a) $f = 2$, $\xi = 1.3141$, surface area $= 4\pi$

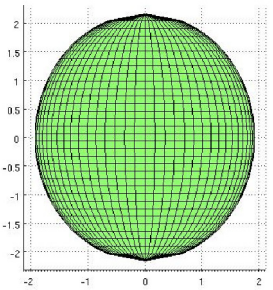

(b) $f = 2$, $\xi = 2.1640$, surface area $= 16\pi$

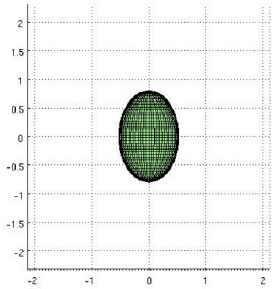

(c) $f = 1.2247$, $\xi = 1.3141$, surface area $= 1.5\pi$

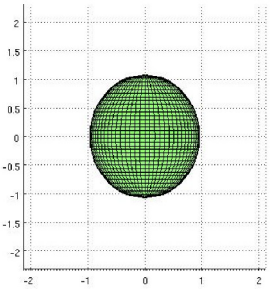

(d) $f = 1$, $\xi = 2.1640$, surface area $= 4\pi$

Figure 3.1: Prolate spheroids for different values of $f$ and $\xi$. Changing $\xi$ while holding $f$ constant changes the shape of the spheroid. Altering $f$ while holding $\xi$ constant changes the size but maintains the shape of the spheroid.

A prolate spheroid is obtained by rotating an ellipse with semimajor axis length $a$ and semiminor axis length $b$ about its major axis. The coordinate system for a prolate spheroid created from such an ellipse is defined by

$$x = \frac{f}{2}\sqrt{(1-\eta^2)(\xi^2-1)}\cos 2\pi\zeta, \quad y = \frac{f}{2}\sqrt{(1-\eta^2)(\xi^2-1)}\sin 2\pi\zeta, \quad \text{and} \quad z = \frac{f}{2}\eta\xi,$$

where $\theta$ is the polar angle with $\eta = \cos\theta \in [-1, 1]$, $\phi$ is the azimuthal angle with $\zeta = \frac{\phi}{2\pi} \in [0, 1)$, $\xi > 1$ is the radial term, and $f$ is the interfocal distance with $f = 2\sqrt{a^2 - b^2}$ [25]. If $E$ is the eccentricity of the prolate spheroid, then the shape of the spheroid can be altered by altering the value of $\xi$, as $E = \frac{1}{\xi}$ (see Section A.5). Given a fixed value of $f$ and increasing the value of $\xi$ results in a rounder, more sphere-like prolate spheroid; increasing $f$ given a fixed $\xi$ increases the overall size of the prolate spheroid while maintaining its shape (see Figure 3.1) [25].

Define the position vector $\mathbf{X}$ on a growing prolate spheroid as

$$\mathbf{X}(\zeta,\eta,t)=\rho(t)\begin{pmatrix}\frac{f_0}{2}\sqrt{(\xi^2-1)(1-\eta^2)}\cos 2\pi\zeta\\ \frac{f_0}{2}\sqrt{(\xi^2-1)(1-\eta^2)}\sin 2\pi\zeta\\ \frac{f_0}{2}\xi\eta\end{pmatrix},$$

where $f_0$ is the interfocal distance at $t=0$ and the growth function is given by $\rho(t)$. We calculate the Laplace-Beltrami operator $\Delta_s$ defined in Equation (3.3) and the dilution term $-\partial_t(\ln(h_1h_2))\phi$ (for $\phi=u,v$). To this end, we observe that

$$h_1=\rho(t)\pi f_0\sqrt{(\xi^2-1)(1-\eta^2)}\quad\text{and}\quad h_2=\rho(t)\frac{f_0}{2}\sqrt{\frac{\xi^2-\eta^2}{1-\eta^2}}.$$

It follows that

$$-\partial_t(\ln(h_1h_2))\phi=-2\frac{\dot\rho}{\rho}\phi \tag{3.4}$$

and

$$\Delta_s\phi=\frac{1}{\rho^2}\Delta_\dagger\phi$$

where

$$\Delta_\dagger\phi=\frac{1}{\pi^2f_0^2(1-\eta^2)(\xi^2-1)}\phi_{\zeta\zeta}+\frac{4(1-\eta^2)}{f_0^2(\xi^2-\eta^2)}\phi_{\eta\eta}-\frac{4\eta(2\xi^2-\eta^2-1)}{f_0^2(\xi^2-\eta^2)^2}\phi_\eta.$$

Overall, System (3.2) on a growing prolate spheroidal domain becomes

$$\left.\begin{aligned}u_t&=\frac{D}{\rho^2}\Delta_\dagger u-2\frac{\dot\rho}{\rho}u+\omega f(u,v),\\ v_t&=\frac{1}{\rho^2}\Delta_\dagger v-2\frac{\dot\rho}{\rho}v+\omega g(u,v).\end{aligned}\right\} \tag{3.5}$$

## 3.4 Conclusions

This chapter outlined the basic properties of Turing systems, their basic types of kinetics functions, and the intuition behind their pattern-generating abilities. A framework for including domain growth in a Turing system was presented and subsequently implemented on a prolate spheroidal domain, yielding System (3.5). In Chapters 4 and 5, respectively, System (3.5) is implemented under exponential and logistic domain growth, ultimately leading to growing domain Turing models of cortical folding that are presented in Chapter 6.

# CHAPTER 4

# EXPONENTIALLY GROWING DOMAIN TURING SYSTEM

To illustrate the types of patterns that can be generated by a growing domain Turing system, we incorporate exponential domain growth into System (3.5). We begin by deriving mathematical conditions that explicitly state when an exponentially growing domain Turing system satisfies the two Turing criteria and thus can generate Turing patterns. We then discuss proper system parameter selection for an exponentially growing prolate spheroidal domain Turing system with BVM kinetics. Finally, we utilize numerical simulations to investigate the pattern-generating abilities of such a system. We will see that adding domain growth to a Turing system induces an important change in the system's pattern-generating behavior. These results have appeared in [90] and have been submitted in [91, 92].

To begin, we select an exponential growth function

$$\rho(t) = e^{Rt}$$

with $R > 0, t \geq 0$. The dilution term from Equation (3.4) is

$$-2\frac{\dot{\rho}}{\rho}\phi = -2R\phi \tag{4.1}$$

and System (3.5) becomes

$$\left.\begin{aligned} u_t &= \frac{D}{\rho^2}\Delta_\dagger u - 2Ru + \omega f(u,v), \\ v_t &= \frac{1}{\rho^2}\Delta_\dagger v - 2Rv + \omega g(u,v). \end{aligned}\right\} \tag{4.2}$$

Observe that setting the growth rate to $R = 0$ reduces System (4.2) to a static domain Turing System, which is discussed further in Section 4.1.3.

## 4.1 Turing Conditions

It is highly beneficial to have mathematical equations whose satisfaction indicates when System (4.2) satisfies the two Turing criteria and is therefore capable of generating Turing patterns. We call such equations Turing conditions and derive them using linear stability analysis [32].

### 4.1.1 Turing Criterion: Linear Stability in the Absence of Diffusion

To derive mathematical Turing conditions representing the first Turing criterion, we assume that System (4.2) possesses the required spatially uniform steady state $(u_0, v_0)$, and that $(u_0, v_0)$ remains a steady state in the absence of diffusion. System (4.2) in the absence of diffusion becomes

$$\left.\begin{array}{rcl} u_t &=& -2Ru + \omega f(u,v), \\ v_t &=& -2Rv + \omega g(u,v), \end{array}\right\} \tag{4.3}$$

where $(u_0, v_0)$ is the solution to

$$\left.\begin{array}{rcl} 0 &=& -2Ru_0 + \omega f(u_0,v_0), \\ 0 &=& -2Rv_0 + \omega g(u_0,v_0). \end{array}\right\} \tag{4.4}$$

Define $\mathbf{w}(t)$ to be a perturbation from $(u_0, v_0)$ such that

$$\mathbf{w}(t) = \begin{pmatrix} u(t) - u_0 \\ v(t) - v_0 \end{pmatrix} = \begin{pmatrix} \epsilon_u \\ \epsilon_v \end{pmatrix} \tag{4.5}$$

with $0 < |\epsilon_u|, |\epsilon_v| \ll 1$. Notice that Equation (4.5) allows System (4.3) to be rewritten as

$$\mathbf{w}_t = \begin{pmatrix} u_t \\ v_t \end{pmatrix}.$$

Next, we linearize $u_t, v_t$ from System (4.3) by performing a Taylor expansion about $(u_0, v_0)$, yielding

$$\begin{aligned} u_t &= -2Ru_0 + \omega f(u_0,v_0) + \epsilon_u \frac{\partial}{\partial u}\left(-2Ru + \omega f(u,v)\right)\Big|_{(u_0,v_0)} \\ &\quad + \epsilon_v \frac{\partial}{\partial v}\left(-2Ru + \omega f(u,v)\right)\Big|_{(u_0,v_0)} + O(\epsilon^2), \end{aligned}$$

and similarly for $v_t$. Using System (4.4) and ignoring $O(\epsilon^2)$ and higher terms, we can write

$$\begin{aligned} u_t &\approx -2R\epsilon_u + \omega[\epsilon_u f_u(u_0,v_0) + \epsilon_v f_v(u_0,v_0)], \\ v_t &\approx -2R\epsilon_v + \omega[\epsilon_u g_u(u_0,v_0) + \epsilon_v g_v(u_0,v_0)], \end{aligned}$$

so that

$$\mathbf{w}_t = -2R\mathbf{w} + \omega A\mathbf{w} \tag{4.6}$$

with

$$A = \begin{pmatrix} f_u & f_v \\ g_u & g_v \end{pmatrix}_{(u_0,v_0)}. \tag{4.7}$$

Consider solutions to Equation (4.6) with form $\mathbf{w}(t) = \mathbf{c}e^{\lambda t}$, where $\mathbf{c}$ is a vector of constants. To achieve the desired linear stability of $(u_0, v_0)$, perturbations $\mathbf{w}$ must approach 0 as $t$ increases, which occurs when $Re(\lambda) < 0$. By substituting $\mathbf{w}(t) = \mathbf{c}e^{\lambda t}$ into Equation (4.6) and dividing through by $e^{\lambda t}$, we obtain the eigenvalue equation

$$\lambda\mathbf{c} = \omega A\mathbf{c} - 2R\mathbf{c} = \tilde{A}\mathbf{c},$$

where

$$\tilde{A} = \omega A - 2RI = \begin{pmatrix} \omega f_u - 2R & \omega f_v \\ \omega g_u & \omega g_v - 2R \end{pmatrix}_{(u_0,v_0)}.$$

For notational brevity it is assumed that $f_u, f_v, g_u, g_v$ are evaluated at the steady state $(u_0, v_0)$ in future calculations.

The characteristic equation of $\tilde{A}$,

$$\det(\tilde{A} - \lambda I) = \begin{vmatrix} \omega f_u - 2R - \lambda & \omega f_v \\ \omega g_u & \omega g_v - 2R - \lambda \end{vmatrix} = 0,$$

implies that the eigenvalues $\lambda$ of $\tilde{A}$ satisfy

$$\lambda^2 - \lambda \mathrm{tr}\tilde{A} + \det \tilde{A} = 0, \tag{4.8}$$

where

$$\begin{aligned} \mathrm{tr}\tilde{A} &= \omega(f_u + g_v) - 4R \quad \text{and} \\ \det \tilde{A} &= \omega^2(f_u g_v - f_v g_u) - 2R\omega(f_u + g_v) + 4R^2. \end{aligned}$$

Since Equation (4.8) has solutions

$$\lambda_{1,2} = \frac{1}{2}\mathrm{tr}\tilde{A} \pm \frac{1}{2}\sqrt{\left(\mathrm{tr}\tilde{A}\right)^2 - 4\det \tilde{A}},$$

it follows that $Re\,\lambda < 0$ when

$$\begin{aligned} \mathrm{tr}\ \tilde{A} = \omega(f_u + g_v) - 4R &< 0 \quad \text{and} \\ \det\ \tilde{A} = \omega^2(f_u g_v - f_v g_u) - 2R\omega(f_u + g_v) + 4R^2 &> 0. \end{aligned} \tag{4.9}$$

These two inequalities constitute the first two mathematical Turing conditions for System (4.2); when these inequalities are satisfied, System (4.2) possesses a steady state that is linearly stable in the absence of diffusion.

### 4.1.2 Turing Criterion: Diffusion-Driven Instability

To derive Turing conditions representing diffusion-driven instability, we begin by linearizing System (4.2) about $(u_0, v_0)$ to obtain

$$\mathbf{w}_t = D_M \Delta_\dagger \mathbf{w} - 2R\mathbf{w} + \omega A\mathbf{w}, \tag{4.10}$$

where

$$D_M = \frac{1}{\rho^2}\begin{pmatrix} D & 0 \\ 0 & 1 \end{pmatrix}$$

and $\mathbf{w}$ is the perturbation defined in Equation (4.5). Consider solutions to Equation (4.10) with form

$$\mathbf{w}(\mathbf{X}, t) = \sum_k c_k e^{\lambda t}\mathbf{Y}_k(\mathbf{X}), \tag{4.11}$$

where $c_k$ are Fourier coefficients determined by the initial conditions and $\mathbf{Y}_k$ are prolate spheroidal harmonics; that is, $\mathbf{Y}_k$ are solutions to the Helmholtz equation $\Delta\mathbf{Y}_k + k^2\mathbf{Y}_k = 0$ on a prolate spheroid. Substitute Equation (4.11) into Equation (4.10) and divide through by $e^{\lambda t}$ to obtain

$$\sum_k c_k(\lambda\mathbf{Y}_k + D_M k^2\mathbf{Y}_k + 2R\mathbf{Y}_k - \omega A\mathbf{Y}_k) = 0,$$

where we have used $-\Delta_\dagger\mathbf{Y}_k = k^2\mathbf{Y}_k$. Since we desire nontrivial solutions $\mathbf{w}$, it must be that $c_k \neq 0$, and

$$\lambda\mathbf{Y}_k + D_M k^2\mathbf{Y}_k + 2R\mathbf{Y}_k - \omega A\mathbf{Y}_k = 0. \tag{4.12}$$

Rearranging Equation (4.12) yields another eigenvalue equation,

$$\lambda\mathbf{Y}_k = (-D_M k^2 - 2RI + \omega A)\mathbf{Y}_k,$$

leading to the characteristic equation

$$\det(\tilde{A} - D_M k^2 - \lambda I) = 0. \tag{4.13}$$

When evaluated, the determinant in Equation 4.13 can be rewritten as

$$\lambda^2 + \lambda\left[\frac{k^2}{\rho^2}(1+D) - \text{tr }\tilde{A}\right] + h(k^2) = 0, \tag{4.14}$$

where

$$h(k^2) \quad = \quad \frac{D}{\rho^4}(k^2)^2 + \frac{k^2}{\rho^2}[2R(1+D) - \omega(f_u + Dg_v)] + \det\,\tilde{A}.$$

Setting $k^2 = 0$ reduces the analysis to the no-diffusion case. Since we wish to derive Turing conditions for diffusion-driven instability, we only consider $k^2 > 0$ from this point onward.

It must be that $Re(\lambda) > 0$ to achieve diffusion-driven instability. Solving Equation (4.14) using the quadratic formula yields

$$\lambda_{1,2} = -\frac{1}{2}\left(\frac{k^2}{\rho^2}(1+D) - \text{tr }\tilde{A}\right) \pm \frac{1}{2}\sqrt{\left(\frac{k^2}{\rho^2}(1+D) - \text{tr }\tilde{A}\right)^2 - 4h(k^2)}. \tag{4.15}$$

Then $Re(\lambda) > 0$ is achieved when either (i)

$$\frac{k^2}{\rho^2}(1+D) - \text{tr }\tilde{A} < 0 \tag{4.16}$$

or (ii)

$$\lambda = -\frac{1}{2}\left(\frac{k^2}{\rho^2}(1+D) - \text{tr }\tilde{A}\right) + \frac{1}{2}\sqrt{\left(\frac{k^2}{\rho^2}(1+D) - \text{tr }\tilde{A}\right)^2 - 4h(k^2)} \tag{4.17}$$

and

$$h(k^2) < 0. \tag{4.18}$$

Equation (4.16) cannot be satisfied if the Turing condition given in Equation (4.9) is satisfied. Thus, to achieve diffusion-driven instability, Equations (4.17) and (4.18) must be satisfied.

A necessary condition for the satisfaction of Equation (4.18) is

$$2R(1+D) - \omega(f_u + Dg_v) < 0, \tag{4.19}$$

which constitutes the first mathematical condition for System (4.2) to satisfy diffusion-driven instability, and the third mathematical Turing condition overall. Notice that Equation (4.19) is a necessary but not sufficient condition to satisfy $h(k^2) < 0$; one must select the positive square root from Equation (4.15) as well as ensure that

$$\left|\frac{k^2}{\rho^2}[2R(1+D) - \omega(f_u + Dg_v)]\right| > \left|\frac{D}{\rho^4}(k^2)^2 + \det \tilde{A}\right|.$$

To guarantee that $h(k^2) < 0$ is satisfied, a fourth mathematical Turing condition is derived. Since $h(k^2)$ is an upward-opening parabola in $k^2$, $h(k^2) < 0$ can be always satisfied if Equation (4.19) is satisfied and $h_{\min} = \min\left[h(k^2)\right] < 0$ . By differentiating $h(k^2)$ with respect to $k^2$ and setting the derivative equal to zero, we see that $h_{\min}$ occurs when

$$k^2 = k^2_{\min} = -\frac{\rho^2}{2D}[2R(1+D) - \omega(f_u + Dg_v)].$$

It then follows that

$$\begin{aligned} h_{\min} = h\left(k^2_{\min}\right) =& R^2\left[4 - \frac{(1+D)^2}{D}\right] + R\omega\left[\frac{1}{D}(1+D)(f_u + Dg_v) - 2(f_u + g_v)\right] \\ &+ \omega^2\left[(f_u g_v - f_v g_u) - \frac{1}{4D}(f_u + Dg_v)^2\right], \end{aligned}$$

so that $h(k^2) < 0$ when

$$\begin{aligned} R^2\left[4 - \frac{(1+D)^2}{D}\right] + R\omega\left[\frac{1}{D}(1+D)(f_u + Dg_v) - 2(f_u + g_v)\right] \\ + \omega^2(f_u g_v - f_v g_u) < \frac{\omega^2}{4D}(f_u + Dg_v)^2. \end{aligned}$$

This equation is the second mathematical condition required for System (4.2) to achieve diffusion-driven instability and the fourth mathematical Turing condition overall.

### 4.1.3 Summary of Turing Conditions

By using linear stability analysis, we derived four mathematical conditions that, when satisfied, guarantee the exponentially growing prolate spheroidal domain Turing System (4.2)

is capable of generating Turing patterns. These four Turing conditions are

$$\begin{aligned}
\text{tr } \tilde{A} = \omega(f_u + g_v) - 4R &< 0, && (4.20a)\\
\det \tilde{A} = \omega^2(f_u g_v - f_v g_u) - 2R\omega(f_u + g_v) + 4R^2 &> 0, && (4.20b)\\
2R(1+D) - \omega(f_u + Dg_v) &< 0, && (4.20c)\\
R^2\left[4 - \frac{(1+D)^2}{D}\right] + \omega^2(f_u g_v - f_v g_u) & \\
+R\omega\left[\frac{1}{D}(1+D)(f_u + Dg_v) - 2(f_u + g_v)\right] &< \frac{\omega^2}{4D}(f_u + Dg_v)^2, && (4.20d)
\end{aligned}$$

where the first two conditions give linear stability in the absence of diffusion and the second two conditions give diffusion-driven instability.

Recall that System (4.2) can be changed to a static domain Turing system by setting the growth rate to $R = 0$, giving System (3.1). The four exponentially growing domain Turing conditions in (4.20) then simplify to the static domain Turing conditions [63]:

$$\begin{aligned}
\text{tr } A = f_u + g_v &< 0, && (4.21a)\\
\det A = f_u g_v - f_v g_u &> 0, && (4.21b)\\
f_u + Dg_v &> 0, && (4.21c)\\
\det A &< \frac{1}{4D}(f_u + Dg_v)^2, && (4.21d)
\end{aligned}$$

where $A$ is given in Equation (4.7). System parameters must therefore also satisfy these four static domain Turing conditions. It follows from Equations (4.21a) and (4.21c) that $f_u, g_v$ are of opposite sign and $D \neq 1$. In System (4.2), $D$ must satisfy $D \in (0, 1)$, thus system parameters must be chosen to satisfy $f_u > 0$ and $g_v < 0$.

The space of parameters for which the Turing conditions in (4.20) are satisfied, often called the Turing space, can be larger for an exponentially growing domain Turing system than for a corresponding static domain Turing system. Comparing the first Turing condition in the growing and static domains, we can see that Equation (4.21a) requires $f_u + g_v$ to be strictly negative while Equation (4.20a) requires that $f_u + g_v < \frac{4R}{\omega}$. Since $R, \omega > 0$, the exponentially growing domain Turing condition (Equation (4.20a)) allows $f_u + g_v$ to potentially be positive, allowing for a larger Turing space than a static domain Turing system. Furthermore, if we compare the second Turing condition in the growing and static domains, we notice that Equation (4.20b) implies

$$\omega^2(f_u g_v - f_v g_u) > 2R[\omega(f_u + g_v) - 2R] > 2R[\omega(f_u + g_v) - 4R] = 2R \,\text{tr } \tilde{A}. \qquad (4.22)$$

While Equation (4.21b) requires that $f_u g_v - f_v g_u$ be strictly positive, Equation (4.22) implies that $f_u g_v - f_v g_u$ only needs to be greater than some negative number since the Equation (4.20a) requires $\text{tr } \tilde{A} < 0$. Again, this shows that an exponentially growing domain Turing system allows for a larger Turing space than a static domain Turing system.

## 4.2 Kinetic Parameter Selection

As discussed in Section 3.1, we select nondimensional BVM kinetics so that System (4.2) becomes

$$\left.\begin{aligned} u_t &= \frac{D}{\rho^2}\Delta_\dagger u - 2Ru + \omega(u + av - Cuv - uv^2), \\ v_t &= \frac{1}{\rho^2}\Delta_\dagger v - 2Rv + \omega(bv + hu + Cuv + uv^2). \end{aligned}\right\} \tag{4.23}$$

Traditional use of BVM kinetics in static domain Turing systems sets parameter values so that $(0,0)$ is the only spatially uniform steady state of the system [9].

It is desirable to accomplish this for the exponentially growing domain System 4.23 as well. However, adding growth to a reaction-diffusion system adds the dilution term which must be considered when finding the steady state(s) of System 4.23. Recall that the steady state of any Turing system must remain a steady state in the absence of diffusion. A steady state $(u,v) = (u_0, v_0)$ of System 4.23 must then satisfy

$$0 = -2Ru_0 + \omega(u_0 + av_0 - Cu_0v_0 - u_0v_0^2), \tag{4.24a}$$
$$0 = -2Rv_0 + \omega(bv_0 + hu_0 + Cu_0v_0 + u_0v_0^2), \tag{4.24b}$$

from which it follows that

$$v_0 = \frac{-u_0(-2R + \omega + \omega h)}{-2R + \omega a + \omega b} \tag{4.25}$$

if $-2R + \omega a + \omega b \neq 0$. Requiring $-2R + \omega + \omega h = 0$, which implies

$$h = \frac{2R}{\omega} - 1, \tag{4.26}$$

ensures that $v_0 = 0$ is the only possible $v$ coordinate of the steady state. Substituting $v_0 = 0$ into Equation 4.24b yields

$$0 = \omega h u_0.$$

As $\omega > 0$, requiring $h \neq 0$ ensures that $u_0 = 0$. In summary, in order for $(0,0)$ to be the only steady state of System 4.23, it must be that

$$\left.\begin{aligned} -2R + \omega a + \omega b &\neq 0, \\ h = \frac{2R}{\omega} - 1 &\neq 0, \quad \text{and} \\ \omega &\neq 2R, \end{aligned}\right\} \tag{4.27}$$

where the third equation follows readily from the second.

The parameters of System (4.23) must be selected to satisfy the four mathematical Turing conditions in (4.20). Nondimensional BVM kinetics have partial derivatives

$$f_u = 1, \quad f_v = a, \quad g_u = h = \frac{2R}{\omega} - 1, \quad \text{and} \quad g_v = b,$$

where all partial derivatives are evaluated at the steady state $(0,0)$ as in Section 4.1. From Section 4.1.3, we require $g_v < 0$; thus $b < 0$. Substituting BVM kinetics partial derivatives into (4.20), it follows that the four mathematical Turing conditions for System (4.23) are

$$\left.\begin{array}{rcl} \omega(1+b) - 4R & < & 0, \\ \omega^2(a+b) - 2R\omega(1+a+b) + 4R^2 & > & 0, \\ 2R(1+D) - \omega(1+Db) & < & 0, \quad \text{and} \\ \omega^2(a+b) + R^2\left(2 - \frac{1}{D} - D\right) & & \\ +R\omega\left(\frac{1}{D} - b - 1 + Db - 2a\right) & < & \dfrac{\omega^2}{4D}(1+Db)^2. \end{array}\right\} \tag{4.28}$$

## 4.3 Numerical Results

We numerically implement System (4.23) using a forward-time central-space finite difference scheme coded in FORTRAN [61, 90]. A prolate spheroidal domain has singularities at the north pole ($\eta = 1$) and south pole ($\eta = -1$) of the prolate spheroid. Thus, special care to avoid these singularities must be taken when establishing the spatial mesh and the boundary conditions. To establish a mesh in the $(\zeta, \eta)$ spatial domain, we set

$$\Delta\zeta = \frac{1}{J} \quad \text{and} \quad \Delta\eta = \frac{2}{K+1},$$

where $J = 68$ and $K = 33$. Creating the mesh in this fashion agrees with the literature for numerical simulations of Turing systems on a sphere [97] and prolate spheroid [86]. We then define

$$U^n_{j,k} = U\left(j\Delta\zeta, -1 + k\Delta\eta + \frac{\Delta\eta}{2}, n\Delta t\right)$$

to be the numerical approximation to the actual value of $u(\zeta, \eta, t)$, where $j, k, n$ are integers such that $j \in [0, J]$, $k \in [0, K]$, and $n \geq 0$ (similarly, $V^n_{j,k}$ is the approximation to $v(\zeta, \eta, t)$). Creating the mesh in this fashion allows the poles at $\eta = \pm 1$ to be avoided. Values of $\eta$ at mesh points exhibit symmetry about the value $\eta = 0$, further agreeing with the literature for similar numerical simulations of Turing systems [86, 97].

Boundary conditions with respect to $\zeta$ are periodic and given by

$$U^n_{0,k} = U^n_{J,k}, \quad V^n_{0,k} = V^n_{J,k}.$$

Boundary conditions with respect to $\eta$ are employed at the north and south pole of the domain and agree with the literature [86, 97]. The south pole boundary condition is

$$U^n_{j+\frac{J}{2},0} = U^n_{j,0}, \quad V^n_{j+\frac{J}{2},0} = V^n_{j,0},$$

and the north pole boundary condition is

$$U^n_{j+\frac{J}{2},K} = U^n_{j,K}, \quad V^n_{j+\frac{J}{2},K} = V^n_{j,K},$$

where $j \in \left[1, \frac{J}{2}\right]$ in both cases.

Concentration values of $u$ and $v$ are assumed to be normalized about zero and initial $u, v$ values are selected to be random values $\chi \in [-0.5, 0.5]$ along the equator of the prolate spheroid and zero elsewhere, representing the noise that causes a Turing system's steady state to be driven unstable by diffusion [97]. Using these initial conditions in our simulations, we observed Turing systems' intrinsically high sensitivity to initial conditions, as expected [99]. While different random initial conditions yielded different patterns (given a particular set of system parameters), the overall pattern-generating behavior of the system (described below for exponential domain growth and in Chapter 5 for logistic domain growth) remained the same. Thus, for the remainder of this dissertation, all simulations have been created using identically seeded random initial conditions so that we can clearly investigate the pattern-generating behavior of the systems in question. Concentration values are visualized using a concentration gradient where light-colored regions correspond to areas where the concentration of activator $u$ exceeds that of inhibitor $v$ (representing $u > 0$ or equivalently, $v < 0$) and dark-colored regions correspond to areas where the concentration of inhibitor $v$ exceeds that of activator $u$ (representing $u < 0$, or equivalently $v > 0$); for example, refer to Figure B.1.

Stability of the numerical code was verified by several methods. Given a set of initial conditions and system parameters, changing the value of $\Delta t$ or changing the mesh size in the $\zeta$ direction (by doubling, quadrupling, or halving the number of $\zeta$ mesh points) yielded the same pattern, as expected. Mesh size in the $\eta$ direction was not altered from the literature value so as not to alter the amount of error being contributed from the boundary conditions at the poles. Selecting an identical initial condition value at every point at the equator and then perturbing the initial condition (either by changing every value on the equator or by changing just one or two values on the equator) yielded the same pattern, as expected. When using the numerical code to simulate the heat equation $v_t = \Delta v$ with a constant initial condition on the equator (representing the "heat source") and zero elsewhere, we observed that the "heat" spreads over the domain and quickly achieves the same value at every point in the domain, as expected.

System parameters were selected to be

$$D = 0.516, \quad a = 1.112, \quad b = -1.01, \quad C = 0,$$

agreeing with traditional values used for BVM kinetics [8, 50]. Initial interfocal distance was selected to be $f_0 = 2$ and $\xi$ was fixed at $\xi = 1.3141$. This choice of $f_0$ and $\xi$ gave the domain an initial surface area of $4\pi$, matching the surface area of the unit sphere. We fix $\xi$ to fix the domain shape (see Section 3.3) as changing $\xi$ affects the generated pattern [86]. Growth rate $R$ and domain scale $\omega$ were the only parameters varied between simulations and were selected such that the Turing conditions in (4.28) were satisfied.

We observed that patterns produced by exponentially growing domain Turing System (4.23) are transient and evolve continuously from one pattern to another (see Figures 4.1–4.3). This pattern-generating behavior contrasts with that of a comparable Turing system on a static prolate spheroidal domain in which the pattern converges to one final pattern [86, 97]. The addition of exponential domain growth to a Turing system therefore induces a fundamental change in the system's pattern-generating behavior. Our observation of domain growth inducing transient patterns agrees with previous research conducted on Turing systems on exponentially growing spheres [32, 43] and linearly growing spheres [16].

System (4.23) can generate striped or spotted patterns depending on whether BVM parameter $C$ is selected as $C = 0$ or $C > 0$, respectively (see Section 3.2). By electing BVM parameter $C = 0$ for our simulations, we observe striped patterns, similar to a static domain BVM system [9, 21]. As the patterns evolve, they become more complex; that is, one can observe more stripes as elapsed time $t$ increases (see Figures 4.1–4.3). An increase in pattern complexity with increasing time agrees with results in the literature from linearly growing spherical Turing systems [16].

Since simulations varied only in the values of parameters $R$ and $\omega$, we were able to observe that increasing $R$ (given a particular $\omega$) or increasing $\omega$ (given a particular $R$) causes the system to generate a more complex pattern at any given $t > 0$ (see Figure 4.4 or compare Figures 4.1–4.3) . We also noticed that increasing $R$ or $\omega$ increases the frequency at which the pattern evolves from one pattern to another. The correspondence between increasing domain growth rate and overall rate of pattern evolution has been previously observed in the case of linearly growing spherical Turing systems [16].

While we employed $C = 0$ in our simulations, it should be noted that observations analogous to those in the preceding three paragraphs are made for spotted patterns produced by System (4.23) when $C > 0$. Patterns are again transient, with the number of spots increasing as $t$ increases; increasing the value of $R$ or $\omega$ again increases the number of spots generated at a given $t > 0$. An example of a spotted pattern produced by System (4.23) with $C = 1.57$ (the traditional literature value of $C$ used to generate spots with BVM kinetics [8, 49, 50]) is given in Figure 4.5.

## 4.4 Comparison to Static Domain Pattern

As discussed in Section 4.3, a pattern generated by a static prolate spheroidal domain Turing system converges to a final pattern (see Figures 4.6 and 4.7). We also compared static prolate spheroidal domain patterns to exponentially growing domain patterns. We generate the pattern on an exponentially growing domain for a given value of growth rate $R$. At the final pattern ($t_{\text{final}} = 35$), the domain size has grown isotropically by a factor of $e^{Rt_{\text{final}}}$. This scale factor is used to create a static prolate spheroidal domain of the same size. The corresponding static domain pattern is then generated using System (4.23) with $R = 0$. Patterns generated on prolate spheroidal domains with equal final domain size are different, but are qualitatively similar in the number and size of stripes (see Figures 4.8 and 4.9). Our observation of domain size having a directly proportional influence on pattern complexity agrees with previous Turing system research conducted on static prolate spheroidal domains [86] and linearly growing spherical domains [16].

## 4.5 Conclusions

In this chapter, we investigated the effects of implementing exponential domain growth in a Turing system on a prolate spheroid. Linear stability analysis was employed to derive mathematical Turing conditions which allow one to select parameters that ensure the system will generate Turing patterns. Appropriate selection of system parameters that satisfy the Turing conditions and maintain the origin as the unique steady state of the system when

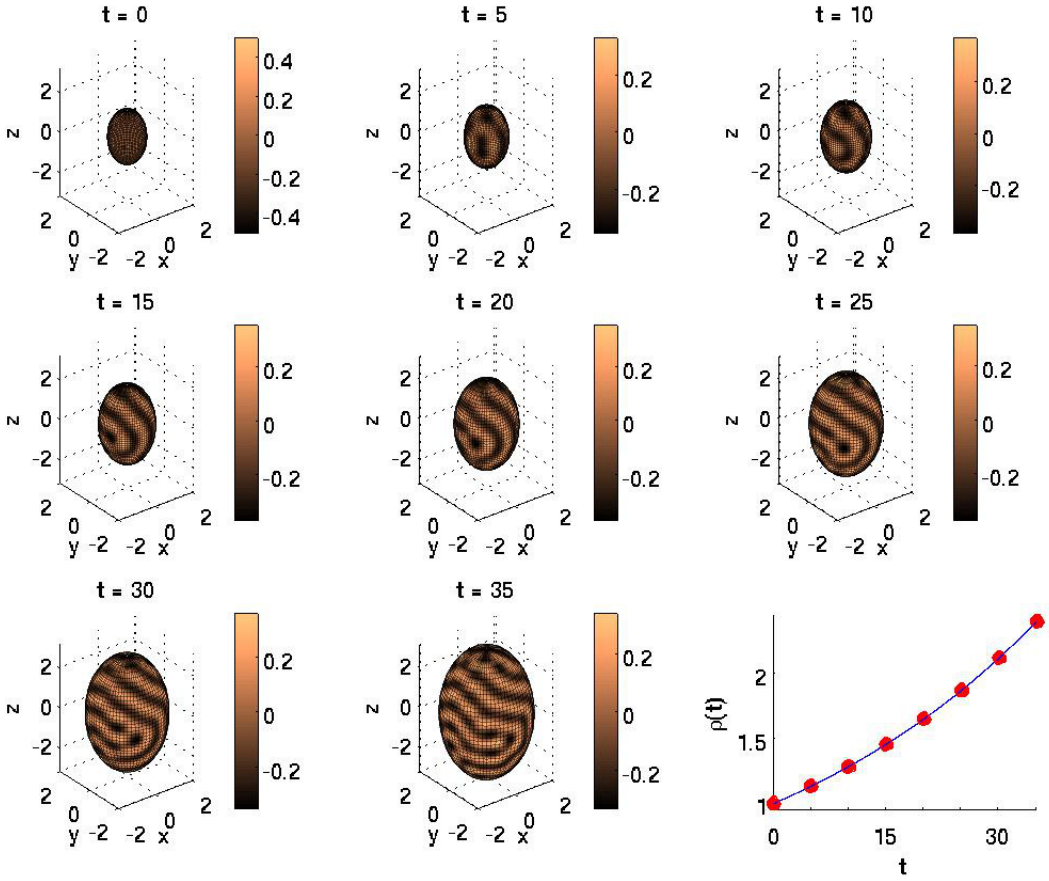


Figure 4.1: Evolution of exponentially growing domain Turing pattern for $R = 0.025, \omega = 115$. The pattern is transient; that is, it evolves as $t$ increases, with pattern complexity increasing with $t$. Light-colored regions represent areas where the concentration of the activator $u$ exceeds that of the inhibitor $v$ ($u > 0$ or equivalently, $v < 0$) and dark-colored regions represent areas where the concentration of the inhibitor $v$ exceeds that of the activator $u$ ($u < 0$, or equivalently $v > 0$). The pattern was generated by System (4.23) with kinetics parameters listed on page 34. Snapshot times are indicated by red dots in the lower right figure. See also: animation.

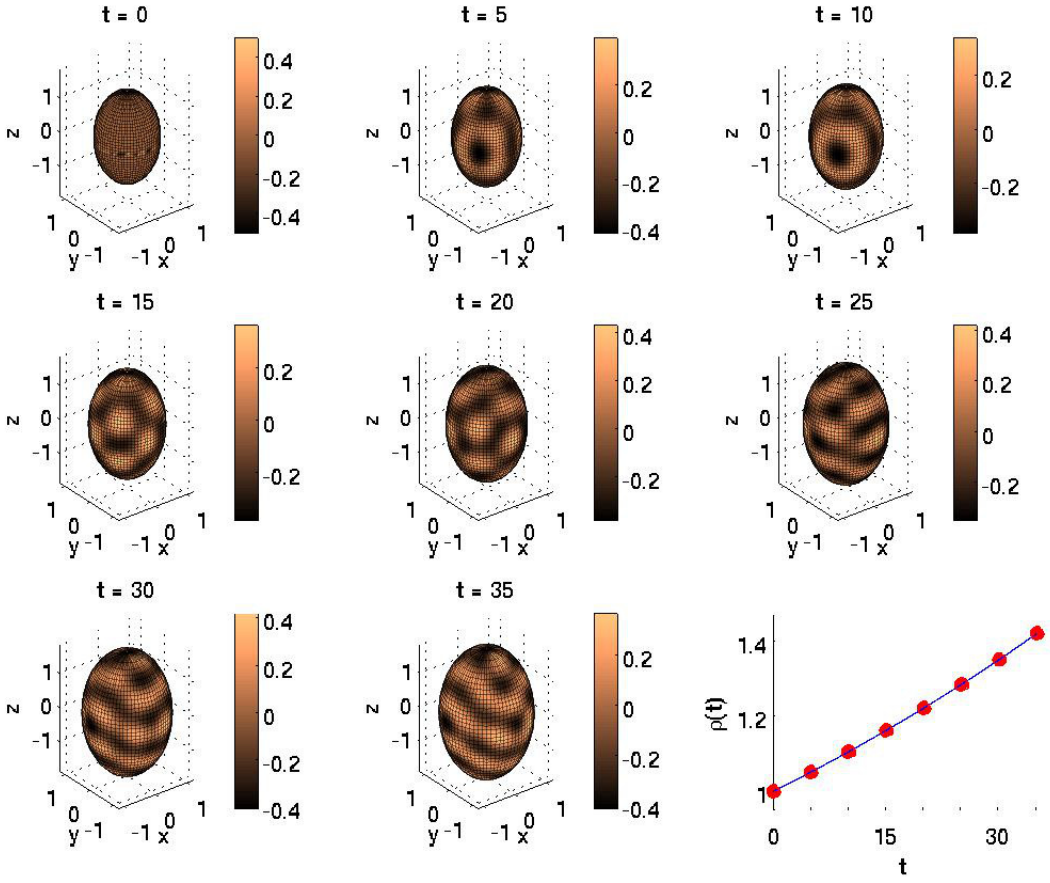


Figure 4.2: Evolution of exponentially growing domain Turing pattern for $R = 0.01, \omega = 115$. Decreasing the value of $R$ yields patterns that are are less complex than those in Figure 4.1 at each corresponding $t$. The pattern was generated by System (4.23) with kinetics parameters listed on page 34. Snapshot times are indicated by red dots in the lower right figure. See also: animation.

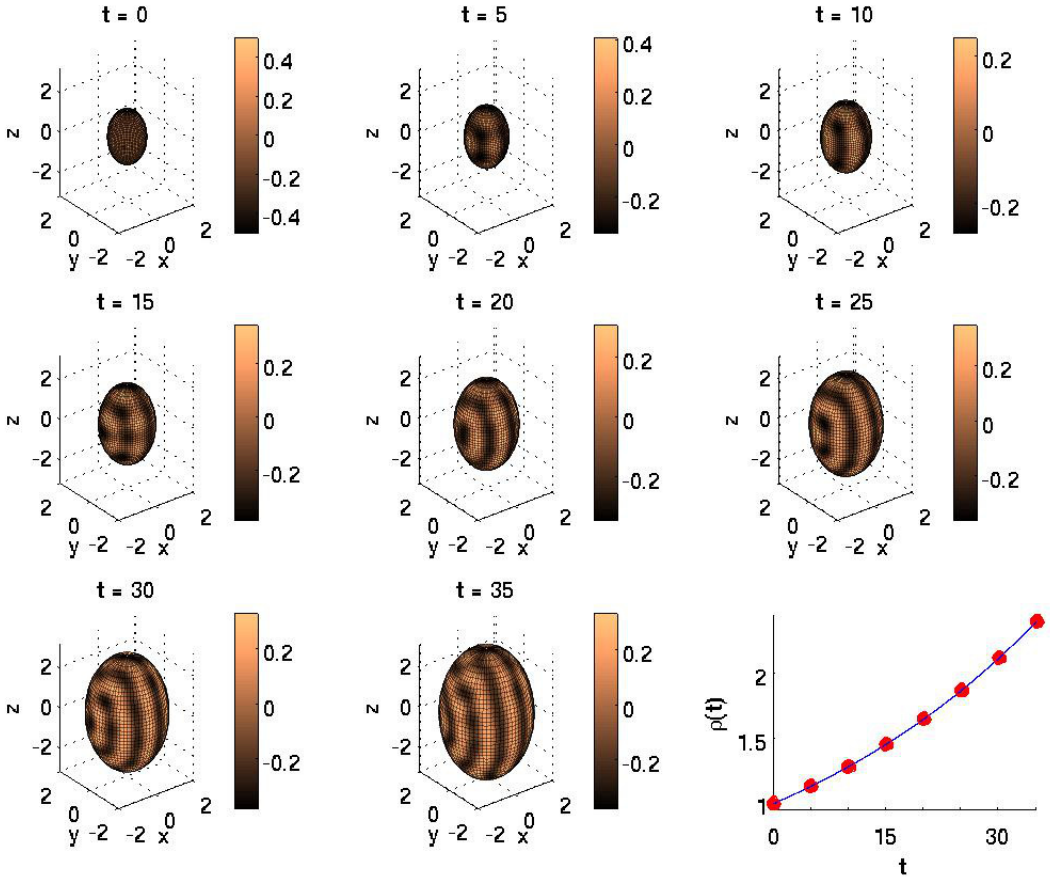


Figure 4.3: Evolution of exponentially growing domain Turing pattern for $R = 0.025, \omega = 70$. Decreasing the value of $\omega$ gives patterns that are less complex than those in Figure 4.1 at corresponding values of $t$. The pattern was generated by System (4.23) with kinetics parameters listed on page 34. Snapshot times are indicated by red dots in the lower right figure. See also: animation.

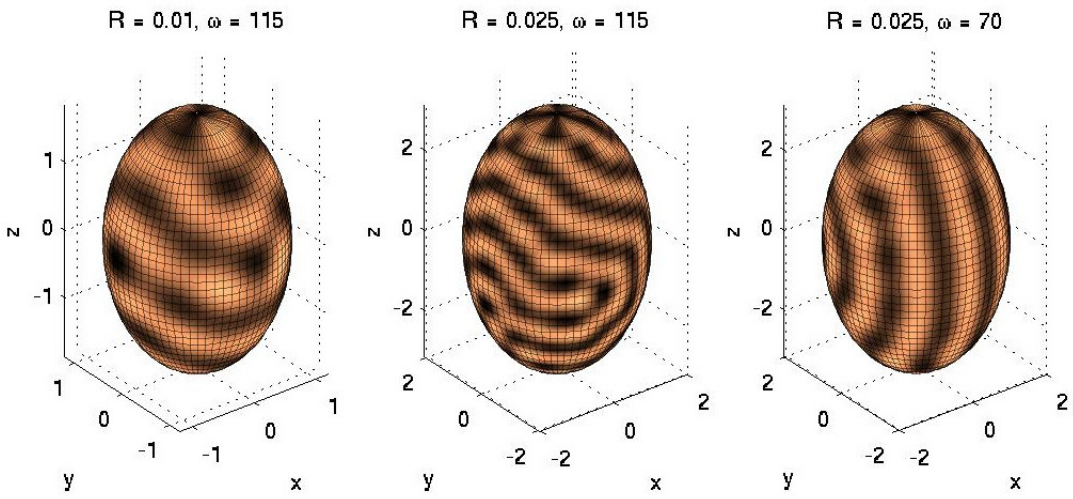


Figure 4.4: Side-by-side comparison of exponentially growing domain Turing patterns for differing values of $R$ and $\omega$ at $t = 35$. Increasing $R$ or $\omega$ results in a more complex pattern at a given value of $t$. The pattern was generated by System (4.23) with kinetics parameters listed on page 34.

using BVM kinetics was discussed. Finally, the pattern-generating behavior of an exponentially growing prolate spheroidal domain Turing system with BVM kinetics was investigated by conducting numerical simulations. These simulations demonstrated that incorporating exponential domain growth into a Turing system causes the patterns to become transient and ever-increasing in complexity. Increasing the value of parameters $R$ or $\omega$ causes the generated pattern to be more complex (more stripes) at a given value of $t > 0$. Domain size has a strong influence on pattern complexity, illustrated by the observation that exponentially growing domain patterns are qualitatively similar to static domain Turing patterns on a corresponding final size domain. In the next chapter, we insert logistic domain growth into System (3.5) and observe that domain growth is the driving force behind pattern transiency in a growing domain Turing system.

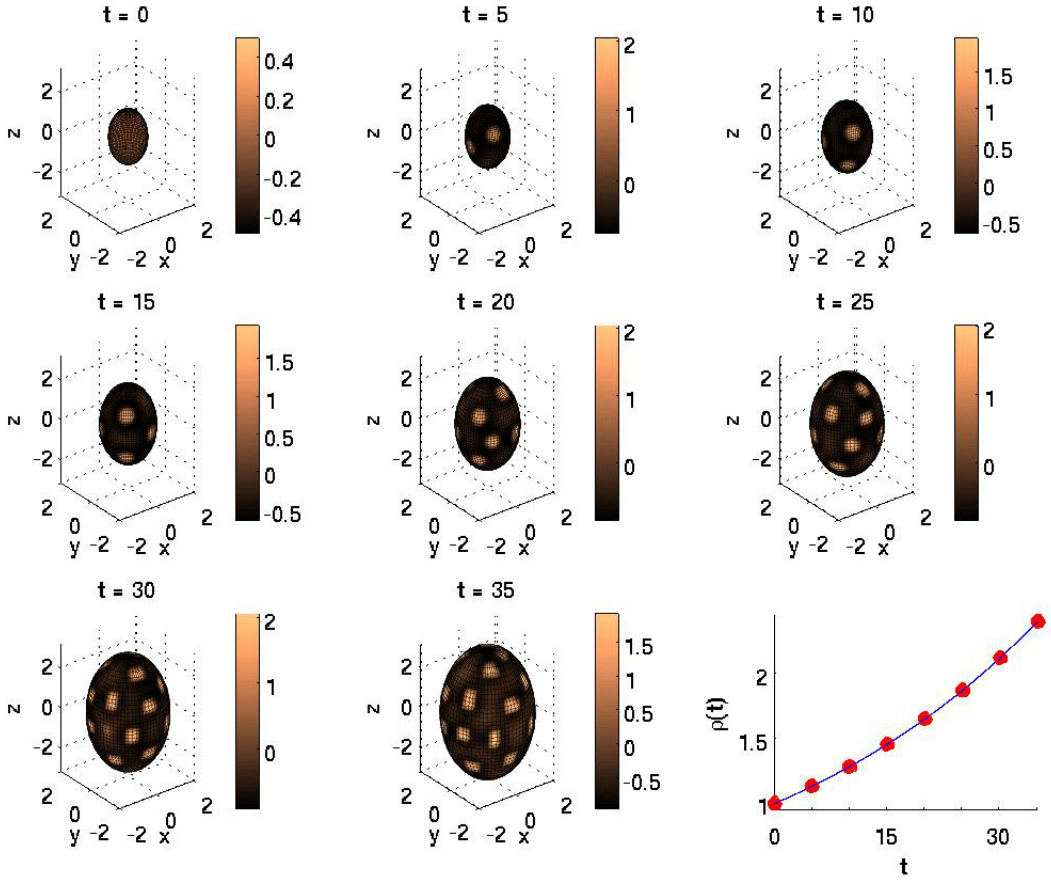


Figure 4.5: Evolution of spotted exponentially growing domain Turing pattern. By selecting $C = 1.57$, System (4.23) generates a transient spotted pattern in which the number of spots increases with $t$. Other system parameters were $R = 0.025, \omega = 70, D = 0.516, a = 1.112, b = -1.01$. Snapshot times are indicated by red dots in the lower right figure. See also: animation.

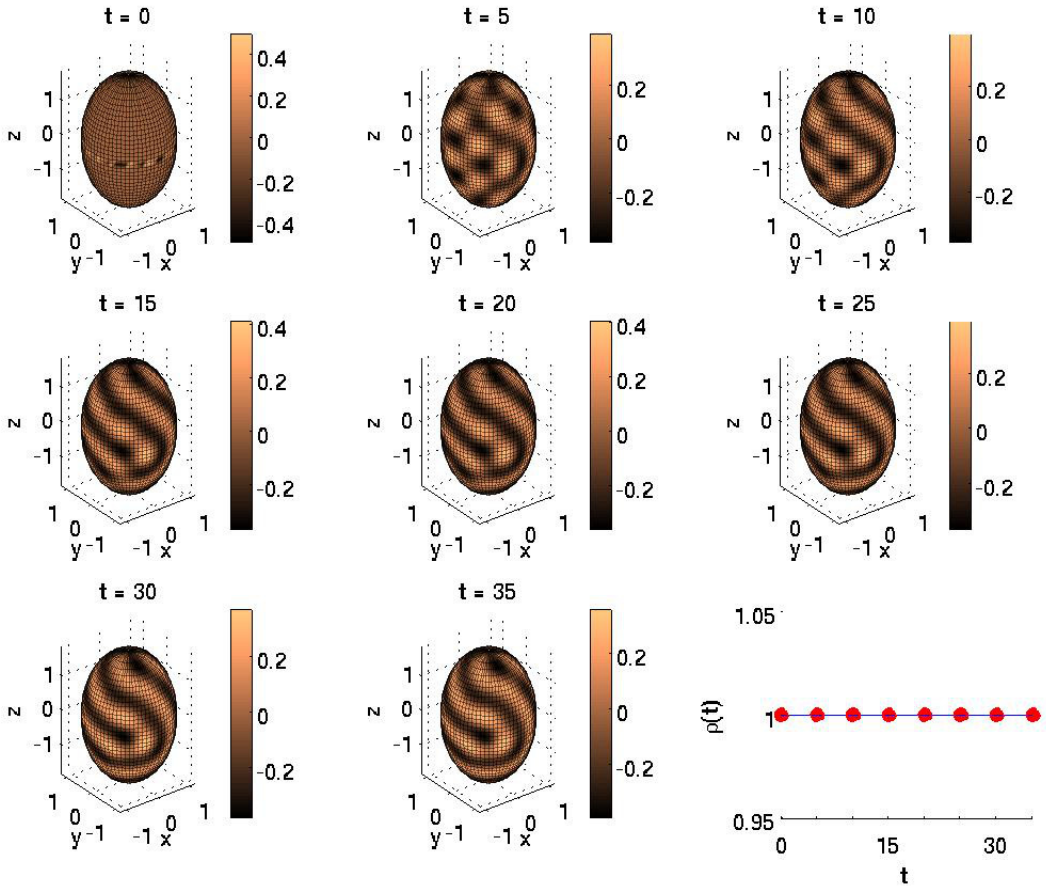


Figure 4.6: Turing pattern on a static domain scaled by $e^{0.01*35}$. The pattern converges to a final pattern due to the lack of domain growth. The pattern was generated by System (4.23) with $R = 0, \omega = 115$, and kinetics parameters listed on page 34. The static domain size equals that of an exponentially growing domain at $t_{\text{final}} = 35$ with $R = 0.01$. Snapshot times are indicated by red dots in the lower right figure.

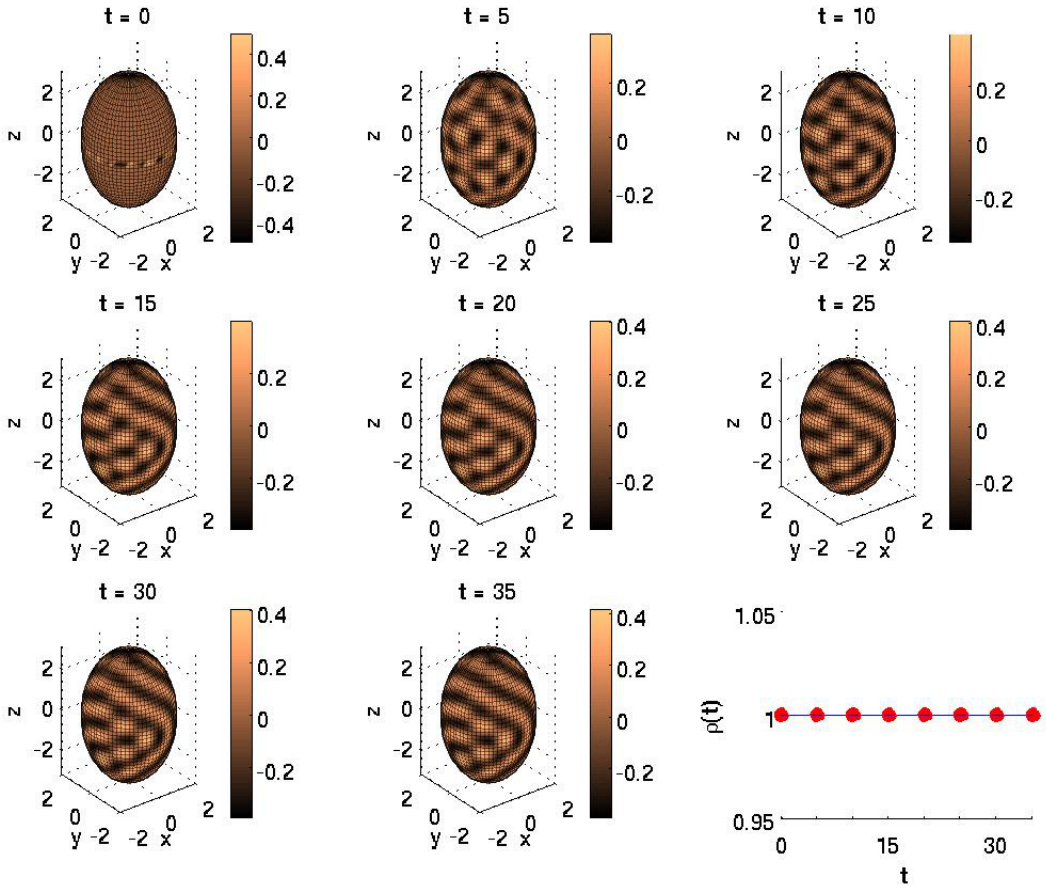


Figure 4.7: Turing pattern on a static domain scaled by $e^{0.025*35}$. The lack of domain growth allows the system to converge to a final pattern. The pattern was generated by System (4.23) with $R = 0, \omega = 70$, and kinetics parameters listed on page 34. The static domain size equals that of an exponentially growing domain at $t_{\text{final}} = 35$ with $R = 0.025$. Snapshot times are indicated by red dots in the lower right figure.

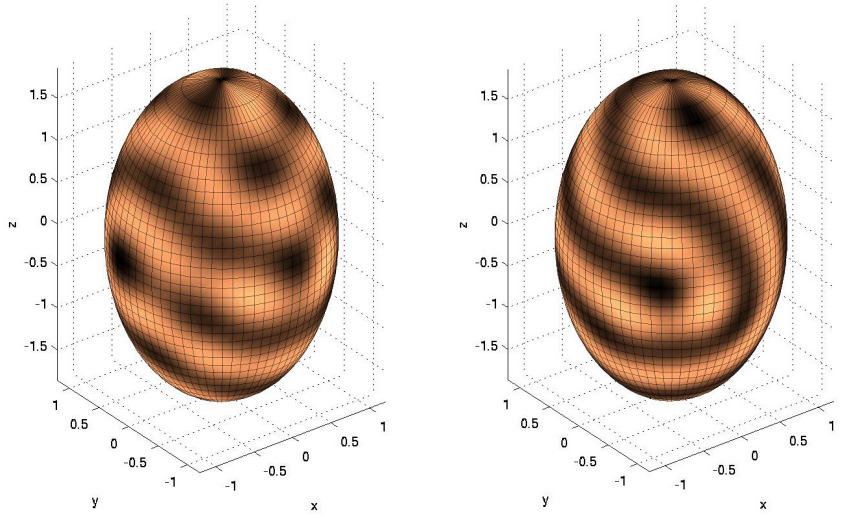


(a) Exponentially growing domain (b) Same-sized static domain

Figure 4.8: Comparison of exponentially growing domain with $R = 0.01$ at $t_{\text{final}} = 35$ and same-sized static domain Turing patterns for $\omega = 115$. A pattern generated on an exponentially growing domain (a) and a same-sized static domain (b) are different, but qualitatively similar in the number and size of stripes due to their shared domain size.

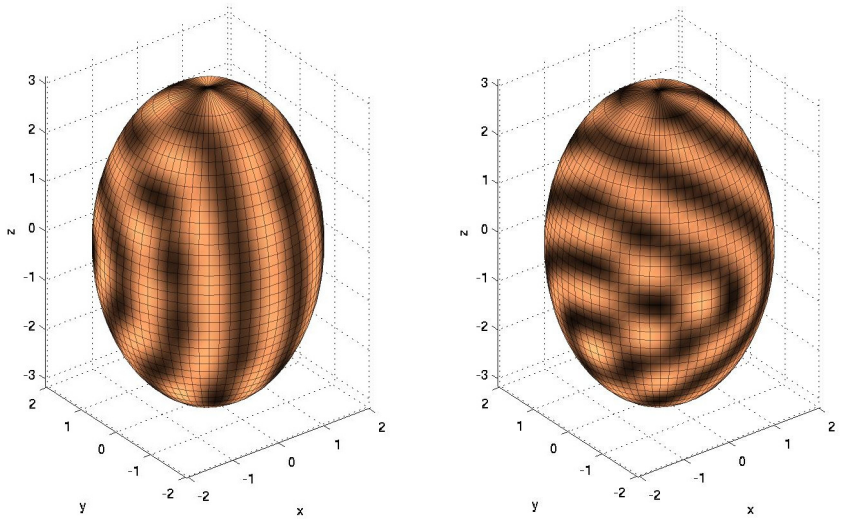


(a) Exponentially growing domain (b) Same-sized static domain

Figure 4.9: Comparison of exponentially growing domain with $R = 0.025$ at $t_{\text{final}} = 35$ and same-sized static domain Turing patterns for $\omega = 70$. Turing systems generate different yet qualitatively similar patterns on an exponentially growing domain (a) and a static domain (b) whose size is equal to the final size of the growing domain.

# CHAPTER 5

# LOGISTICALLY GROWING DOMAIN TURING SYSTEM

To further illustrate the versatility of the growing domain Turing framework, we incorporate logistic domain growth into System (3.5). Logistic growth has been used to model biological phenomena such as population growth, cell division, and tumor growth [63]. Logistic growth is frequently used in biomathematical models due to its high level of biological realism [12, 46, 94]. Organisms cannot continue to grow forever; they eventually stop growing due to constraints of resources or size (or both), and logistic growth models this well.

We first build a logistic growth function that approximates biologically relevant cortical growth data. We then scale this growth function in a way that facilitates comparison between patterns generated by System (3.5) on corresponding prolate spheroidal domains with exponential or logistic domain growth. We demonstrate that although a logistically growing domain does not allow for the derivation of Turing conditions, as explained in Section 5.2, the logistic system is still able to exhibit pattern-forming Turing behavior, which is presented in Section 5.3. These results have been submitted in [91].

## 5.1 Selecting a Logistic Growth Function

To incorporate logistic domain growth into System (3.5), we define $\rho(t)$ to be a logistic growth function. The basic logistic growth function is

$$\rho(t) = \frac{K}{1 + e^{-r(t-t_0)}}, \tag{5.1}$$

where $t \geq 0$, $K$ is the "carrying capacity" or asymptotic value of the curve as $t \to \infty$, $r$ is the logistic growth rate (not to be confused with the exponential growth rate $R$ from exponential growth function $\rho_{\exp}(t) = e^{Rt}$), and $t_0$ allows one to horizontally shift the graph left or right. Since we are constructing a growth function for use in a model of cortical folding, we perform a logistic fit on a modification of the estimated Kinoshita *et al.* [44] germinal matrix volume data points. The data points, which approximate exponential growth, must be modified to appear logistic because without modification, the logistic fit operation returns a curve that resembles exponential growth (see Figure 5.1). The resulting parameter values from the logistic fit are $K = 2.3304, r = 0.6603, t_0 = 19.9258$ (see Figure 5.1).

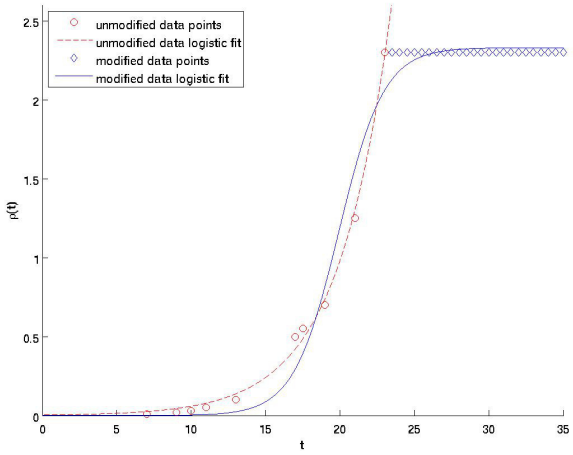


Figure 5.1: Logistic growth curves. The unmodified estimated Kinoshita *et al.* [44] germinal matrix data points (circles) are logistically fit using the basic logistic function (Equation (5.1)) and resemble an exponential growth function (dashed curve). Estimated parameters are $K = 1.8683 \times 10^{13}, r = 0.28137, t_0 = 128.6751$. After modifying the estimated data points by adding repetitions of the final value to the end (diamonds), the fitted logistic function (solid curve) with parameters $K = 2.3304, r = 0.6603, t_0 = 19.9258$ is sigmoidal.

Next, we alter the basic logistic growth function in Equation (5.1) with the intention of comparing domain growth between logistic and exponential growth functions. We change the carrying capacity from $K$ to $K^\star = e^{Rt_{\text{final}}} - 1$ and vertically shift the graph by 1 to give the scaled logistic growth function

$$\rho_{\log}(t) = \frac{K^\star}{1 + e^{-r(t-t_0)}} + 1. \tag{5.2}$$

Equation 5.2 has been scaled so that $\rho_{\exp}(0) \approx \rho_{\log}(0)$ and $\rho_{\exp}(t_{\text{final}}) \approx \rho_{\log}(t_{\text{final}})$ at a chosen time $t_{\text{final}}$ (see Figure 5.2). A growing domain under logistic growth function $\rho_{\log}$ and exponential growth function $\rho_{\exp}$ thus have approximately the same initial and final domain sizes. Controlling the initial and final domain size in this fashion allows for comparison of patterns generated on corresponding exponentially and logistically growing domains.

Using the growth function in Equation (5.2), the dilution term from Equation (3.4) becomes

$$-2\frac{\dot{\rho}}{\rho}\phi = -2L(t)\phi,$$

where

$$L(t) = \frac{r(\rho - 1)}{\rho}\left(1 - \frac{\rho - 1}{K^\star}\right). \tag{5.3}$$

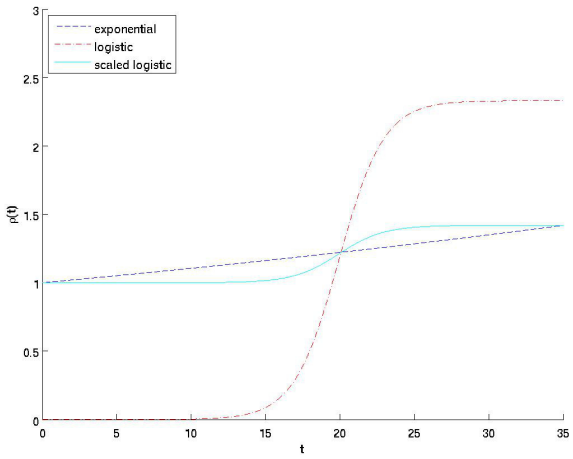


Figure 5.2: Scaled logistic growth curve. Modifying the basic logistic fit curve given by Equation (5.1) (dash-dotted curve) results in the scaled logistic growth curve (solid curve) given by Equation (5.2), which has approximately the same initial and final values as the exponential growth curve $e^{0.01t}$ (dashed curve).

Overall, System (3.5) with logistic growth function $\rho_{\log}(t)$ becomes

$$\left.\begin{aligned} u_t &= \frac{D}{\rho^2}\Delta_\dagger u - 2L(t)u + \omega f(u,v), \\ v_t &= \frac{1}{\rho^2}\Delta_\dagger v - 2L(t)v + \omega g(u,v), \end{aligned}\right\} \tag{5.4}$$

where $L(t)$ is given by Equation (5.3). Notice that unlike the $-2R\phi$ dilution term for the exponentially growing domain (Equation 4.1), the dilution term under logistic domain growth is time-dependent.

## 5.2 Linear Stability Analysis for the Logistically Growing Domain Turing System

We attempt to employ linear stability analysis to obtain Turing conditions for the logistically growing domain System (5.4) in the same manner as for the exponentially growing domain System (4.2) in Section 4.1.1. System (5.4) in the absence of diffusion becomes

$$\begin{aligned} u_t &= -2L(t)u + \omega f(u,v), \\ v_t &= -2L(t)v + \omega g(u,v). \end{aligned}$$

Let $(u_0, v_0)$ be a spatially uniform steady state of System (5.4) that remains a steady state in the absence of diffusion. This implies that $(u_0, v_0)$ is the solution to

$$\begin{aligned} 0 &= -2L(t)u_0 + \omega f(u_0,v_0), \\ 0 &= -2L(t)v_0 + \omega g(u_0,v_0). \end{aligned}$$

Notice that due to the time dependence of the dilution term, the steady state of the system is also time-dependent, so $(u_0, v_0) = (u_0(t), v_0(t))$. Linear stability analysis no longer makes sense because of this time dependence, as the system would need to be re-linearized at each value of $t$; in other words, a unique linear approximation for the system for all $t$ cannot be found.

Since linear stability analysis fails, the time dependence of the dilution term prevents the derivation of Turing conditions for the logistically growing domain System (5.4). This means that we cannot find mathematical conditions that guarantee that System (5.4) will be able to exhibit the characteristic Turing pattern-generating behavior. However, the lack of a guarantee does not rule out the possibility that System (5.4) might still exhibit Turing behavior; in fact, it is able to generate Turing patterns, which we show in the following sections.

## 5.3 Numerical Results

We select nondimensional BVM kinetics so that System (5.4) becomes

$$\left.\begin{aligned} u_t &= \frac{D}{\rho^2}\Delta_\dagger u - 2L(t)u + \omega(u + av - Cuv - uv^2), \\ v_t &= \frac{1}{\rho^2}\Delta_\dagger v - 2L(t)v + \omega(bv + hu + Cuv + uv^2). \end{aligned}\right\} \tag{5.5}$$

To numerically implement System (5.5), we use a forward-time, central-space finite difference scheme coded in FORTRAN. We wish to compare the patterns created by System (4.23) and System (5.5) to investigate the effects of changing domain growth in System (3.5) from exponential to logistic. To accomplish this, our logistic growth numerical simulations had identical kinetics parameters, identical initial conditions, and approximately identical initial and final domain size (as discussed in Section 5.1) as the exponential growth simulations in Section 4.3. We again visualize concentration values with a concentration gradient in which light-colored areas represent regions where activator $u$ has greater concentration than inhibitor $v$ (corresponding to $u > 0$ or equivalently, $v < 0$) and dark-colored areas represent regions where inhibitor $v$ has greater concentration than activator $u$ (corresponding to $u < 0$ or equivalently, $v > 0$). Parameters for the logistic growth function defined in Equation (5.2) were $r = 0.6603, t_0 = 19.9258, K^\star = e^{Rt_{\text{final}}} - 1$ where $R = 0.01$ and $t_{\text{final}} = 35$. The parameter $\omega$ was varied as in Section 4.3.

We observed a key difference in how patterns produced by logistically and exponentially growing domain Turing systems evolve as elapsed time progresses. While patterns on an exponentially growing prolate spheroid continually change and evolve (see Section 4.3), patterns on a logistically growing prolate spheroid exhibit the vast majority of their transiency during the period when the logistic growth curve is rapidly increasing. A "burst" of pattern change is seen concurrently with the "burst" of domain growth provided by the logistic growth curve. Once the domain stops growing (asymptotically), patterns generated on a logistically growing prolate spheroidal domain behave like a pattern produced by a static domain, converging towards one final pattern (see Figures 5.3 and 5.4). Overall, we observe

that transient pattern evolution in a growing domain Turing system is driven by domain growth.

We also observed that increasing the value of the domain scale parameter $\omega$ in a logistically growing prolate spheroid Turing system increases the complexity of the generated pattern at a given $t > 0$, just as in an exponentially growing prolate spheroid Turing system (compare Figures 5.3 and 5.4). Even though they shared identical kinetics parameters, initial conditions, and initial and final domain size, the final patterns produced by System (4.23) and System (5.5) are different, though they are qualitatively similar in the number and size of stripes due to their corresponding final domain size (see Figures 5.5, 5.6). It will be demonstrated in Chapter 6 that increasing the value of $R$, which increases the logistic carrying capacity $K^\star$ and therefore the domain size at a given $t > 0$, increases the complexity of the pattern at a given $t > 0$, again echoing the observations seen in an exponentially growing system.

## 5.4 Piecewise Exponential Growth

We provide further evidence that domain growth drives pattern transiency in a growing domain Turing system. A piecewise growth function consisting of initial and final constant values and a middle exponential growth region can be used to approximate logistic domain growth. We incorporate such a growth function into Turing System (3.5). Consider the piecewise growth function

$$\rho_{\text{pe}}(t) = \begin{cases} a & \text{for } k_1 \leq t < k_2, \\ be^{(R_{\text{pe}})t} & \text{for } k_2 \leq t < k_3, \\ c & \text{for } k_3 \leq t \leq k_4, \end{cases}$$

where $k_i\,(i = 1, \ldots, 4)$ are chosen constants and $R_{\text{pe}}$ is the growth rate for the exponential region. The dilution term from Equation (3.4) becomes

$$-2\frac{\dot{\rho}_{\text{pe}}}{\rho_{\text{pe}}}\phi = \begin{cases} 0 & \text{for } k_1 \leq t < k_2, \\ -2R_{\text{pe}}\phi & \text{for } k_2 \leq t < k_3, \\ 0 & \text{for } k_3 \leq t \leq k_4. \end{cases}$$

Inserting the growth function $\rho_{\text{pe}}(t)$ into System (3.5) still yields System (4.2), but with $R = 0$ for $t \in [k_1, k_2) \cup [k_3, k_4]$ and $R = R_{\text{pe}}$ for $t \in [k_2, k_3)$. The linear stability analysis and Turing conditions in Section 4.1 thus still hold true. When selecting system parameters for System (3.5) with growth function $\rho_{\text{pe}}(t)$, one must check that the parameters satisfy the Turing conditions in (4.20) not only for the exponential growth rate $R = R_{\text{pe}}$ but also for $R = 0$. It is not difficult to find system parameters that meet this requirement, allowing us to confirm that System (3.5) with growth function $\rho_{\text{pe}}(t)$ can exhibit Turing pattern-generating behavior.

To enable comparison of the pattern-generating behavior of a piecewise exponentially growing prolate spheroidal domain Turing system with that of the exponentially or logistically growing domain Turing systems discussed in Sections 4.3 and 5.3, we select parameters

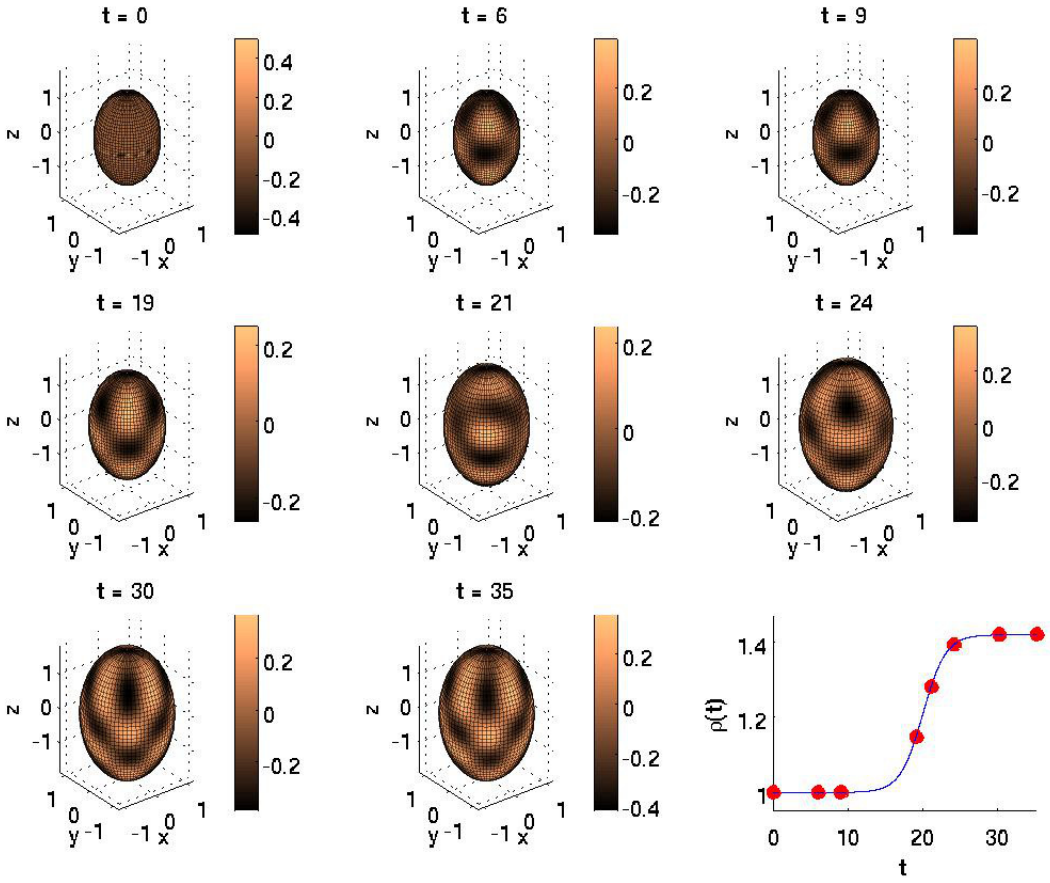


Figure 5.3: Evolution of logistically growing domain Turing pattern with $\omega = 70$. Other parameters are $R = 0.01, t_{\text{final}} = 35, r = 0.6603, t_0 = 19.9258, K^\star = e^{Rt_{\text{final}}} - 1$. The pattern changes rapidly when the growth curve rapidly increases but does not change much when the growth curve is flat. The system converges to a final pattern once the domain asymptotically stops growing. The pattern was generated by System (5.5) with kinetics parameters listed on page 34. Snapshot times are indicated by red dots in the lower right figure. See also: animation.

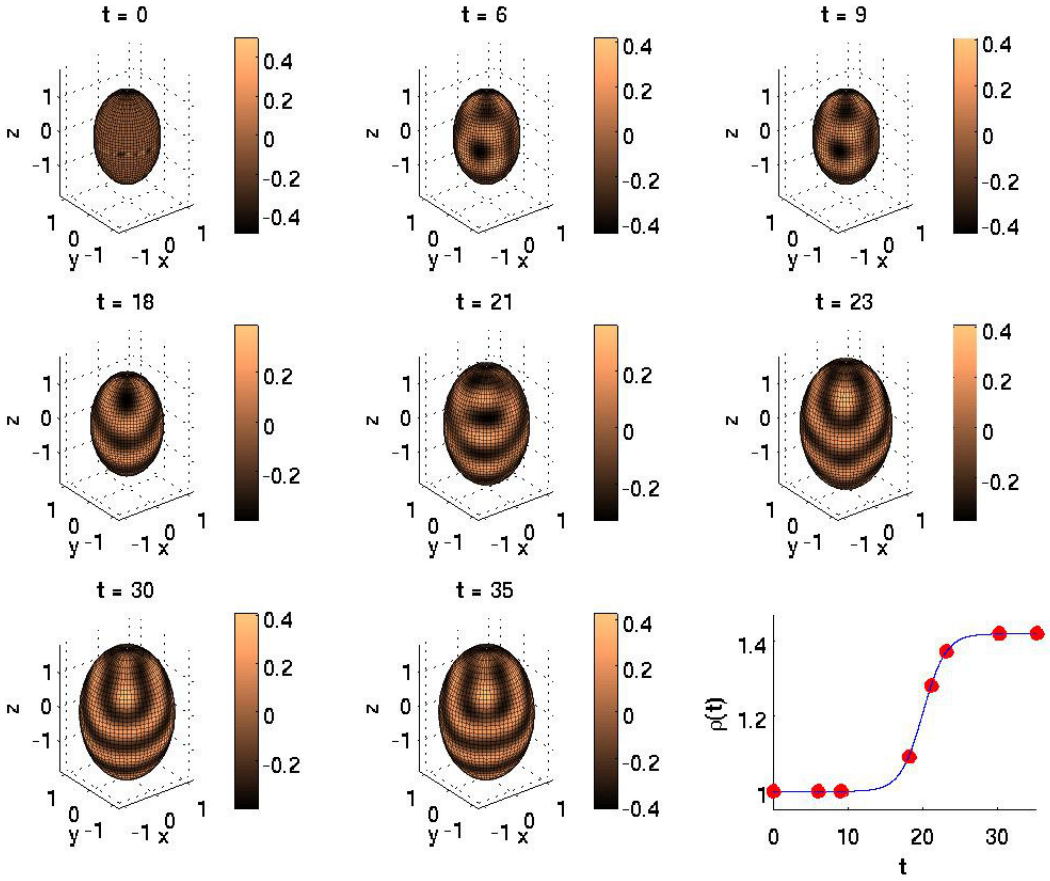


Figure 5.4: Evolution of logistically growing domain Turing pattern with $\omega = 115$. Other parameters are $R = 0.01, t_{\text{final}} = 35, r = 0.6603, t_0 = 19.9258, K^\star = e^{Rt_{\text{final}}} - 1$. Patterns at corresponding values of $t$ are more complex than those in Figure 5.3 due to the increased value of $\omega$. The pattern was generated by System (5.5) with kinetics parameters listed on page 34. Snapshot times are indicated by red dots in the lower right figure. See also: animation.

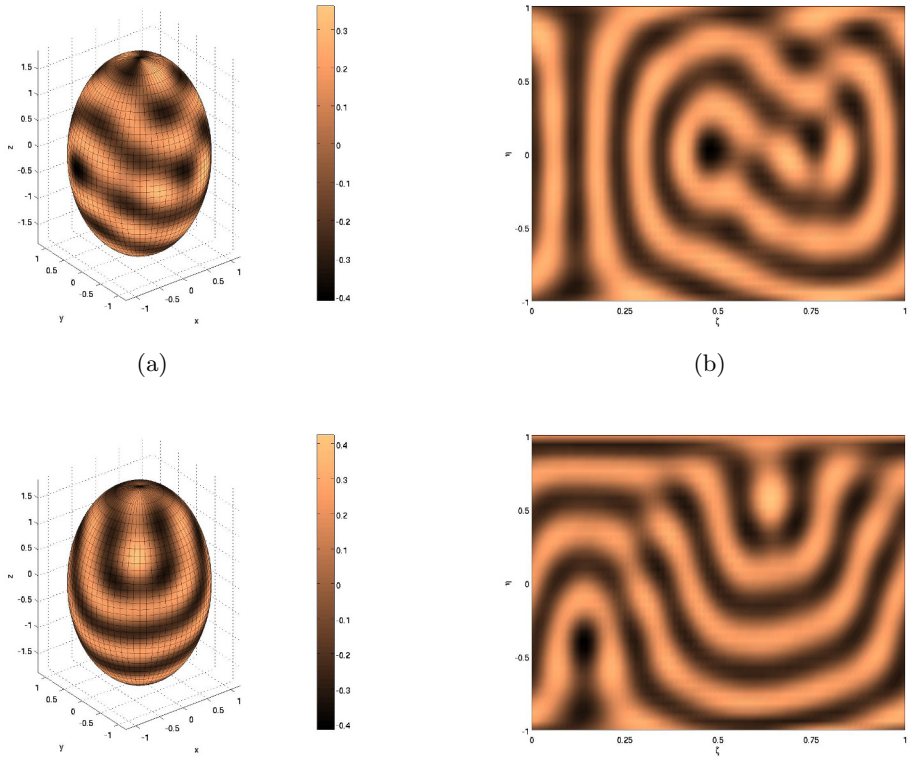

(a) (b)

(c) (d)

Figure 5.5: Comparison of patterns on exponentially and logistically growing prolate spheroidal domains for $R = 0.01, \omega = 115$ at $t_{\text{final}} = 35$. Figures (a),(b) show the pattern produced by System (4.23) on an exponentially growing prolate spheroid. Figures (c),(d) show the pattern produced by System (5.5) on a logistically growing prolate spheroid with $r = 0.6603, t_0 = 19.9258, K^\star = e^{Rt_{\text{final}}} - 1$. Kinetics parameters used in both cases are listed on page 34. Figures (a),(c) represent the patterns on the prolate spheroid, while figures (b),(d) represent the patterns on their computational domain. The patterns are different, even though both simulations had approximately the same initial and final domain size and used identical initial conditions, diffusion coefficient, and kinetics parameters. The patterns are qualitatively similar in the number and size of stripes due to their corresponding final domain size.

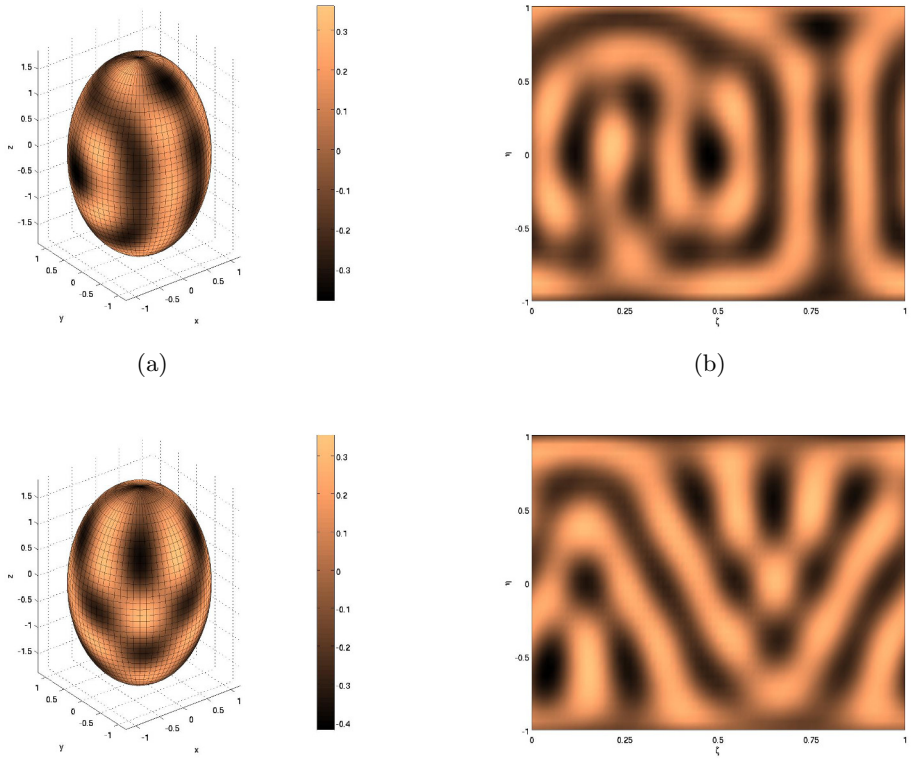

(a) (b)

(c) (d)

Figure 5.6: Comparison of patterns on exponentially and logistically growing prolate spheroidal domains for $R = 0.01, \omega = 70$ at $t_{\text{final}} = 35$. Figures (a),(b) show the pattern produced by System (4.23) on an exponentially growing prolate spheroid. Figures (c),(d) show the pattern produced by System (5.5) on a logistically growing prolate spheroid with $r = 0.6603, t_0 = 19.9258, K^\star = e^{Rt_{\text{final}}} - 1$. Kinetics parameters used in both cases are listed on page 34. Figures (a),(c) show the patterns on the prolate spheroid; figures (b),(d) show the patterns on their computational domain. Patterns produced using different growth functions are different despite being produced by systems that had nearly identical initial and final domain size, identical initial conditions, and identical kinetics and diffusion parameters. The patterns are qualitatively similar in the number and size of stripes due to their corresponding final domain size.

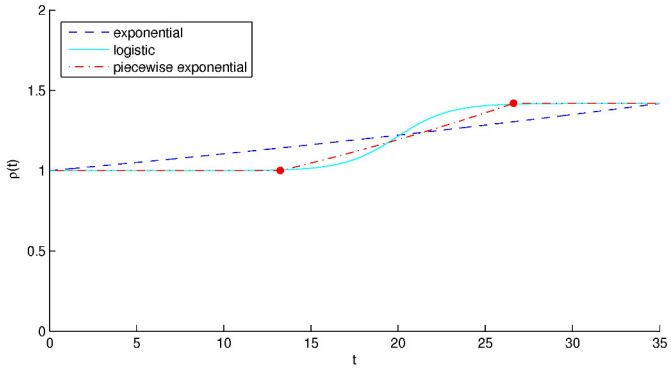


Figure 5.7: Comparison of growth functions. Depicted are three different growth functions where $R = 0.01$: $\rho_{\exp}(t) = e^{Rt}$ (dashed curve), $\rho_{\log}(t)$ defined by Equation (5.2) with $r = 0.6603, t_0 = 19.9258, t_{\text{final}} = 35, K^\star = e^{Rt_{\text{final}}} - 1$ (solid curve), and $\rho_{\text{pe}}(t)$ given in Equation (5.6) (dash-dot curve). The plotted points $(13.2366, 1)$ and $(26.6150, e^{0.01*35})$ were used to find the exponential portion of $\rho_{\text{pe}}(t)$ via best exponential fit.

for $\rho_{\text{pe}}(t)$ such that

$$\rho_{\text{pe}}(t) = \begin{cases} 1 & \text{for } 0 \le t < 13.2366, \\ 0.7073e^{0.02616t} & \text{for } 13.2366 \le t < 26.6150, \\ e^{Rt_{\text{final}}} & \text{for } 26.6150 \le t \le 35 = t_{\text{final}}, \end{cases} \tag{5.6}$$

where $R = 0.01$ and the middle function is obtained by performing a best exponential fit between the points $(13.2366, 1)$ and $(26.6150, e^{Rt_{\text{final}}})$. These specific points were selected to construct a $\rho_{\text{pe}}(t)$ with exponential growth occurring concurrently with the rapid increase portion of $\rho_{\log}(t)$ (see Figure 5.7); this was accomplished by finding where $\rho_{\log}(t)$ is $\epsilon$ away from its initial and final asymptotic values of 1 and $e^{0.01*35}$, where $\epsilon$ was chosen to be $\epsilon = 0.005$. Choosing the parameters for $\rho_{\text{pe}}(t)$ in this way also allows all three growth functions $\rho_{\exp}, \rho_{\log}, \rho_{\text{pe}}$ to have approximately the same initial and final values so that their corresponding Turing systems have approximately the same initial and final domain sizes.

### 5.4.1 Numerical Results

We implement System (3.5) with nondimensional BVM kinetics and growth function $\rho_{\text{pe}}(t)$ defined in Equation (5.6) using a FORTRAN forward-time, central-space finite difference scheme. To allow comparison with the exponentially or logistically growing prolate spheroid Turing systems discussed in Sections 4.3 and 5.3, we select system parameters and initial conditions as in Sections 4.3 and 5.3. Considering the observations from Sections 4.3 and 5.3, Turing patterns generated on a piecewise exponentially growing prolate spheroidal domain behave as expected: patterns exhibit the vast majority of their evolution during the period of exponential domain growth, while converging to a pattern when the domain is not growing (see Figure 5.8). Patterns can exhibit small amounts of transiency during the initial constant portion of the growth curve, as some pattern evolution is to be expected during

the initial development of any Turing pattern (even on a static domain). Once the domain begins to grow during the middle exponential portion of the growth curve, the generated pattern becomes highly transient and increases in complexity, similar to the exponentially growing domain patterns in Section 4.3. When the final constant part of the growth curve is reached, the system converges to a final pattern. These observations combined with the results from Sections 4.3 and 5.3 clearly show that domain growth drives pattern change in a growing domain Turing system.

## 5.5 Conclusions

In this chapter, we developed a logistic growth function that allowed comparisons of patterns generated by exponentially and logistically growing prolate spheroids. After observing the pattern-generating behavior of a logistically growing prolate spheroidal Turing system, we concluded that domain growth drives pattern transiency in a growing domain Turing system. Observing the pattern-generating behavior of a comparable piecewise-exponentially growing prolate spheroid further supported this conclusion. As in Chapter 4, we noted that increasing the value of parameters $R$ or $\omega$ in a logistically growing Turing system gives a more complex pattern at a given $t > 0$. In the next chapter, we utilize the growing domain Turing systems presented in Chapters 4 and 5 to construct growing domain Turing system models of cortical folding patterns in the brain.

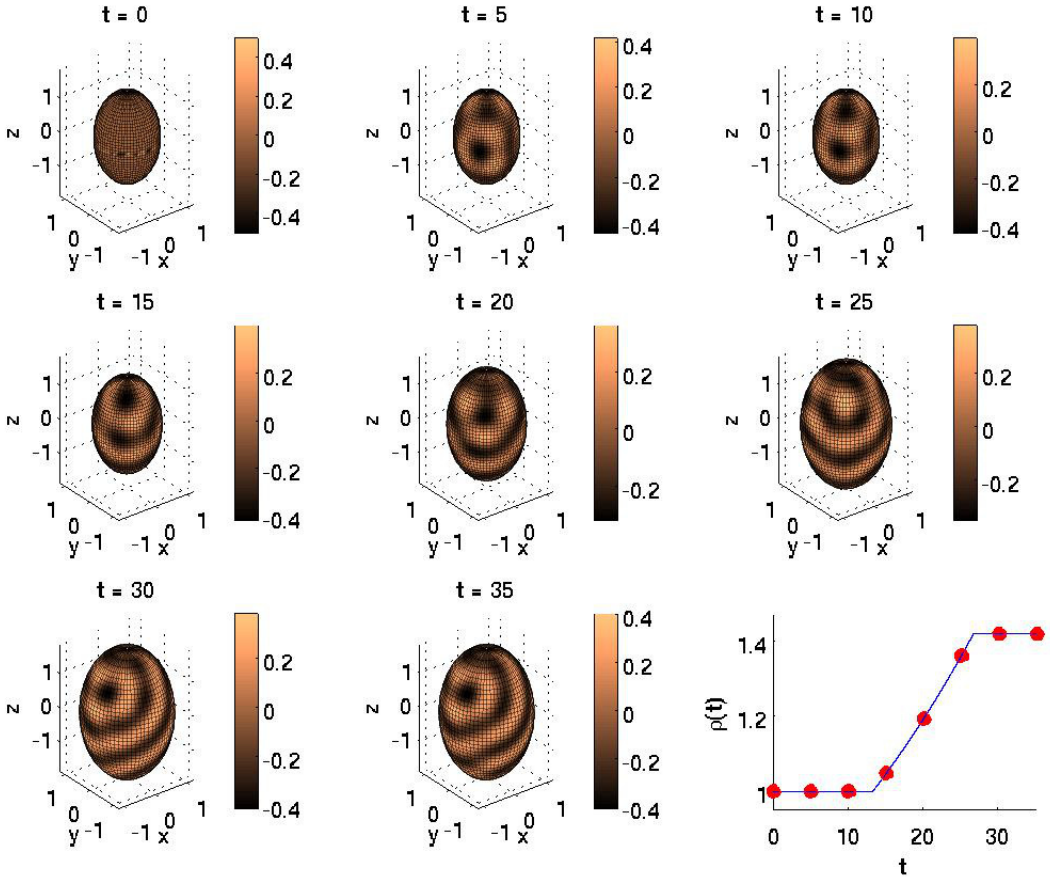


Figure 5.8: Pattern generated by System (3.5) on a piecewise exponentially growing prolate spheroid with growth function defined in Equation (5.6) and $\omega = 115$. Kinetics parameters used are listed on page 34. The pattern changes during the period of domain growth and converges when domain growth stops. Dots in the bottom right figure indicate when the individual snapshots were taken. See also: animation.

# CHAPTER 6

# GROWING DOMAIN TURING MODELS OF CORTICAL FOLDING

In this chapter, we use the exponentially and logistically growing prolate spheroidal domain Turing systems discussed in Chapters 4 and 5 to create two separate yet related growing domain models of cortical folding. Motivation for using a growing prolate spheroidal domain Turing system to model the development of cortical folding patterns is presented. The connection between patterns generated by our model systems and the biology of cortical folding pattern development is discussed. The mathematical models are then utilized to model various manifestations of polymicrogyria and lissencephaly, two types of human diseases of cortical folding which present with too many or too few cortical folds [4, 65, 68, 79]. Advantages and drawbacks of the exponential growth model when compared to the logistic growth model are also discussed. The exponential modeling results have appeared in [90] and have been submitted in [91]; logistic modeling results have been submitted in [91].

## 6.1 Motivation: Connecting the Math to the Biology

The original aim of Turing systems was to model chemical morphogen concentration gradient patterns on a developing embryo [95]. Since cortical folding may be controlled via a genetic chemical gradient (see Section 2.2), a Turing system is a reasonable choice for our biomathematical models of cortical folding. Previous Turing system models of cortical folding used a static domain, failing to capture the natural growth that occurs as the brain develops [86]. We address this shortcoming by incorporating a dynamically growing domain into a Turing system model of cortical folding. We apply our model with exponential domain growth (presented in Section 6.2.1) as well as our model with logistic domain growth (presented in Section 6.2.2) to cortical folding.

Recall that our model investigates the viability of the Intermediate Progenitor Model (IPM), and the key biological processes hypothesized in the IPM take place in the subventricular zone (SVZ). Thus, we must select an appropriate geometric domain to represent the SVZ in our model. We select a prolate spheroidal domain which grows according to a chosen type of growth function. The growing prolate spheroidal domain models the lateral ventricle (LV), while the domain surface models the SVZ. Early in neurogenesis, which occurs from weeks 7-18 gestational age (GA) in humans [75], the cerebral hemispheres are


(a)

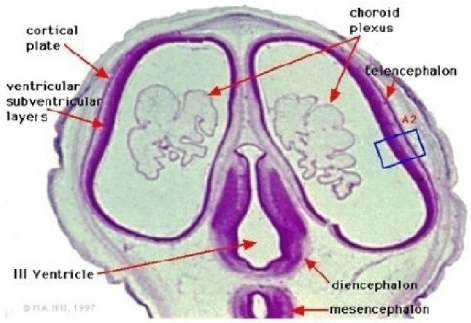


(b)

Figure 6.1: Brain, lateral ventricles, and fetus early in development. The cerebral hemispheres (yellow arrow in Figure (a)) are prolate spheroidal in shape at 48 days GA; since the LVs occupy nearly the entire volume of the developing cerebral hemispheres at 54-56 days GA, they are therefore prolate spheroidal in shape (see Figure (b)). Figure (a) adapted from [26]; Figure (b) from [38].

prolate spheroidal in shape, with the LVs accounting for the nearly the entire volume of the cerebral hemispheres (see Figure 6.1) [26, 36, 38, 86]. It follows that the LVs are also prolate spheroidal in shape at this time, making a prolate spheroid a reasonable choice to represent the LV in our model. Since the SVZ lines the walls of the LV (see Section 2.1.2), the prolate spheroid's surface is a reasonable choice to represent the SVZ.

We assume the existence of an activator morphogen which drives intermediate progenitor cells (IPCs) to self-amplify and an inhibitor morphogen which prevents IPCs from self-amplifying; the existence of such morphogens is supported by evidence showing that IPCs are controlled by genetic gradients (see Section 2.2). The concentration of activator morphogen is represented by $u$ and the concentration of inhibitor morphogen is represented by $v$. Concentration values are assumed to be normalized about zero such that areas with $u = 0$ (equivalently, $v = 0$) represent regions where the concentration of activator and inhibitor are exactly equal, areas with $u > 0$ (equivalently, $v < 0$) represent activated regions where the concentration of activator exceeds that of inhibitor, and areas with $u < 0$ (equivalently, $v > 0$) represent nonactivated regions where the concentration of inhibitor exceeds that of activator (see figures of simulation results, for example Figures 4.1–4.3, where light-colored regions represent $u > 0$ and dark-colored regions represent $u < 0$).

Patterns created by the model Turing systems on the domain surface can represent a genetic chemical prepattern [62, 63] of regions of activation and nonactivation for IPC self-amplification in the SVZ. According to the IPM, IPCs would respond to activated regions by undergoing self-amplification, leading to gyrus formation; IPCs in nonactivated regions would not undergo self-amplification, leading to sulcus formation (see Figure 6.2a). Plotting the final value of $u$ on the $z$-axis against the $(\zeta, \eta)$ computational domain allows one to visualize the development of a labyrinthine cortical folding pattern [13, 86] that could evolve from a Turing prepattern via the IPM (see Figure 6.2b). Visualizing a labyrinthine Turing pattern in this fashion was previously done in the case of a static rectangular domain

Turing system model of cortical folding [13]. Alternatively, one can obtain a visualization of a labyrinthine cortical folding pattern on the prolate spheroidal surface by adding $u$ to the radial coordinate $\xi$ at each mesh point and projecting the result onto the final prolate spheroidal domain (see Figure 6.2c). Using activator concentration to proportionally deform the domain surface in this fashion has been previously utilized in a Turing model of tumor growth on a linearly growing spherical domain [16]. Animations have been created for each pattern evolution figure and each labyrinthine visualization figure in this chapter. In sum, our models create prepatterns for regional IPC self-amplification that could then determine the location of cortical folds via the IPM; in other words, the IPM provides the link between mathematical Turing pattern and biological cortical folding pattern in our models.

## 6.2 Growing Domains for Cortical Folding

### 6.2.1 Exponentially Growing Model

We select exponential domain growth for our first Turing model of cortical folding. Recall that the SVZ is the site of self-amplification of IPCs, and regional patterning of IPC self-amplification could lead to cortical fold locations via the IPM. Since the SVZ produces (and contains) the germinal matrix (GM), which grows exponentially at a time during which IPCs proliferate and cortical folds begin to form in humans (see Section 2.1.3 and Figure 2.6), an exponentially growing domain is a reasonable choice for our model. Additionally, the cerebral hemispheres have been observed to grow exponentially from week 8-13 GA [10] and the cerebral hemispheres' volume is dominated by the LVs and other ventricles through week 16 GA [36], further supporting the use of exponential growth in our model.

Our exponential growth model utilizes System (4.23), a Turing system with nondimensional BVM kinetics on an exponentially growing prolate spheroidal domain. The values of BVM kinetics parameters utilized in our simulations are listed on page 34. As we will demonstrate in the following sections, this model of cortical folding can qualitatively model both normal cortical folding and abnormal (diseased) cortical folding by altering system parameters $R$ and $\omega$ to represent changes in LV size and level of overall genetic expression of activator and inhibitor morphogens [90]. This technique of modifying system parameters to represent changes in genetic expression has been previously employed in other biomathematical Turing models of cortical folding [47]. In particular, we are able to model different presentations of polymicrogyria and lissencephaly, which are discussed in Section 6.3.

### 6.2.2 Logistically Growing Model

For our second growing domain Turing model of cortical folding, we select logistic domain growth. As discussed in Section 5.1, our logistic growth function is formed via a logistic fit on a modification of the estimated Kinoshita *et al.* [44] germinal matrix volume data points, then scaled to allow for comparison with the exponentially growing model. Using logistic growth in a growing domain Turing model of cortical folding allows the prolate spheroidal domain to grow rapidly, then (asymptotically) stop growing. Since the prolate spheroidal domain represents the LV, which will eventually stop growing along with the rest of the brain, logistic growth is a biologically realistic choice for a model of cortical

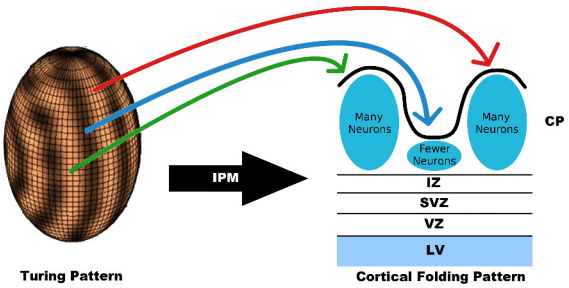


(a) Turing prepattern for cortical folding

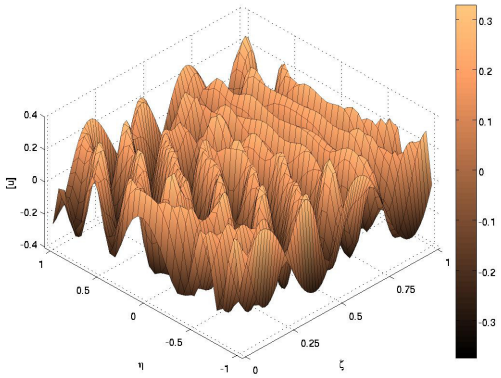

(b) Labyrinthine visualization on computational domain

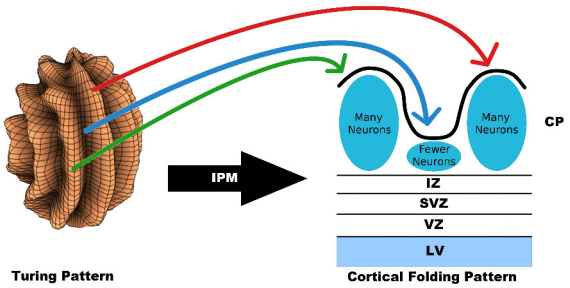


(c) Labyrinthine visualization on prolate spheroid

Figure 6.2: The Intermediate Progenitor Model provides the link between the mathematics and the biology in our Turing system models of cortical folding patterns. Light areas ($u > 0$) in the Turing pattern represent activated regions where IPCs would undergo many rounds of self-amplification; dark areas ($u < 0$) represent nonactivated regions where IPCs would not self-amplify (Figure (a)). This cortical folding prepattern could lead to folding patterns of gyri and sulci (Figures (b) and (c)). Refer to Section 2.2.3 for more details on the IPM. See also: animations.

folding. As discussed in Sections 4.3 and 5.3, Turing patterns on an exponentially growing domain continually evolve, while Turing patterns on a logistically growing domain eventually converge to a final pattern. Since a final cortical folding pattern is eventually established, a logistically growing domain model captures the generation of cortical folding patterns more realistically than an exponentially growing domain model.

Our logistic growth model of cortical folding uses System (5.5), a Turing system with nondimensional BVM kinetics on a logistically growing prolate spheroidal domain. The values of BVM kinetics parameters used in our simulations are listed on page 34. As is the case for our exponentially growing model, we can alter system parameters $R$ and $\omega$ to represent changes in LV size and genetic morphogen expression so that our logistically growing model of cortical folding can qualitatively model certain diseases of cortical folding, which are discussed in the following section.

## 6.3 Modeling Diseases of Cortical Folding

Our growing prolate spheroidal domain models of cortical folding can be employed to model diseases of cortical folding in which the number and size of folds or the size of the LVs are different from normal development. As discussed in Sections 4.3 and 5.3, increasing $R$ or $\omega$ increases the complexity of the pattern at a given $t > 0$, yielding more numerous, thinner stripes. Altering the value of $R$ allows us to control the size of the domain and thus the size of the LV. In the case of exponential growth, increasing or decreasing $R$ respectively increases or decreases the exponential growth rate, therefore increasing or decreasing the size of the domain (representing the size of the LV) at a given $t > 0$. For logistic growth, increasing or decreasing $R$ respectively increases or decreases the carrying capacity $K^\star = e^{Rt_{\text{final}}} - 1$ of the logistic growth function in Equation 5.2, again yielding a larger domain at a given $t > 0$ for larger values of $R$. Recalling that parameter $\omega$ allows one to control the strength of the reaction terms relative to the dilution and diffusion terms in a growing domain Turing system, increasing or decreasing the value of $\omega$ represents a respective increase or decrease in the overall level of genetic expression of activator and inhibitor morphogens $u$ and $v$.

We alter both $R$ and $\omega$ to control the complexity of the pattern to model various manifestations of polymicrogyria and lissencephaly. To do this, we must establish a reference set of values which represent normal LV size and genetic expression level, thus giving a normal cortical folding pattern (via a prepattern for IPC self-amplification as discussed in Section 6.1). We select $R = 0.015$ to correspond to a normal-sized LV and $\omega = 115$ to represent normal activator-inhibitor genetic expression, so that the number and size of stripes in the pattern given by System (4.23) or (5.5) with $R = 0.015, \omega = 115$ represents normal development of the cortical folding pattern. Finally, since patterns generated by exponentially growing System (4.23) continually evolve without end, we must select a value of $t$ to represent the "final" pattern generated by the system, which will be interpreted by IPCs as a prepattern for self-amplification. Since the pattern generated by logistically growing System (5.5) has converged by $t = 35$, we select $t = 35$ as the time at which we stop our exponentially growing simulations. Figures in this section therefore show the final pattern generated at $t = 35$ by the corresponding model simulation.

### 6.3.1 Polymicrogyria

Polymicrogyria (PMG) is the common name given to a group of diseases of cortical folding in which the folds of the cortex are unusually high in number and small in size [4]. Patients suffering from PMG often exhibit mental retardation, epilepsy, and developmental delay. Mutations in *Pax6* and *GPR56* have been linked to some forms of PMG [35, 71]. Several different types of PMG are accompanied by enlarged LVs, such as megalencephaly PMG with polydactyly and hydrocephalus (see Figure 6.3a) [17], bilateral frontoparietal PMG (see Figure 6.3b) [4, 15, 87], and unilateral PMG (see Figure 6.3c) [70].

As discussed above, we model normal cortical folding using $R = 0.015, \omega = 115$. The evolving pattern for exponential domain growth from $t = 0$ to $t = 35$ is shown in Figure 6.4, and the corresponding labyrinthine visualizations are shown in Figures 6.5 and 6.6. Using our models, we capture various forms of PMG by altering the values of $R$ and $\omega$. Results are summarized in Table 6.1 and Figures 6.7 and 6.8, which show the final pattern (at $t = 35$) for exponential and logistic growth, respectively. For example, Figures 6.7a–6.7c (corresponding to the last time step of Figures 6.4–6.6) and Figures 6.8a–6.8c show normal patterns for exponential and logistic growth, while Figures 6.7d–6.7i and Figures 6.8d–6.8i show various representations of PMG. Details are discussed in the following paragraphs. The full corresponding pattern evolution and labyrinthine visualization figures are found in Appendix B.

To model polymicrogyria with enlarged LVs, our model systems utilize $\omega = 115$ and capture LV enlargement by increasing the value of $R$ to $R = 0.021$, causing the prolate spheroidal domain (representing the LV) to be larger as explained in Section 6.3. Using a larger $R$ results in a more complex pattern with an increased number and decreased width of stripes when compared to the normal pattern. Recalling that the pattern produced by our model can represent a prepattern for cortical folding via the IPM, this can be interpreted as an increased number of smaller cortical folds, modeling the characteristic manifestation of polymicrogyria. The final patterns for PMG with enlarged LVs are shown in Figures 6.7d–6.7f and 6.8d–6.8f.

In certain types of PMG, such as some cases of bilateral frontoparietal PMG, patients present with microcephaly (smaller than normal brain and head), yet are still reported to have enlarged LVs (see Figure 6.3d) [15, 71]. The literature is unclear as to whether or not these enlarged LVs are actually bigger than normal-sized ventricles in a normal-sized brain (see Figure 6.3e). We thus capture enlarged LVs within a microcephalic brain by employing the value of $R = 0.015$ used for normal-sized LVs, making the assumption that enlarged LVs in a microcephalic brain are approximately the size of normal LVs in a normocephalic (normal-sized) brain. The needed polymicrogyric pattern can then be generated with $\omega = 150$, representing an increase in overall genetic expression of $u$ and $v$. The result of employing $R = 0.015, \omega = 150$ in System (4.23) and (5.5) to model PMG with microcephaly and enlarged LVs can be seen in Figures 6.7g–6.7i and 6.8g–6.8i, respectively. The generated patterns again exhibit an increased number and decreased size of stripes relative to the normal patterns, representing polymicrogyria.

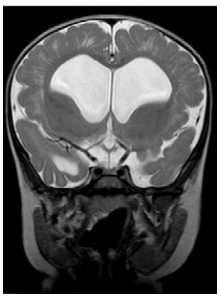

(a) Megalencephaly PMG with polydactyly and hydrocephalus

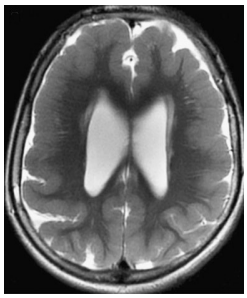

(b) Bilateral frontoparietal polymicrogyria

(c) Unilateral polymicrogyria

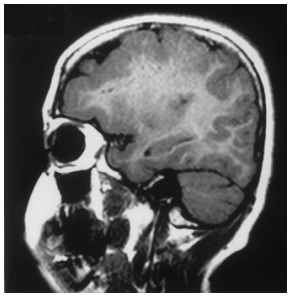

(d) Bilateral frontoparietal polymicrogyria with microcephaly

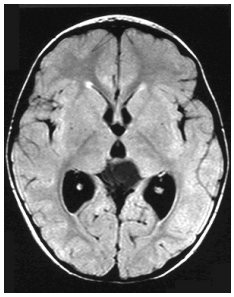

(e) Normal brain

Figure 6.3: MRI images illustrating different types of polymicrogyria. In megalencephaly PMG with polydactyly and hydrocephalus ((a), figure from [17]) and bilateral frontoparietal polymicrogyria ((b), figure from [4]), both sides of the brain feature PMG and enlarged lateral ventricles. In unilateral polymicrogyria ((c), figure from [70]), PMG is seen on the side of the brain with the enlarged LV, while the side of the brain with a normal-sized LV exhibits normal cortical folding. Some cases of bilateral frontoparietal PMG present with microcephaly ((d), figure from [15].) A brain with normal cortical folding pattern and normal-sized LVs is shown in (e) (figure from [40]).

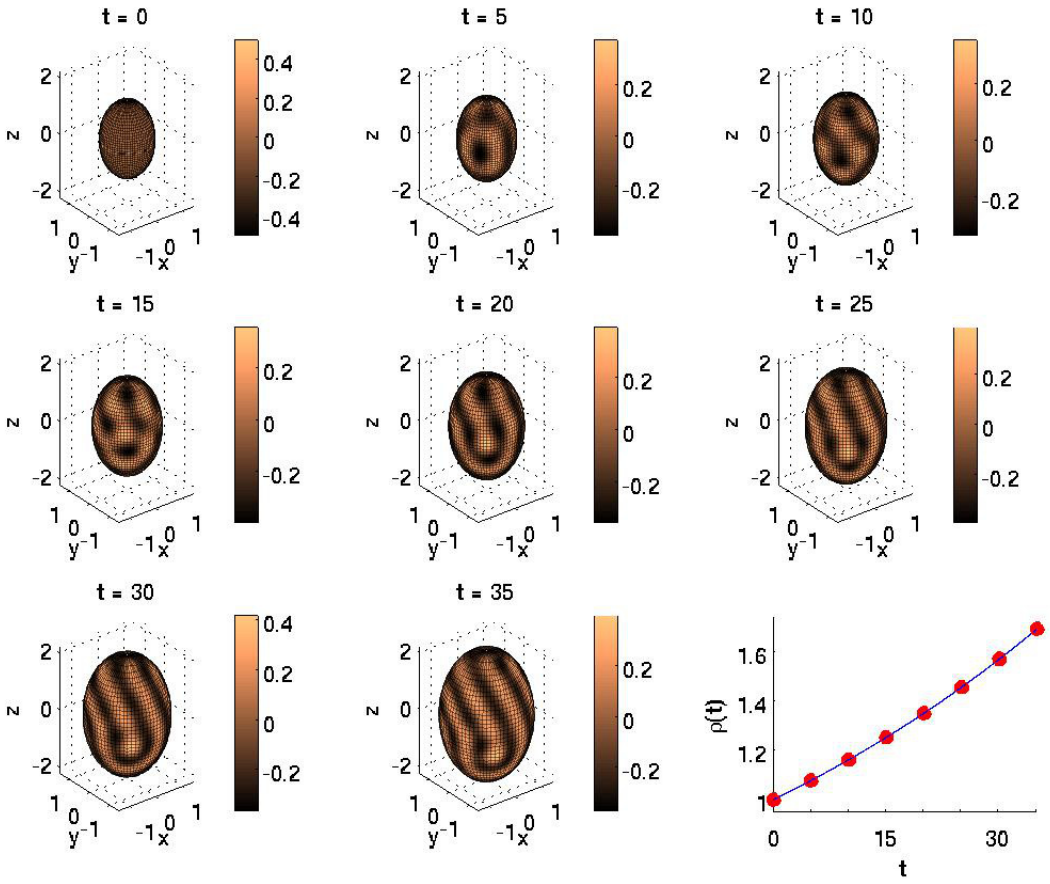


Figure 6.4: Evolution of Turing pattern on an exponentially growing prolate spheroid representing normal cortical development. The pattern was generated by System (4.23) with $R = 0.015, \omega = 115$ and kinetics parameters listed on page 34. Red dots on the bottom right figure represent times at which the snapshots were taken. See also: animation.

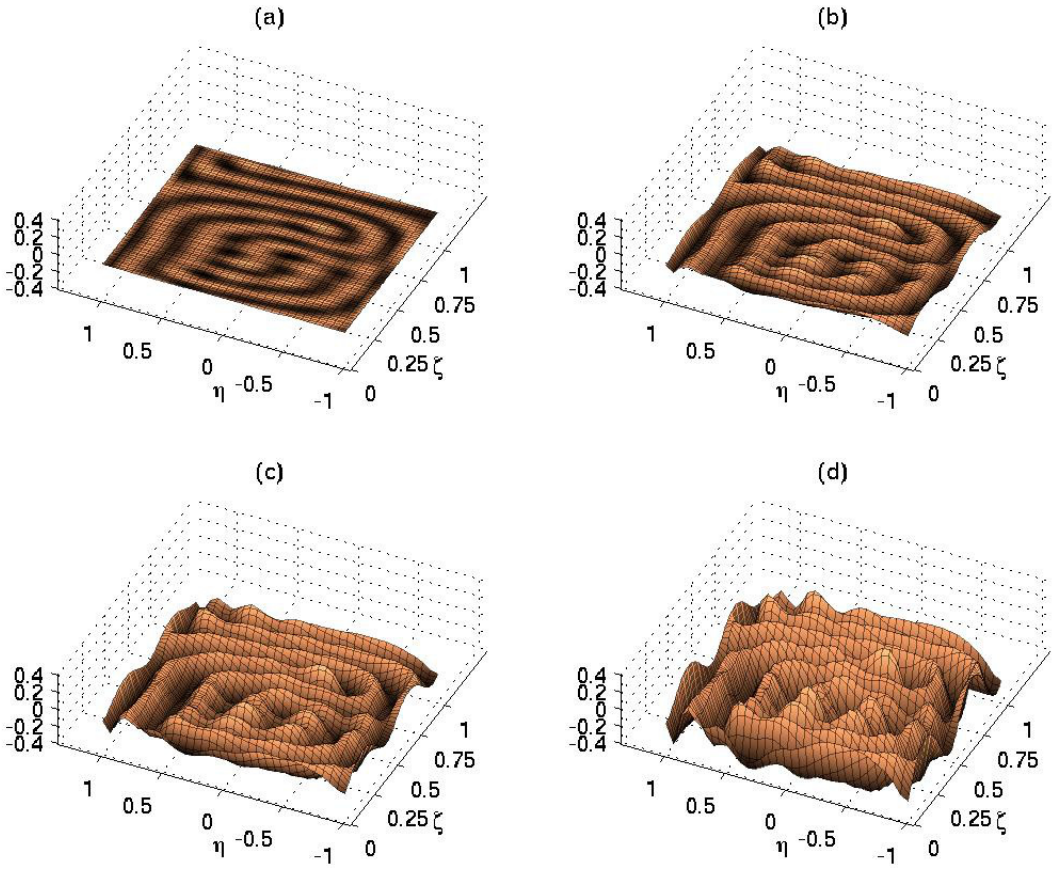


Figure 6.5: Exponential growing domain Turing pattern as a prepattern for normal cortical fold development. Figures (a) through (d) provide a visualization of how a labyrinthine cortical folding pattern could develop from a genetic chemical Turing prepattern by plotting the activator concentration $u$ on the $z$-axis for $z = 0$, $z = \frac{u}{4}$, $z = \frac{u}{2}$, and $z = u$, respectively. The pattern represents normal cortical development and corresponds to the final pattern in Figure 6.4. See also: animation.

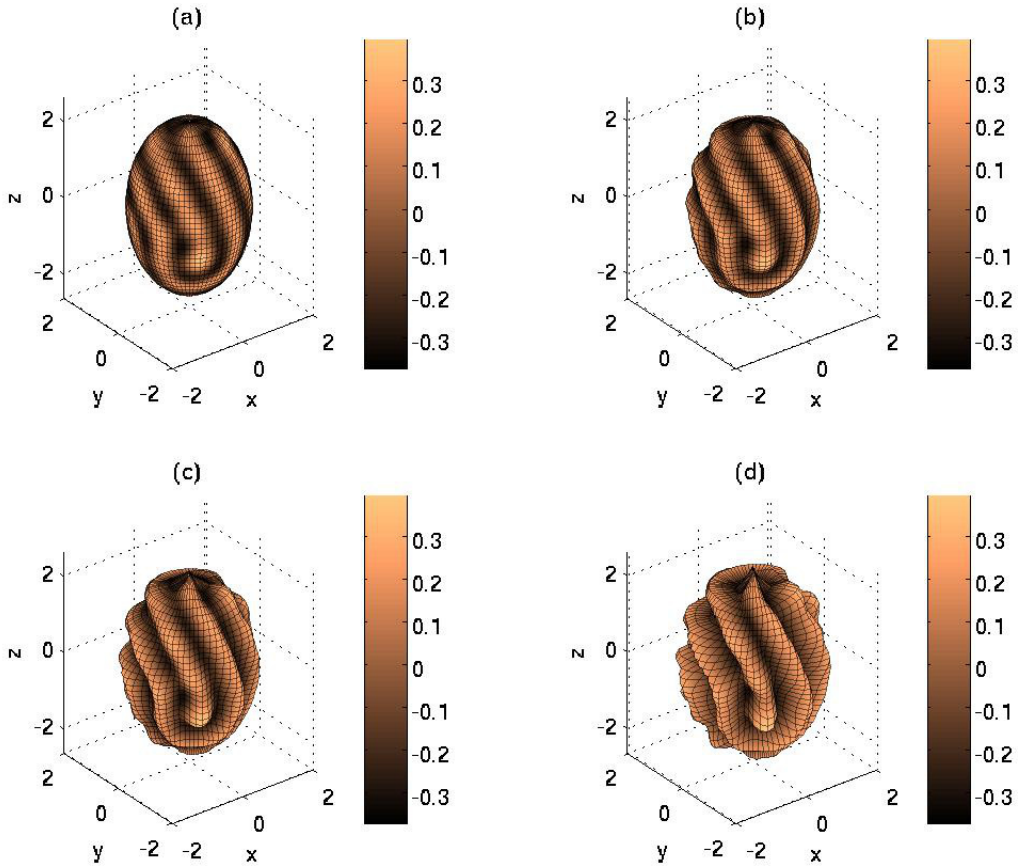


Figure 6.6: Prolate spheroid visualization of exponentially growing domain Turing prepattern for normal cortical fold development. Projecting the images from Figure 6.5 onto the corresponding prolate spheroidal domain gives a new way to visualize how a labyrinthine pattern representing normal cortical folding could develop from a chemical Turing prepattern (refer to Figure 6.4 at $t = 35$). See also: animation.

Table 6.1: Polymicrogyria simulation results. Simulation results are summarized in Figures 6.7 and 6.8. Full pattern evolution and labyrinthine visualization figures are in Appendix B.

| Growth Function | Figure Type | Normal ($R = 0.015$, $\omega = 115$) | PMG, enlarged LVs ($R = 0.021$, $\omega = 115$) | PMG, microcephaly, enlarged LVs ($R = 0.015$, $\omega = 150$) |
|---|---|---|---|---|
| Exponential | Prolate spheroid prepattern | Figs. 6.7a, B.1 | Figs. 6.7d, B.4 | Figs. 6.7g, B.7 |
| | Rectangular domain folding pattern | Figs. 6.7b, B.2 | Figs. 6.7e, B.5 | Figs. 6.7h, B.8 |
| | Prolate spheroid folding pattern | Figs. 6.7c, B.3 | Figs. 6.7f, B.6 | Figs. 6.7i, B.9 |
| Logistic | Prolate spheroid prepattern | Figs. 6.8a, B.19 | Figs. 6.8d, B.22 | Figs. 6.8g, B.25 |
| | Rectangular domain folding pattern | Figs. 6.8b, B.20 | Figs. 6.8e, B.23 | Figs. 6.8h, B.26 |
| | Prolate spheroid folding pattern | Figs. 6.8c, B.21 | Figs. 6.8f, B.24 | Figs. 6.8i, B.27 |

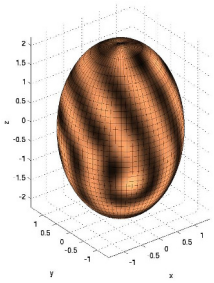

(a) Normal: $R = 0.015, \omega = 115$

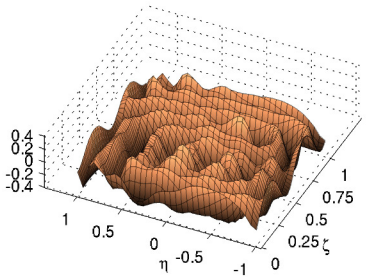


(b) Folding pattern from (a)

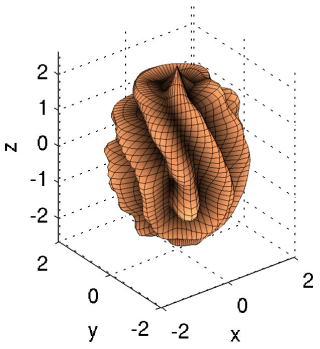


(c) Projection of (b)

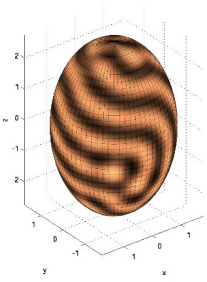

(d) PMG with enlarged LVs: $R = 0.021, \omega = 115$

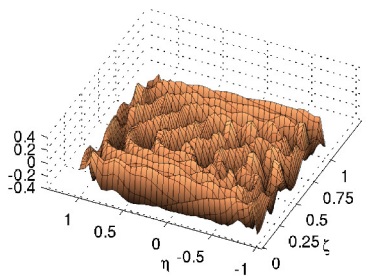


(e) Folding pattern from (d)

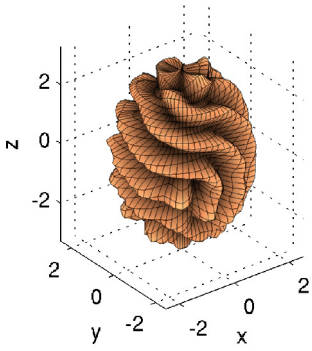


(f) Projection of (e)

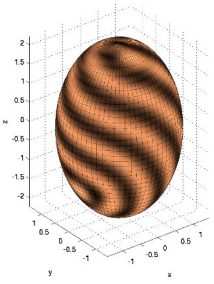

(g) PMG, microcephaly, enlarged LVs: $R = 0.015, \omega = 150$

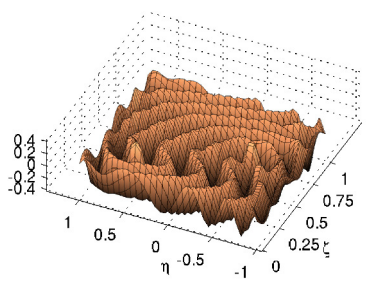


(h) Folding pattern from (g)

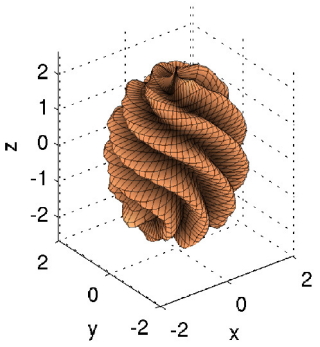


(i) Projection of (h)

Figure 6.7: Modeling polymicrogyria on an exponentially growing prolate spheroid. The generated PMG prepatterns exhibit an increased number and decreased width of stripes (figures (d)–(i)) relative to the normal patterns (figures (a)–(c)). The center and right columns show how a labyrinthine cortical folding pattern could develop from the corresponding Turing genetic chemical prepattern in the left column. See Figures B.1–B.9 for the corresponding pattern evolution and labyrinthine visualization figures.

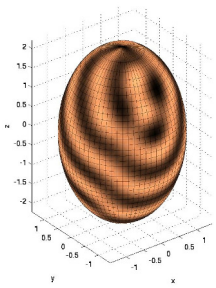

(a) Normal: $R = 0.015, \omega = 115$

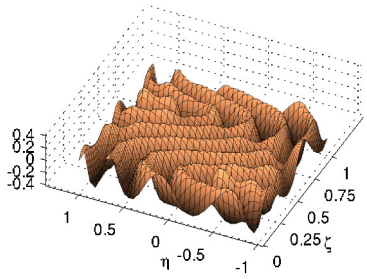


(b) Folding pattern from (a)

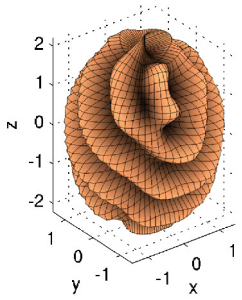


(c) Projection of (b)

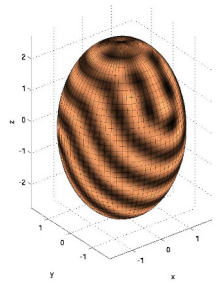

(d) PMG with enlarged LVs: $R = 0.021, \omega = 115$

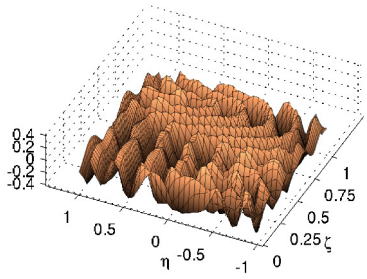


(e) Folding pattern from (d)

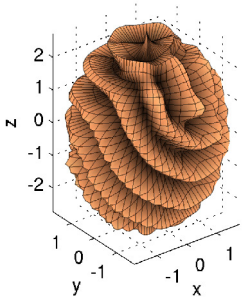


(f) Projection of (e)

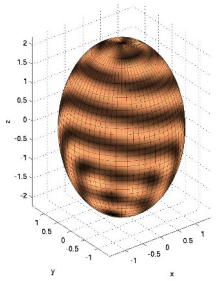

(g) PMG, microcephaly, enlarged LVs: $R = 0.015, \omega = 150$

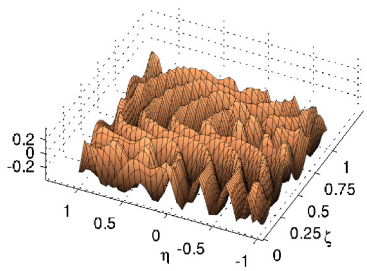


(h) Folding pattern from (g)

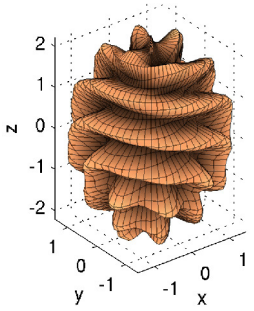


(i) Projection of (h)

Figure 6.8: Modeling polymicrogyria on a logistically growing prolate spheroid. The generated PMG prepatterns exhibit an increased number and decreased width of stripes (figures (d)–(i)) relative to the normal patterns (figures (a)–(c)). The center and right columns show how a labyrinthine cortical folding pattern could develop from the corresponding Turing genetic chemical prepattern in the left column. See Figures B.19–B.27 for the corresponding pattern evolution and labyrinthine visualization figures.

### 6.3.2 Lissencephaly

Type I lissencephaly, also called classical lissencephaly, is a disease of cortical folding in which the brain presents with a below-normal number of cortical folds, which appear broader in width (see Figures 6.9 and 6.10) [5, 65, 79]. As we did with polymicrogyria, we model various types of type I lissencephaly (henceforth referred to simply as lissencephaly) by varying the values of parameters $R$ and $\omega$ in our model systems. Results corresponding to our model representations of lissencephaly are summarized in Table 6.2 and Figures 6.11 and 6.12 for exponential and logistic growth. For example, Figures 6.11a–6.11c and 6.12a–6.12c (repeats of Figures 6.7a–6.7c and 6.8a–6.8c) show normal patterns for exponential and logistic growth, while figures 6.11d–6.11l and 6.12d–6.12l show various representations of lissencephaly. The corresponding full pattern evolution and labyrinthine visualization figures are in Appendix B.

**Microcephalic Lissencephaly: Norman-Roberts Syndrome.** Norman-Roberts Syndrome (NRS) is a very rare congenital disease of brain development, with only eleven cases reported as of 2007 [11, 65, 68, 79]. NRS patients present with type I lissencephaly, microcephaly (see Figure 6.9), reduced head growth rate, severe mental retardation, and epilepsy [5, 11, 65, 79]. In five of the eleven cases, patients presented with enlarged LVs, while in the other six cases the LVs are reported as not being enlarged (see Figure 6.10) [11, 65, 68, 79]. For NRS cases in which the LVs are not enlarged, individual components of the brain are smaller than normal (including the LVs), as NRS patients suffer from microcephaly. To model these cases of NRS, we select $\omega = 115$ and represent the smaller-than-normal-LVs by reducing the value of $R$ to $R = 0.005$, resulting in a smaller prolate spheroidal domain (representing the LV) as explained in Section 6.3. Decreasing $R$ results in a less complex final pattern, or in other words, a decrease in number and increase in width of stripes when compared to the normal pattern (see Figures 6.11d–6.11f and 6.12d–6.12f). By interpreting the striped pattern as a prepattern for the location and size of cortical folds via the IPM, this represents a decrease in number and increase in width of cortical folds, modeling the lissencephaly that is seen in NRS.

For cases of NRS in which the LVs are enlarged, the enlarged ventricles are still contained within a microcephalic brain, and the literature is again unclear about the size of such enlarged LVs relative to normal-sized LVs in a normocephalic brain. To model the enlarged LVs in these cases of NRS, we select $R = 0.015$ (corresponding to normal-sized LVs) as we did in the case of PMG with microcephaly and enlarged LVs in Section 6.3.1. The needed prepattern leading to lissencephaly can then be generated with $\omega = 30$, representing a decrease in the overall activator-inhibitor genetic expression. This again results in a pattern with a decrease in number and increase in width of stripes when compared to the normal pattern, representing the lissencephaly observed in NRS (see Figures 6.11g–6.11i and 6.12g–6.12i).

**Normocephalic Lissencephaly.** Type I lissencephaly can occur in normocephalic brains that possess enlarged LVs [39, 52]. We again model the enlargement of LVs by using $R = 0.021$, giving a larger domain size as explained in Section 6.3. The lissencephalic prepattern can then be generated on a large domain with $\omega = 30$, representing an overall decrease in genetic activator-inhibitor expression. The end result of using $R = 0.021, \omega = 30$ in Systems (4.23) and (5.5) is a pattern with stripes that are decreased in number and

Table 6.2: Lissencephaly simulation results. Simulation results are summarized in Figures 6.11 and 6.12. Full pattern evolution and labyrinthine visualization figures are in Appendix B.

| Growth Function | Figure Type | Normal ($R = 0.015$, $\omega = 115$) | NRS, LVs non-enlarged ($R = 0.005$, $\omega = 115$) | NRS, LVs enlarged ($R = 0.015$, $\omega = 30$) | Type I lissencephaly, normocephaly, enlarged LVs ($R = 0.021$, $\omega = 30$) |
|---|---|---|---|---|---|
| Exponential | Prolate spheroid prepattern | Figs. 6.11a, B.1 | Figs. 6.11d, B.10 | Figs. 6.11g, B.13 | Figs. 6.11j, B.16 |
| | Rectangular domain folding pattern | Figs. 6.11b, B.2 | Figs. 6.11e, B.11 | Figs. 6.11h, B.14 | Figs. 6.11k, B.17 |
| | Prolate spheroid folding pattern | Figs. 6.11c, B.3 | Figs. 6.11f, B.12 | Figs. 6.11i, B.15 | Figs. 6.11l, B.18 |
| Logistic | Prolate spheroid prepattern | Figs. 6.12a, B.19 | Figs. 6.12d, B.28 | Figs. 6.12g, B.31 | Figs. 6.12j, B.34 |
| | Rectangular domain folding pattern | Figs. 6.12b, B.20 | Figs. 6.12e, B.29 | Figs. 6.12h, B.32 | Figs. 6.12k, B.35 |
| | Prolate spheroid folding pattern | Figs. 6.12c, B.21 | Figs. 6.12f, B.30 | Figs. 6.12i, B.33 | Figs. 6.12l, B.36 |

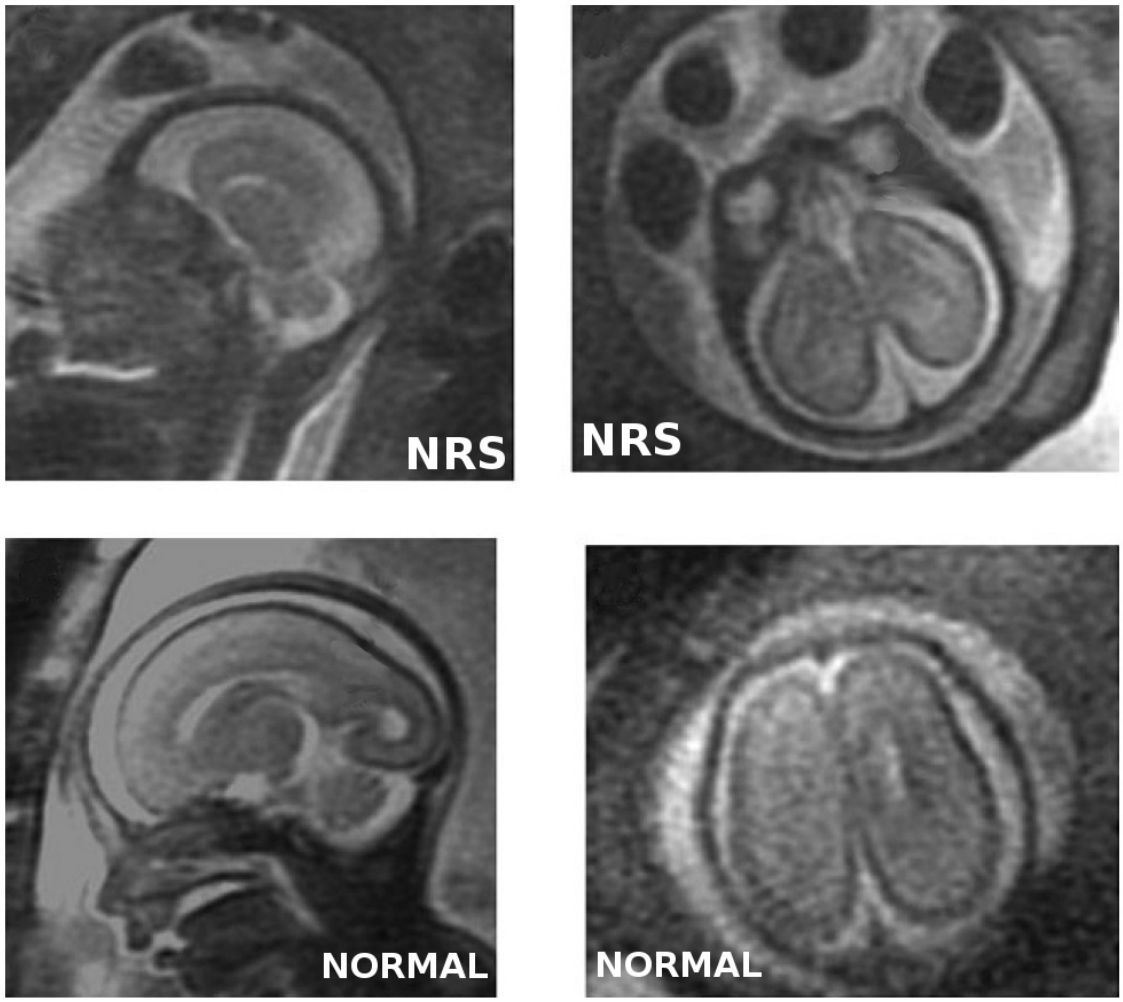


Figure 6.9: Comparison of Norman-Roberts Syndrome brain with normally developing brain (MRI). At 23 weeks GA, one can observe the microcephaly exhibited by a Norman-Roberts Syndrome fetus (top figures) as compared with a normally developing fetus (bottom figures). Furthermore, one can observe the presence of the parietooccipital sulcus in the normal brain (bottom left) but not in the NRS brain (top left), demonstrating the lissencephaly presented by NRS. Figure adapted from [65].

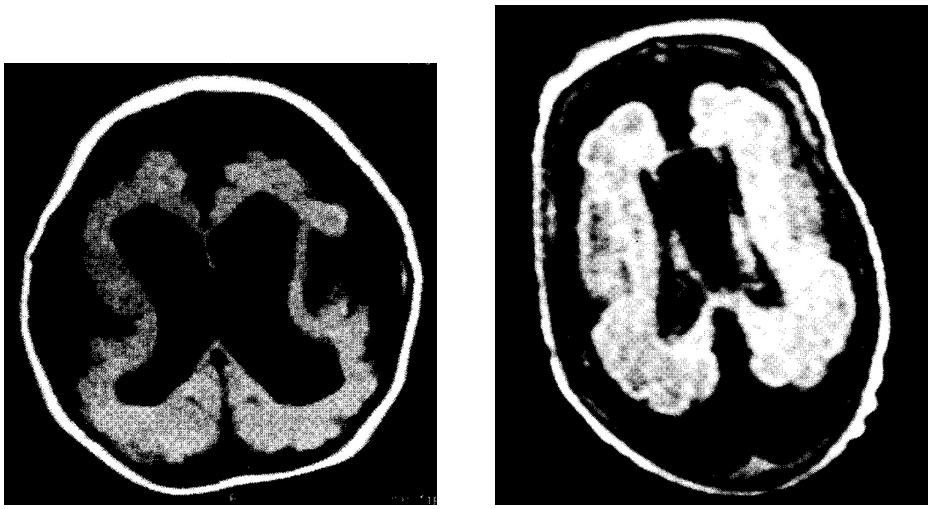

(a) NRS with enlarged LVs (b) NRS with LVs not enlarged

Figure 6.10: Lateral ventricles in Norman-Roberts Syndrome (MRI). Out of the eleven reported cases of NRS, five have presented with enlarged LVs (a) and six have presented with LVs that are not enlarged (b). Lissencephaly is observed in all cases. Figures adapted from [11].

increased in width when compared to the normal pattern (see Figures 6.11j–6.11l and 6.12j–6.12l), representing lissencephaly.

## 6.4 Exponential Versus Logistic Growth

We have presented two Turing system models of cortical folding, one on an exponentially growing domain and the other on a logistically growing domain, and have used them to model different diseases of cortical folding. The exponential and logistic growth models each have their own advantages and disadvantages. The exponentially growing model allows for the derivation of mathematical Turing conditions, which allow one to select system parameters such that the system is guaranteed to be able to generate Turing patterns. An exponentially growing domain may not be the most biologically realistic, as the domain keeps growing and the generated patten keeps evolving and increasing in complexity with increasing $t$, yet the developing brain does not keep growing forever and the cortical folding pattern is eventually finalized. In order to be interpreted as a prepattern for cortical folding, one must choose an arbitrary time at which the numerical simulation must be stopped. The pattern at this time then represents the prepattern for IPC self-amplification, which could be correlated with the cortical folding pattern according to the IPM.

The logistically growing model addresses the aforementioned shortcomings of the exponential model while possessing drawbacks of its own. The logistically growing model does not allow for the derivation of Turing conditions and as such cannot be guaranteed to be able to generate Turing patterns, but as we have demonstrated in Section 5.3, system

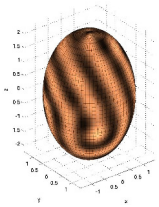

(a) Normal: $R = 0.015$, $\omega = 115$

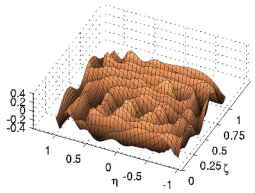

(b) Folding pattern from (a)

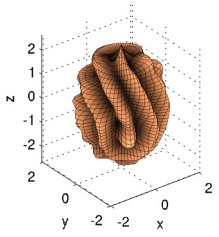

(c) Projection of (b)

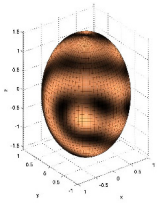

(d) NRS, non-enlarged LVs: $R = 0.005, \omega = 115$

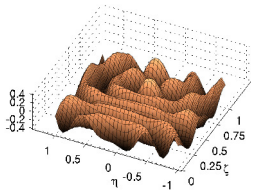

(e) Folding pattern from (d)

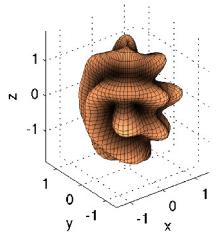

(f) Projection of (e)

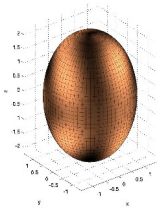

(g) NRS, enlarged LVs: $R = 0.015, \omega = 30$

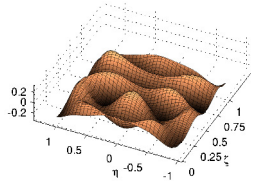

(h) Folding pattern from (g)

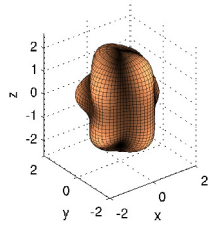

(i) Projection of (h)

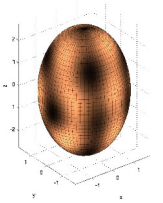

(j) Type I Lissencephaly, enlarged LVs, normocephaly: $R = 0.021, \omega = 30$

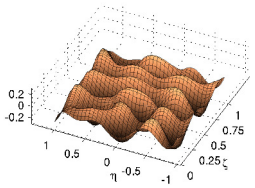

(k) Folding pattern from (j)

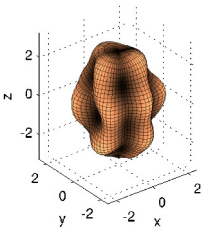

(l) Projection of (k)

Figure 6.11: Modeling lissencephaly on an exponentially growing prolate spheroid. The generated lissencephalic prepatterns exhibit a decreased number and increased width of stripes (figures (d)–(l)) relative to the normal patterns (figures (a)–(c)). The center and right columns show how a labyrinthine cortical folding pattern could develop from the corresponding Turing genetic chemical prepattern in the left column. See Figures B.1–B.3 and Figures B.10–B.18 for the corresponding pattern evolution and labyrinthine visualization figures.

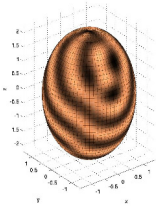

(a) Normal: $R = 0.015$, $\omega = 115$

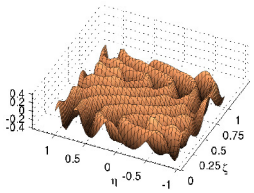

(b) Folding pattern from (a)

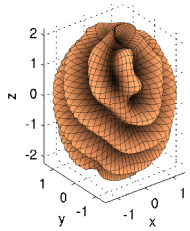

(c) Projection of (b)

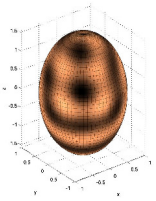

(d) NRS with non-enlarged LVs: $R = 0.005, \omega = 115$

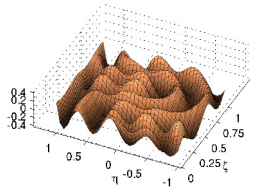

(e) Folding pattern from (d)

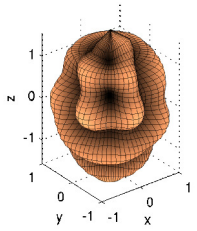

(f) Projection of (e)

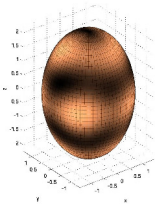

(g) NRS with enlarged LVs: $R = 0.015, \omega = 30$

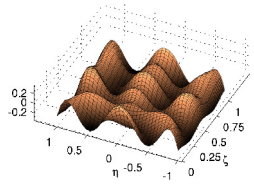

(h) Folding pattern from (g)

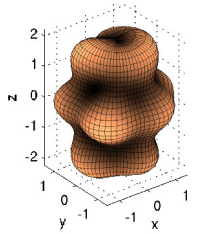

(i) Projection of (h)

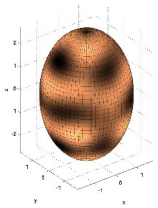

(j) Type I Lissencephaly with enlarged LVs and normocephaly: $R = 0.021, \omega = 30$

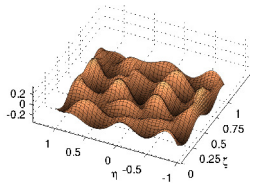

(k) Folding pattern from (j)

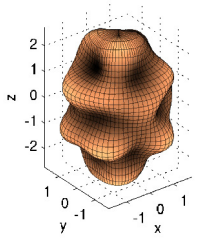

(l) Projection of (k)

Figure 6.12: Modeling lissencephaly on a logistically growing prolate spheroid. The generated lissencephalic prepatterns exhibit a decreased number and increased width of stripes (figures (d)–(l)) relative to the normal patterns (figures (a)–(c)). The center and right columns show how a labyrinthine cortical folding pattern could develop from the corresponding Turing genetic chemical prepattern in the left column. See Figures B.19–B.21 and Figures B.28–B.36 for the corresponding pattern evolution and labyrinthine visualization figures.

parameters can still be found so that Turing patterns can be generated. The logistically growing model makes up for its lack of mathematical Turing conditions with biological realism, as its domain eventually stops growing and its pattern eventually converges. Since the brain eventually stops growing and the cortical folding pattern is eventually finalized, a logistically growing domain Turing model of cortical folding is more biologically realistic than an exponentially growing domain model. Furthermore, since the pattern generated on a logistically growing domain converges to a final pattern, there is no need to select an artificial time at which to stop the model simulation to view the pattern. The system's final convergent pattern can be readily interpreted as the chemical prepattern for IPC self-amplification, which, as stated by the IPM, might be correlated with the cortical folding pattern.

Beyond the context of cortical folding models, a strength of the exponentially growing domain Turing system in System (4.2) is that it can be applied to not just an exponentially growing prolate spheroidal domain, but an exponentially growing domain in any of the eleven Helmholtz-separable coordinate systems. The linear stability analysis in Section 4.1 can be used to derive mathematical Turing conditions on any such exponentially growing domain. System (4.2) thus can be used to construct mathematical Turing models complete with Turing conditions on a geometrically diverse group of exponentially growing domains.

## 6.5 Conclusions

This chapter presented our growing prolate spheroidal domain Turing system models of cortical folding patterns. Motivation for using a Turing system in a biomathematical model of cortical folding was provided, and details of how the mathematics link to the biology of cortical folding (via the IPM) were discussed. Motivation for using an exponentially or logistically growing domain in a Turing model of cortical folding was presented. Both the exponential and logistic models were utilized to model various manifestations of polymicrogyria and lissencephaly, two contrasting types of cortical folding disease. Variations of these diseases were captured in the models by altering the values of $R$ and $\omega$. Changing $R$ allowed for control of domain size, which represented the size of the LVs; changing $\omega$ allowed for control of the reaction terms' strength relative to the diffusion and dilution terms, which represented the overall genetic expression level of the activator and inhibitor. Labyrinthine patterns were visualized on both the computational domains and on the prolate spheroidal domains. The fact that our models were able to qualitatively capture both polymicrogyric and lissencephalic diseases of cortical folding lends support to the IPM; in other words, our models help provide evidence that patterns of genetic chemical factors could play a role in establishing cortical folding patterns. Finally, strengths and weaknesses of the exponential growth model of cortical folding were compared with those of the logistic growth model.

Our cortical folding models investigate and lend support to the role of genetic chemical control of cortical folding by implementing a Turing system on a dynamically growing and biologically relevant prolate spheroidal domain. We specifically investigated the effects of altering domain growth (via changes in $R$) or genetic expression level (via changes in $\omega$) on the generated pattern; this allowed us to capture various types of polymicrogyria and lissencephaly with our models. The Striegel and Hurdal [86] static prolate spheroidal do-

main Turing model (see Section 2.3.1) investigated the role of domain size and shape as the primary factors influencing a genetically-controlled pattern for cortical folding. Their model was able to predict the order of cortical sulci, which is something our growing domain models are unable to do. However, our models were able to represent more diseases of cortical folding in a more biologically realistic way due to the inclusion of domain growth. Cartwright's [13] static domain Turing model (see Section 2.3.2) used the patterns generated by the reaction-diffusion system to represent axonal tension via axonal migration. Like Cartwright, we employ the value of activator $u$ to generate labyrinthine patterns. However, Cartwright employs a static rectangular domain, lacking the biological motivation and realism our models enjoy by employing a growing prolate spheroidal domain. The Lefevre and Mangin [47] Turing finite element model (see Section 2.3.3) generated a pattern that directly influenced the formation of cortical folds by causing the domain surface to deform up or down at every time step of the simulations. Our models, on the other hand, utilize a final Turing pattern as a prepattern that, according to the IPM, could be correlated with the possible location of cortical folds. The Toro and Burnod [93] 2-D tension-based finite element model (see Section 2.3.4) investigated the effects of having unequal domain growth in different parts of the domain, but only was able to represent cortical folds in two dimensions on a simple circular domain. The Geng *et al.* [29] 3-D tension-based finite element models (see Section 2.3.5), benefited from the use of fetal sheep MRI data to help construct and initialize the models; our models of human cortical folding could not be constructed on similar human data because such data is not readily available. However, their second model's growing 3-D rectangular domain was not as biologically inspired as our models' growing prolate spheroidal domain. Overall, our models fill a hole in the biomathematical cortical folding research by examining the effects of altering domain growth and overall genetic expression level in a Turing system that generates a genetic chemical prepattern for cortical folding.

# CHAPTER 7

# CONCLUSIONS

## 7.1 Summary

While there have been numerous biomathematical investigations into modeling cortical folding patterns of the brain, a growing domain Turing system model of cortical folding had yet to be implemented. Turing system models of cortical folding had been investigated using static domains [86], failing to capture the growth that inherently occurs as the brain develops. To address this hole in the research, this dissertation presented growing prolate spheroidal domain Turing system models of cortical folding using BVM kinetics and exponential or logistic domain growth.

We began by introducing the biology of cortical folding, discussing the relevant anatomical features and outlining some of the biological hypotheses attempting to describe the underlying mechanism of cortical folding. We noted that some biological hypotheses ascribe cortical folding development to a genetic chemically-controlled process, while others suggest a physical tension-driven process. After discussing several previous mathematical efforts into modeling cortical folding, we presented the properties of Turing reaction-diffusion systems and outlined a framework in which different types of domain growth could be incorporated into a Turing system on a prolate spheroidal surface. We then utilized numerical simulations to investigate the pattern-generating behavior of a Turing system with BVM kinetics on a prolate spheroidal domain under exponential or logistic domain growth. We observed that increasing system parameters $R$ or $\omega$ increased the complexity of the generated pattern at a given value of $t > 0$, and that patterns generated on domains with equal final domain size, regardless of the presence or type of growth function, are qualitatively similar in the number and size of stripes.

A growing domain Turing system can generate different patterns with different transient behaviors on the same geometric domain by changing the domain growth function. We have observed that a Turing system with BVM kinetics on an exponentially growing prolate spheroidal domain generates patterns that continually evolve. Changing the domain growth to logistic generates a pattern that evolves while the domain grows but then converges to a final pattern once domain growth stops. Overall, the presence of domain growth in a Turing system drives the Turing pattern to be transient, while a lack of domain growth allows the pattern to converge. This observation agrees with previous investigations into Turing systems on static prolate spheroids [86], exponentially growing spheres [32], and

linearly growing spheres [16]; it was further confirmed by observing the behavior of a Turing system on a piecewise exponentially growing prolate spheroidal domain. It is therefore of key importance to include domain growth when building a Turing model of cortical folding not only because of the biological realism that a growing domain lends to the model, but also because the addition of domain growth fundamentally alters the pattern-generating behavior of a Turing system.

To help investigate the plausibility of a genetic morphogen-controlled mechanism of cortical folding, we built the biological basis of our biomathematical models upon the Intermediate Progenitor Model (IPM), which is a biological hypothesis describing a possible underlying mechanism for cortical folding [45]. We utilized a prolate spheroidal domain to represent the LV and the prolate spheroidal domain surface to represent the SVZ, accurately capturing the shape of the LV during early neurogenesis. Under the IPM assumption that regional patterning of IPC self-amplification in the SVZ might be directly correlated to cortical folding patterns, our model systems' Turing patterns can serve as a genetic chemical factor prepattern for IPC self-amplification. IPCs in activated regions ($u > 0$) of the pattern would self-amplify, leading to gyri, while IPCs in nonactivated ($u < 0$) regions would not self-amplify, leading to sulci.

Patterns created by our exponentially or logistically growing domain Turing systems can qualitatively describe cortical folding patterns in normal cortical development or in certain diseases of cortical folding. By controlling the strength of the reaction terms relative to the diffusion and dilution terms (reflecting varying levels of expression of genetic factors controlling IPC cells) via parameter $\omega$ and by controlling the domain size (reflecting the size of the LVs) via parameter $R$, our models of cortical folding can qualitatively capture different manifestations of polymicrogyria and lissencephaly, two types of diseases of cortical folding in which there are respectively too many or too few cortical folds. The fact that our Turing system models of cortical folding are able to qualitatively capture such vastly different kinds of diseases of cortical folding lends support to both the role of genetic control in cortical development and to the IPM.

## 7.2 Future Directions

Patterns generated by our growing domain Turing models of cortical folding represent patterns of genetic chemical factors, and genetic control is the underlying principle of several modern biological hypotheses of cortical folding such as the Intermediate Progenitor Hypothesis, Intermediate Progenitor Model, and Radial Unit Hypothesis. However, our models do not capture any physical axonal tension, which is the main constituent of competing biological hypotheses of cortical folding such as the Axonal Tension Hypothesis. As there has been much evidence supporting both genetic- and tension-based biological hypotheses of cortical folding [22, 73, 77], the true mechanism behind cortical folding likely involves both physical tension and genetic chemical control. Thus, a possible future extension of the research presented in this dissertation would be the incorporation of terms representing physical axonal tension into the model Turing system equations.

Another possible future direction for Turing models of cortical folding would be to utilize a finite element mesh that could dynamically grow from an initial prolate spheroid

shape to the final $c$-shape of the LV. Furthermore, while we have specifically investigated an implementation of the growing domain Turing system framework in System (3.2) using BVM kinetics on a prolate spheroidal domain under isotropic exponential and logistic domain growth, it would be of further interest to investigate the types of patterns that System (3.2) could generate using other kinds of reaction kinetics, geometric domains (such as an oblate spheroid), or growth functions (such as linear, quadratic, or anisotropic growth). It is interesting to note that the three Turing models of cortical folding discussed in Section 2.3 all utilized different reaction kinetics, yet still generated results that could be applied to cortical folding. As mentioned in Section 6.4, the linear stability analysis performed in Section 4.1 could be used to obtain mathematical Turing conditions on any of the eleven Helmholtz-separable coordinate systems under exponential growth, opening up the possibility for using System (3.2) to model other areas of developmental biology beyond cortical folding patterns.

While this dissertation qualitatively described the number and size of stripes in growing domain BVM Turing patterns, future research would benefit from the development of a metric or index which quantifies the complexity of such patterns. Some of the ways that this could be accomplished could include measuring the length of stripes, calculating the number of stripes per unit area, or counting the number of "defects" (spots or discontinuous stripes) [97] in a striped pattern. The mechanism by which stripes form in a growing domain BVM Turing pattern could be explored, investigating if different growth rates or growth functions affect the way in which stripes emerge as the pattern evolves.

Several challenges face our growing domain Turing models of cortical folding. To begin, parameters used in our simulations are not based on real human cortical folding data, but rather were phenomenologically selected to produce the desired results. Longitudinal data about the surface area and volume of the LVs or the rate of growth of the SVZ would allow growth function parameters and initial domain size and shape parameters to be selected in a way that would allow our models' domain to more accurately represent the developing LVs and SVZ. Data about the diffusion coefficients and genetic expression levels of genetic factors controlling IPC self-amplification would allow the diffusion coefficient $D$, BVM kinetics parameters $a, b, C, h$, and domain scale parameter $\omega$ (controlling relative reaction term strength) to be selected in a way that would allow our models to more accurately represent the underlying biology of cortical development. However, such data is not readily available, and thus new biological research must be conducted to allow the mathematics to better represent and connect with the biology.

We modeled different diseased conditions of cortical folding by altering the values of $R$ and $\omega$. For example, some cases of NRS are reported as having enlarged LVs, and other cases of NRS are reported as not having enlarged LVs. In both cases, the cortex exhibits lissencephaly. Our model was able to capture both of these cases. A large $R$ (representing enlarged LVs) coupled with a small $\omega$ value (representing a decrease in genetic expression) modeled NRS lissencephaly with enlarged LVs, while a small $R$ (representing small LVs due to microcephaly) coupled with the "normal" value of $\omega$ modeled NRS lissencephaly with non-enlarged LVs. Clearly, many factors are at play in diseases of cortical folding, and more research is needed to establish a link between the mathematical parameters $R, \omega$ and the underlying biology of the disease.

Our models can represent cortical folding only on a qualitative level; that is, they can generally describe the number and size of cortical folds but are unable to model the location

of specific folds in the brain or the order in which specific folds appear. Part of the reason for this is the inherent sensitivity of Turing systems to initial conditions. This high level of sensitivity to initial conditions means that different initial conditions cause our model systems to generate different patterns that may be qualitatively similar in number and size of stripes, but vastly different in the arrangement of such stripes. We seeded our random initial conditions to allow us to investigate the effects of altering $R$ and $\omega$ on the patterns produced by our model systems. However, the initial conditions of Turing systems represent random biological noise, and these natural perturbations are truly random, not a seeded sequence of random numbers. Furthermore, humans develop cortical folding patterns in which certain folds share a common location and size despite originating from different initial conditions. Finding a way to generate consistently reproducible patterns (hence reducing the sensitivity to initial conditions) that can model the specific location and order of emergence of cortical folds is an area where Turing modeling of cortical folding can be extended in the future. One possible way to address these issues may be to construct a Turing system on a self-deforming surface constructed of finite elements. As discussed in Section 2.3.3, this technique has been previously applied on a dynamically self-deforming sphere and was able to consistently reproduce the location of one cortical fold from different random initial conditions [47]. Overall growth of the spherical domain was not incorporated into this model, however, and so creating a finite element Turing model of cortical folding on a dynamically growing and self-deforming domain holds strong potential for future research.

## 7.3 Concluding Remarks

By combining the mathematics of Turing systems [95] with the biological ideas of genetic chemical prepatterns [62, 63, 95] and the Intermediate Progenitor Model [45], we have created two growing prolate spheroidal domain Turing system models of cortical folding that are capable of qualitatively modeling normal and diseased cortical folding patterns. Mathematically, by investigating the effects of exponential and logistic domain growth in a Turing system, we have demonstrated that the presence of domain growth drives a prolate spheroidal Turing system pattern to become transient. Under exponential domain growth, patterns are continually transient; when utilizing logistic domain growth, patterns are transient during the growth period but converge to a final pattern once domain growth ceases. Both types of domain growth possess interesting applicability for mathematically modeling cortical folding patterns. Biologically, by creating a biomathematical model that is able to capture a variety of diseases of cortical folding, we have provided evidence to support the role of genetic chemical factor prepatterns in the development of cortical folding patterns, therefore supporting biological cortical folding hypotheses such as the Intermediate Progenitor Model.

# APPENDIX A

# APPENDIX: DERIVATIONS

## A.1 Generic Reaction Diffusion-Equation

To derive a generic reaction-diffusion equation in three-dimensional space, let $V \subset \mathbb{R}^3$ be a compact domain and let $S \subset \mathbb{R}^2$ be its piecewise-continuous surface. Let $u(\mathbf{X}, t)$ be the concentration of a substance in $V$ at location $\mathbf{X}$ and time $t$, and assume $u(\mathbf{X}, t)$ is continuous. The general theory of conservation states that the rate of change of the amount of the substance inside $V$ equals the amount of the substance flowing across $S$ out of $V$ [72] plus the amount of the substance produced by its source inside $V$. This can be stated mathematically as

$$\frac{d}{dt}\int_V u(\mathbf{X}, t)\, dV = -\int_S \mathbf{J} \cdot d\mathbf{S} + \int_V f(u(\mathbf{X}, t))\, dV, \tag{A.1}$$

where $f(u(\mathbf{X}, t))$ represents the source of the substance inside $V$ and $\mathbf{J}$ represents the flux of the substance across $S$.

**Theorem A.1.1** (Divergence Theorem [83]). *If $V$ is a bounded spatial domain with a piecewise continuous boundary surface $S$ with positive orientation, and $\mathbf{J}$ is any continuous vector field on the closure of $V$, then*

$$\int_V \nabla \cdot \mathbf{J}\, dV = \int_S \mathbf{J} \cdot d\mathbf{S}. \tag{A.2}$$

Using Equation (A.2), we can rewrite Equation (A.1) as

$$\frac{d}{dt}\int_V u(\mathbf{X}, t)\, dV \quad = \quad -\int_V \nabla \cdot \mathbf{J}\, dV + \int_V f(u(\mathbf{X}, t))\, dV,$$

which implies

$$\int_V \left[\frac{\partial u}{\partial t}(\mathbf{X}, t) + \nabla \cdot \mathbf{J} - f(u(\mathbf{X}, t))\right] dV = 0. \tag{A.3}$$

**Theorem A.1.2** (Second Vanishing Theorem [84]). *If $f(\mathbf{X})$ is a continuous function in $D$ such that $\int_{D'} f(\mathbf{X})\, dV = 0$ for all subdomains $D' \subset D$, then $f(\mathbf{X}) \equiv 0$ on $D$.*

Applying Theorem (A.1.2) to Equation (A.3) yields

$$\frac{\partial u}{\partial t} = -\nabla \cdot \mathbf{J} + f(u(\mathbf{X}, t)). \tag{A.4}$$

Fick's First Law states $\mathbf{J} = -D\nabla u$ [55], where $D > 0$ is the constant diffusion coefficient of the substance. Using Fick's First Law, Equation (A.4) can be rewritten as the generic reaction-diffusion equation

$$\frac{\partial u}{\partial t} = D\nabla^2 u + f(u(\mathbf{X}, t)),$$

where the source function $f$ is now referred to as a reaction kinetics function [63].

## A.2 Growing Domain Turing System Framework

The following derivation of the growing domain Turing system framework follows that of [72].

Let $S_t \subset \mathbb{R}^3$ be a two-dimensional growing surface such that $S_t = \psi_t(\Omega_i)$ (see Figure (A.1)), where

$$\psi_t : \Omega_i \subset \mathbb{R}^2 \to \mathbb{R}^3, \quad \psi_t(\zeta, \eta) \equiv \mathbf{X}(\zeta, \eta, t) = \begin{pmatrix} x(\zeta, \eta, t) \\ y(\zeta, \eta, t) \\ z(\zeta, \eta, t) \end{pmatrix}, \tag{A.5}$$

for $(\zeta, \eta) \in \Omega_i, t \geq 0$. Assume that growth function $\psi_t \in C^2$ is continuously differentiable with respect to $t$. Also assume that $S_t$ is a regular surface in the Euclidean metric, so that

$$\mathbf{X}_\zeta \times \mathbf{X}_\eta \neq \mathbf{0} \ \ \forall\, (\zeta, \eta) \in \Omega_i, \forall\, t \geq 0$$

and

$$dl^2 = dx^2 + dy^2 + dz^2.$$

Finally, assume that

$$\mathbf{X}_\zeta \cdot \mathbf{X}_\eta = 0 \quad \forall\, t,$$

which implies that the $(\zeta, \eta)$-parametrized coordinate system is orthogonal on $S_t$. It follows that the normal vector to $S_t$ is $\mathbf{N}(\zeta, \eta, t) = \mathbf{X}_\zeta \times \mathbf{X}_\eta \neq \mathbf{0}$.

Next, consider a specific parameter domain region $\Omega_0 \subset \Omega_i$ with smooth positively oriented boundary $\partial\Omega_0$. Define $\Omega(t) = \psi_t(\Omega_0) \in S_t$ with boundary $\partial\Omega(t) = \psi_t(\partial\Omega_0)$ to be the growing domain of interest (see Figure (A.1)), and suppose the boundary is parametrized by $\partial\Omega(t) = \mathbf{X}(\zeta_0(s), \eta_0(s))$, where $\mathbf{X} \in S_t$ and $s \in [0, 1]$. Let $\phi = \phi(\mathbf{X}(\zeta, \eta, t), t)$ be the concentration at location $\mathbf{X} \in S_t$ of a chemical substance with diffusion coefficient $D$. Ignoring the effects of any reaction kinetics sources of $\phi$ inside the domain $\Omega(t)$, then Equation (A.1) on $\Omega(t)$ becomes

$$\frac{d}{dt} \int_{\Omega(t)} \phi(\mathbf{X}, t)\, dS = D \int_{\partial\Omega(t)} \nabla\phi \cdot \hat{\mathbf{n}}\, dl, \tag{A.6}$$

where $\hat{\mathbf{n}}$ is the outward unit normal vector to $\partial\Omega(t)$ and we have again used Fick's First Law, $\mathbf{J} = -D\nabla\phi$.

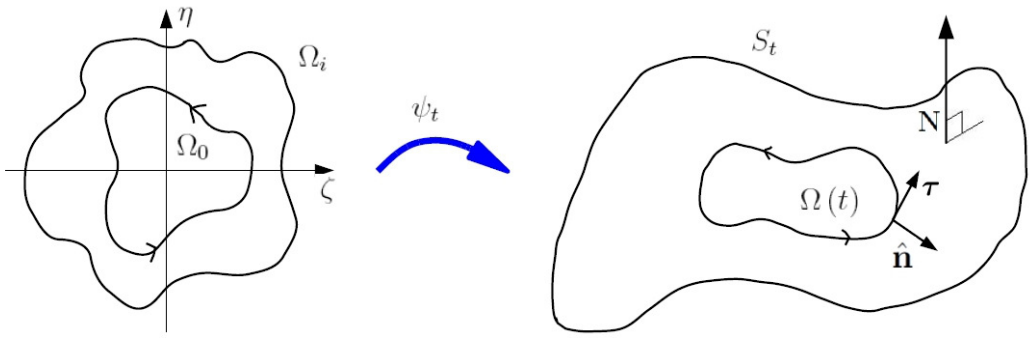


Figure A.1: Deriving the growing domain Turing system framework. The growth function $\psi(t)$ maps $\Omega_i$ to $S_t$ and $\Omega_0$ to $\Omega\,(t)$. The surface normal vector to $S_t$ is denoted $\mathbf{N}$. The tangent and unit normal vectors to $\partial\Omega(t)$ are denoted $\boldsymbol{\tau}$ and $\hat{\mathbf{n}}$, respectively.

Let $\boldsymbol{\tau}$ be the tangent vector to $\partial\Omega(t)$ so that $\boldsymbol{\tau}\cdot\hat{\mathbf{n}} = 0$ and let $(\cdot)'$ represent the derivative $\dfrac{d(\cdot)}{ds}$. Since $\partial\Omega(t) = \mathbf{X}(\zeta_0(s), \eta_0(s))$, it follows that

$$\begin{aligned}\boldsymbol{\tau} &= \frac{\partial \mathbf{X}}{\partial s} \\ &= \frac{\partial \mathbf{X}}{\partial \zeta_0}\frac{\partial \zeta_0}{\partial s} + \frac{\partial \mathbf{X}}{\partial \eta_0}\frac{\partial \eta_0}{\partial s} \\ &= \zeta_0'\mathbf{X}_\zeta + \eta_0'\mathbf{X}_\eta,\end{aligned}$$

where we have dropped the naught subscripts on derivatives of $\mathbf{X}$ for notational convenience.

To find $\hat{\mathbf{n}}$, we let $h_1, h_2$ be scale factors, where

$$h_1 = |\mathbf{X}_\zeta|\,, \quad h_2 = |\mathbf{X}_\eta|\,.$$

Let $\tilde{\mathbf{n}}$ be a normal vector to $\partial\Omega(t)$ whose length is not necessarily equal to 1. By the right-hand rule, $\tilde{\mathbf{n}} = \boldsymbol{\tau}\times\mathbf{N}$, which implies

$$\begin{aligned}\tilde{\mathbf{n}} &= \left(\zeta_0'\mathbf{X}_\zeta + \eta_0'\mathbf{X}_\eta\right)\times\left(\mathbf{X}_\zeta\times\mathbf{X}_\eta\right) \\ &= \zeta_0'\mathbf{X}_\zeta\times\left(\mathbf{X}_\zeta\times\mathbf{X}_\eta\right) + \eta_0'\mathbf{X}_\eta\times\left(\mathbf{X}_\zeta\times\mathbf{X}_\eta\right). \qquad \text{(A.7)}\end{aligned}$$

Applying the vector triple product $\mathbf{a}\times(\mathbf{b}\times\mathbf{c}) = \mathbf{b}(\mathbf{a}\cdot\mathbf{c}) - \mathbf{c}(\mathbf{a}\cdot\mathbf{b})$ to Equation (A.7) gives

$$\begin{aligned}\tilde{\mathbf{n}} &= \mathbf{X}_\zeta\left(\zeta_0'\mathbf{X}_\zeta\cdot\mathbf{X}_\eta\right) - \mathbf{X}_\eta\left(\zeta_0'\mathbf{X}_\zeta\cdot\mathbf{X}_\zeta\right) + \mathbf{X}_\zeta\left(\eta_0'\mathbf{X}_\eta\cdot\mathbf{X}_\eta\right) - \mathbf{X}_\eta\left(\eta_0'\mathbf{X}_\eta\cdot\mathbf{X}_\zeta\right) \\ &= -\zeta_0' h_1^2\mathbf{X}_\eta + \eta_0' h_2^2\mathbf{X}_\zeta\end{aligned}$$

since $\mathbf{X}_\zeta\cdot\mathbf{X}_\eta = 0$. Since

$$|\tilde{\mathbf{n}}|^2 = h_1^2 h_2^2\left(\zeta_0'^2 h_1^2 + \eta_0'^2 h_2^2\right) = h_1^2 h_2^2\,|\boldsymbol{\tau}|^2\,,$$

it follows that

$$\hat{\mathbf{n}} = \frac{\tilde{\mathbf{n}}}{|\tilde{\mathbf{n}}|} = \beta\mathbf{X}_\zeta + \alpha\mathbf{X}_\eta,$$

where

$$\alpha = -\frac{h_1}{h_2}\frac{\zeta_0'}{|\boldsymbol{\tau}|} \quad \text{and} \quad \beta = \frac{h_2}{h_1}\frac{\eta_0'}{|\boldsymbol{\tau}|}.$$

To continue the derivation of the growing domain Turing system framework, we need to rewrite both the right- and left-hand sides of Equation (A.6). We first turn our attention to the right-hand side. A change of variables yields

$$\begin{aligned} D\int_{\partial\Omega(t)} \nabla\phi\cdot\hat{\mathbf{n}}\,dl &= D\oint_{\partial\Omega_0} \nabla\phi\cdot(\alpha\mathbf{X}_\eta+\beta\mathbf{X}_\zeta)\,|\boldsymbol{\tau}|\,ds \\ &= D\oint_{\partial\Omega_0}\left(-\frac{h_1}{h_2}\partial_\eta\phi\right)d\zeta+\left(\frac{h_2}{h_1}\partial_\zeta\phi\right)d\eta. \end{aligned} \tag{A.8}$$

**Theorem A.2.1** (Green's Theorem [84])**.** *Suppose $D\subset\mathbb{R}^2$ is a bounded domain with positively oriented and piecewise-$C^1$ boundary $C$. If $p(x,y), q(x,y)\in C^1$ on the closure of $D$, then*

$$\int_D\left(\frac{\partial q}{\partial x}-\frac{\partial p}{\partial y}\right)dx\,dy = \oint_C p\,dx+q\,dy.$$

Green's Theorem applied to Equation (A.8) implies

$$D\int_{\partial\Omega(t)}\nabla\phi\cdot\hat{\mathbf{n}}\,dl = D\int_{\Omega_0}\left[\left(\frac{h_2}{h_1}\partial_\zeta\phi\right)_\zeta+\left(\frac{h_1}{h_2}\partial_\eta\phi\right)_\eta\right]d\zeta\,d\eta. \tag{A.9}$$

Next, applying a change of variables to the left-hand side of Equation (A.6) gives

$$\begin{aligned} \frac{d}{dt}\int_{\Omega(t)}\phi(\mathbf{X},t)\,dS &= \frac{d}{dt}\int_{\Omega_0}\phi(\mathbf{X}(\zeta,\eta,t),t)h_1h_2\,d\zeta\,d\eta \\ &= \int_{\Omega_0}\frac{\partial}{\partial t}[\phi(\mathbf{X}(\zeta,\eta,t),t)h_1h_2]\,d\zeta\,d\eta \\ &= \int_{\Omega_0}\left[h_1h_2\left(\frac{\partial}{\partial t}\phi(\mathbf{X},t)\right)+(h_1h_2)_t\,\phi(\mathbf{X},t)\right]d\zeta\,d\eta. \end{aligned} \tag{A.10}$$

By the parametrization given in Equation (A.5), $\phi(\mathbf{X}(\zeta,\eta,t),t)=\phi(x,y,z,t)$. Applying the chain rule gives

$$\begin{aligned} \frac{\partial}{\partial t}\phi(\mathbf{X}(\zeta,\eta,t),t) &= \frac{\partial}{\partial t}\phi(x,y,z,t) \\ &= \frac{\partial\phi}{\partial x}\frac{\partial x}{\partial t}+\frac{\partial\phi}{\partial y}\frac{\partial y}{\partial t}+\frac{\partial\phi}{\partial z}\frac{\partial z}{\partial t}+\frac{\partial\phi}{\partial t}\frac{dt}{dt} \\ &= \nabla\phi\cdot\mathbf{X}_t+\frac{\partial\phi}{\partial t}. \end{aligned} \tag{A.11}$$

Substituting Equation (A.11) into Equation (A.10) gives

$$\frac{d}{dt}\int_{\Omega(t)}\phi(\mathbf{X},t)\,dS = \int_{\Omega_0}((\phi_t+\nabla\phi\cdot\mathbf{X}_t)h_1h_2+(h_1h_2)_t\,\phi)\,d\zeta\,d\eta. \tag{A.12}$$

Finally, substituting the rewritten the left- and right-hand sides of Equation (A.6) (given by Equations (A.12) and (A.9), respectively) into Equation (A.6) yields

$$\int_{\Omega_0} \left( \tilde{\phi}_t h_1 h_2 + (h_1 h_2)_t \, \tilde{\phi} - D \left[ \left( \frac{h_2}{h_1} \tilde{\phi}_\zeta \right)_\zeta + \left( \frac{h_1}{h_2} \tilde{\phi}_\eta \right)_\eta \right] \right) d\zeta \, d\eta = 0,$$

where we have used the notation $\tilde{\phi}(\zeta, \eta, t) = \phi(\mathbf{X}(\zeta, \eta, t), t)$ so that $\tilde{\phi}_t = \nabla \phi \cdot \mathbf{X}_t + \frac{\partial \phi}{\partial t}$, $\partial_\zeta \phi = \tilde{\phi}_\zeta$, and $\partial_\eta \phi = \tilde{\phi}_\eta$. Since $\Omega_0$ was arbitrary, we can apply Theorem (A.1.2) to yield

$$\tilde{\phi}_t h_1 h_2 + (h_1 h_2)_t \, \tilde{\phi} - D \left[ \left( \frac{h_2}{h_1} \tilde{\phi}_\zeta \right)_\zeta + \left( \frac{h_1}{h_2} \tilde{\phi}_\eta \right)_\eta \right] = 0,$$

which implies

$$\tilde{\phi}_t = \frac{1}{h_1 h_2} D \left[ \left( \frac{h_2}{h_1} \tilde{\phi}_\zeta \right)_\zeta + \left( \frac{h_1}{h_2} \tilde{\phi}_\eta \right)_\eta \right] - \frac{1}{h_1 h_2} (h_1 h_2)_t \, \tilde{\phi}. \tag{A.13}$$

Equation (A.13) can be equivalently written as

$$\tilde{\phi}_t = D \Delta_s \tilde{\phi} - \tilde{\phi} \partial_t (\ln(h_1 h_2)), \tag{A.14}$$

where $\Delta_s$ is the Laplace-Beltrami operator defined by

$$\Delta_s \tilde{\phi} = \frac{1}{h_1 h_2} \left[ \left( \frac{h_2}{h_1} \tilde{\phi}_\zeta \right)_\zeta + \left( \frac{h_1}{h_2} \tilde{\phi}_\eta \right)_\eta \right].$$

Using Equation (A.14), the dimensional form of the growing domain Turing system framework on growing domain $\Omega(t)$ for a system of two chemicals with concentrations $u = u(\zeta, \eta, t)$ and $v = v(\zeta, \eta, t)$ for $(\zeta, \eta) \in \Omega_0$ is

$$\left.\begin{aligned} u_t &= D_u \Delta_s u - \partial_t (\ln(h_1 h_2)) u + F(u, v), \\ v_t &= D_v \Delta_s v - \partial_t (\ln(h_1 h_2)) v + G(u, v), \end{aligned}\right\} \tag{A.15}$$

where $F, G$ are the dimensional reaction kinetics and $D_u, D_v$ are the diffusion coefficients of $u, v$ respectively. System (A.15) can be nondimensionalized following the technique of Murray [63] to yield the nondimensional form of the growing domain Turing system framework,

$$\left.\begin{aligned} u_t &= D \Delta_s u - \partial_t (\ln(h_1 h_2)) u + \omega f(u, v), \\ v_t &= \Delta_s v - \partial_t (\ln(h_1 h_2)) v + \omega g(u, v), \end{aligned}\right\}$$

where $D = \dfrac{D_u}{D_v}$, $\omega > 0$ is the domain scale parameter, and $f, g$ are the dimensionless versions of $F, G$. See Sections A.3 and A.4 for details.

## A.3 BVM Kinetics

This derivation of BVM kinetics follows that of Leppanen [48, 49]. Consider the classic dimensional Turing system

$$\left.\begin{aligned} U_t &= D_U\nabla^2 U + f(U,V), \\ V_t &= D_V\nabla^2 V + g(U,V), \end{aligned}\right\} \tag{A.16}$$

where $f, g$ are the BVM kinetics (to be constructed below), $U = U(x,t), V = V(x,t)$ (where $x$ is space and $t$ is time) are the respective concentrations of activator morphogen $U$ and inhibitor morphogen $V$, and $D_U, D_V$ are the respective diffusion coefficients of $U, V$. Assume System (A.16) has a spatially uniform steady state at $(U_c, V_c)$ which remains a steady state in the absence of diffusion; that is, $f(U_c, V_c) = g(U_c, V_c) = 0$.

A Taylor expansion of the kinetics functions $f, g$ about the steady state $(U_c, V_c)$ is performed up to third order terms, giving

$$\begin{aligned} f(U,V) \approx\ & f(U_c,V_c) + (U-U_c)f_U|_{(U_c,V_c)} + (V-V_c)f_V|_{(U_c,V_c)} \\ &+ \frac{1}{2!}\left[(U-U_c)^2 f_{UU}|_{(U_c,V_c)} + 2(U-U_c)(V-V_c)f_{UV}|_{(U_c,V_c)} + (V-V_c)^2 f_{VV}|_{(U_c,V_c)}\right] \\ &+ \frac{1}{3!}\left[(U-U_c)^3 f_{UUU}|_{(U_c,V_c)} + 3(U-U_c)^2(V-V_c)f_{UUV}|_{(U_c,V_c)}\right. \\ &\qquad \left. + 3(U-U_c)(V-V_c)^2 f_{UVV}|_{(U_c,V_c)} + (V-V_c)^3 f_{VVV}|_{(U_c,V_c)}\right] + O(\epsilon^4) \end{aligned}$$

and similarly for $g(U,V)$. By construction, functions $f, g$ are defined to have the following partial derivatives, where all are evaluated at steady state $(U_c, V_c)$:

$$\begin{aligned} f_U &= A, \quad f_V = B, \quad f_{UV} = -C, \quad \frac{1}{2}f_{UVV} = -D_1, \\ f_{UU} &= f_{VV} = f_{UUU} = f_{UUV} = f_{VVV} = 0, \\ g_U &= E, \quad g_V = F, \quad g_{UV} = C, \quad \frac{1}{2}g_{UVV} = D_1, \quad \text{and} \\ g_{UU} &= g_{VV} = g_{UUU} = g_{UUV} = g_{VVV} = 0. \end{aligned}$$

The third order Taylor expansions of $f$ and $g$ then reduce to

$$\begin{aligned} f(U,V) = A(U-U_c) + B(V-V_c) \\ - C(U-U_c)(V-V_c) - D_1(U-U_c)(V-V_c)^2, \\ g(U,V) = E(U-U_c) + F(V-V_c) \\ + C(U-U_c)(V-V_c) + D_1(U-U_c)(V-V_c)^2. \end{aligned} \tag{A.17}$$

The quadratic $UV$ and cubic $UV^2$ kinetic terms give the BVM System (A.16) its characteristic behavior of generating spotted or striped patterns [9]. Generally, spotted patterns are produced when the quadratic term has a nonzero coefficient, while stripes are produced when the cubic term has a nonzero coefficient and the quadratic term's coefficient is zero or very close to zero [9, 21]. In other words, the quadratic term causes the system to strongly tend toward the formation of spots while the cubic term causes the system to tend toward the formation of stripes [9, 21].

We next establish the traditional dimensional BVM parameter notation by denoting

$$A = \alpha > 0, \quad B = 1, \quad C = r_2, \quad D_1 = \alpha r_1, \quad E = \gamma, \quad \text{and} \quad F = \beta.$$

Using this new parameter notation and the substitutions $u = U - U_C$ and $v = V - V_c$ (effectively moving the steady state of the system from $(U_c, V_c)$ to $(0,0)$) in the right hand side of Equations (A.17) yields the dimensional BVM kinetics

$$\begin{array}{rcl} f(u,v) & = & \alpha u(1 - r_1 v^2) + v(1 - r_2 u) \\ g(u,v) & = & v(\beta + \alpha r_1 uv) + u(\gamma + r_2 v). \end{array} \tag{A.18}$$

Substituting Equations (A.18) into System (A.16) yields

$$\left.\begin{array}{rcl} u_t & = & D\delta\nabla^2 u + \alpha u(1 - r_1 v^2) + v(1 - r_2 u), \\ v_t & = & \delta\nabla^2 v + v(\beta + \alpha r_1 uv) + u(\gamma + r_2 v), \end{array}\right\} \tag{A.19}$$

where $D = D_U/D_V$. A scaling factor $\delta > 0$ has been divided out of the diffusion coefficients to allow for independent control of diffusion and domain scaling. This scaling factor $\delta$ is inversely proportional to domain scale [85], unlike the directly proportional scaling factor commonly used in the Turing system notation of Murray [63]. Notice that the strength of cubic and quadratic interactions are respectively controlled by the parameters $r_1$ and $r_2$.

System (A.19) shall be referred to as the dimensional BVM system [9]. One should note that even though Equations (A.18) and System (A.19) are called "dimensional", their equations are actually dimensionless; BVM kinetics are phenomenological and hence are not based on any particular physical dimensions [56]. As stated by Maini [56], "Since the [BVM] model is therefore really a model of a model it probably does not make sense to talk about dimensional aspects of it."

To nondimensionalize System (A.19), let $T$ be the characteristic time and $L$ be the characteristic length of the system. Whereas we previously let $U = U(x,t), V = V(x,t)$ be the respective concentration functions for the activator and inhibitor, we now let $U$ and $V$ represent the characteristic concentrations of activator and inhibitor, respectively. We can then define the dimensionless quantities

$$\bar{u} = \frac{u}{U}, \quad \bar{v} = \frac{v}{V}, \quad \bar{t} = \frac{t}{T}, \quad \text{and} \quad \bar{x} = \frac{x}{L}. \tag{A.20}$$

Substituting these dimensionless quantities into System (A.19) gives

$$\left.\begin{array}{rcl} \dfrac{\partial\,(U\bar{u})}{\partial\,(T\bar{t})} & = & \dfrac{D\delta}{L^2}\nabla^2(U\bar{u}) + \alpha U\bar{u} - \alpha r_1 U\bar{u}(V\bar{v})^2 + V\bar{v} - r_2 U\bar{u}V\bar{v}, \\ \dfrac{\partial\,(V\bar{v})}{\partial\,(T\bar{t})} & = & \dfrac{\delta}{L^2}\nabla^2(V\bar{v}) + \beta V\bar{v} + \alpha r_1 U\bar{u}(V\bar{v})^2 + \gamma U\bar{u} + r_2 U\bar{u}V\bar{v}. \end{array}\right\} \tag{A.21}$$

To rewrite the nondimensional system in its final form, we define

$$T = \frac{L^2}{\delta}, \quad U = V = \frac{1}{\sqrt{r_1}}, \quad a = \frac{1}{\alpha}, \quad b = \frac{\beta}{\alpha}, \quad h = \frac{\gamma}{\alpha}, \quad C = \frac{r_2}{\alpha\sqrt{r_1}}, \quad \text{and} \quad \omega = \frac{L^2\alpha}{\delta},$$

which can be substituted into System (A.21) to yield the nondimensional BVM system,

$$\left.\begin{aligned} \tfrac{\partial u}{\partial t} &= D\nabla^2 u + \omega(u + av - Cuv - uv^2), \\ \tfrac{\partial v}{\partial t} &= \nabla^2 v + \omega(bv + hu + Cuv + uv^2), \end{aligned}\right\}$$

where the bars have been dropped for convenience. The domain scaling is now controlled by the parameter $\omega > 0$, which is directly proportional to the domain scale.

## A.4 Growing Domain BVM Turing System Nondimensionalization

Consider the dimensional growing domain Turing System (A.15) with dimensional BVM kinetics

$$\left.\begin{aligned} u_t &= D\delta\Delta_s u - \partial_t(\ln(h_1h_2))u + \alpha u(1 - r_1v^2) + v(1 - r_2u), \\ v_t &= \delta\Delta_s v - \partial_t(\ln(h_1h_2))v + v(\beta + \alpha r_1uv) + u(\gamma + r_2v). \end{aligned}\right\} \tag{A.22}$$

The process of nondimensionalizing System (A.22) is the same as that of System (A.19) in Section A.3 with the addition of nondimensionalizing the dilution terms $-\partial_t(\ln(h_1h_2))u$ and $-\partial_t(\ln(h_1h_2))v$. Substituting the dimensionless quantities (A.20) gives the new dimensionless dilution terms

$$-\frac{\partial}{\partial(T\bar{t})}(\ln(h_1h_2))U\bar{u} \quad \text{and} \quad -\frac{\partial}{\partial(T\bar{t})}(\ln(h_1h_2))V\bar{v}.$$

After simplifying and dropping the bars for convenience, the resulting nondimensional growing domain BVM Turing system is

$$\left.\begin{aligned} u_t &= D\Delta_s u - \partial_t(\ln(h_1h_2))u + \omega(u + av - Cuv - uv^2), \\ v_t &= \Delta_s v - \partial_t(\ln(h_1h_2))v + \omega(bv + hu + Cuv + uv^2). \end{aligned}\right\}$$

## A.5 Prolate Spheroidal Coordinates

The following derivation of prolate spheroidal coordinates follows that of [25, 85].

Consider an ellipse centered at the origin of the $(x, y)$ plane with major axis length $2a$, minor axis length $2b$, and foci at $(\pm c, 0)$. The ellipse has equation

$$\frac{x^2}{a^2} + \frac{y^2}{b^2} = 1, \tag{A.23}$$

where $a > b > 0$ and $c^2 = a^2 - b^2$; the interfocal distance $f$ is defined as $f = 2c$. To derive elliptical coordinates, let $a = \frac{f}{2}\cosh\mu$ and $b = \frac{f}{2}\sinh\mu$, where $\mu > 0$. Equation (A.23) then becomes

$$\frac{4x^2}{f^2\cosh^2\mu} + \frac{4y^2}{f^2\sinh^2\mu} = 1. \tag{A.24}$$

Setting Equation (A.24) equal to corresponding terms in the Pythagorean Identity $\cos^2\theta + \sin^2\theta = 1$ and rearranging yields the elliptical coordinate system $(\mu, \theta)$, where

$$\left.\begin{aligned} x &= \frac{f}{2}\cosh\mu\cos\theta, \\ y &= \frac{f}{2}\sinh\mu\sin\theta, \end{aligned}\right\} \tag{A.25}$$

and $\theta \in [0,\, 2\pi)$.

To derive prolate spheroidal coordinates, one must first rewrite the elliptical coordinate equations of System (A.25). To this end, define $\xi = \cosh\mu \geq 1$ and $\eta = \cos\theta \in [-1,\, 1]$. By relabeling the $x$ variable as $z$ [102] and using the definitions of $\xi$ and $\eta$, System (A.25) can be rewritten in an alternate form of elliptical coordinates,

$$\left.\begin{aligned} y &= \frac{f}{2}\sqrt{(1-\eta^2)(\xi^2-1)}, \\ z &= \frac{f}{2}\eta\xi. \end{aligned}\right\} \tag{A.26}$$

A prolate spheroid is generated by rotating an ellipse around its major axis; rotation around the minor axis yields an oblate spheroid, which will not be considered here [25]. Rotating an ellipse described by System (A.26) an angle $\phi \in [0, 2\pi)$ in the $(x, y)$ plane [102] yields the prolate spheroidal coordinate system [25],

$$\left.\begin{aligned} x &= \frac{f}{2}\sqrt{(1-\eta^2)(\xi^2-1)}\cos\phi, \\ y &= \frac{f}{2}\sqrt{(1-\eta^2)(\xi^2-1)}\sin\phi, \\ z &= \frac{f}{2}\eta\xi, \end{aligned}\right\} \tag{A.27}$$

where $\theta$ (represented by $\eta$) is the polar angle and $\phi$ is the azimuthal angle. As shown in Section 3.3, the azimuthal angle $\phi$ can be replaced by $\phi = 2\pi\zeta$, where $\zeta \in [0, 1)$, to facilitate implementation of System (A.27) in numerical schemes. Prolate spheroidal coordinates are an orthogonal coordinate system [25].

The south pole of a prolate spheroid is given by $\eta = -1 = \cos\pi$, while the north pole is given by $\eta = 1 = \cos 0 = \cos 2\pi$ (see Figure A.2). To avoid the ambiguity of multiple $\theta$-values corresponding to the same $\eta$-coordinate, $\theta$ is restricted to $\theta \in [0, \pi]$. When $\xi > 1$, constant $\xi$ values give concentric prolate spheroids centered at the origin, while constant $|\eta| < 1$ values give halves of hyperboloids of two sheets about the $z$-axis [25]. The cases when $\xi = 1$ and $|\eta| = 1$ are degenerate cases corresponding to the $z$-axis with $|z| \leq \frac{f}{2}$ and $|z| > \frac{f}{2}$, respectively [25].

The eccentricity of a prolate spheroid equals the eccentricity of the ellipse from which it was formed. The eccentricity $E$ of an ellipse with semimajor axis length $a$ and semiminor axis length $b$ is defined as [101]

$$E = \sqrt{1 - \frac{b^2}{a^2}}. \tag{A.28}$$

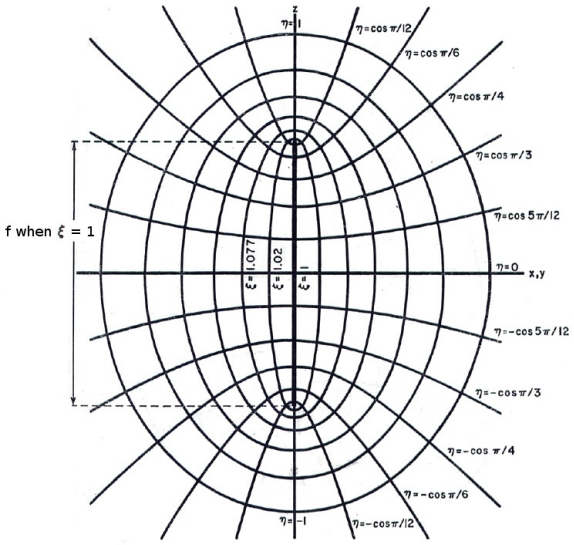


Figure A.2: Prolate spheroidal coordinates. Interfocal distance $f$ and radial term $\xi > 1$ respectively control the size and shape of a prolate spheroid, while $\zeta = \frac{\phi}{2\pi} \in [0, 1)$ and $\eta = \cos\theta \in [-1, 1]$ describe the azimuthal and polar angles $\phi$ and $\theta$, respectively. Figure adapted from [25].

Using $c^2 = a^2 - b^2$ and $f = 2c$, Equation (A.28) can be rewritten as

$$E = \frac{f}{2a}. \tag{A.29}$$

Recalling that $a = \frac{f}{2}\cosh\mu = \frac{f}{2}\xi$, it follows from Equation (A.29) that

$$E = \frac{1}{\xi}.$$

As discussed in Section 3.3, altering the value of $\xi$ allows one to control the eccentricity and therefore the shape of a prolate spheroid.

# APPENDIX B

# APPENDIX: FIGURES

In Chapter 6, the final ($t = 35$) Turing pattern and labyrinthine visualization figures were organized by disease. In this Appendix, we present the full pattern evolution and labyrinthine visualization figures and organize them by domain growth. Section B.1 contains exponential growth figures, while Section B.2 contains logistic growth figures. Animations are also available.

## B.1 Exponentially Growing Model

This section contains the full pattern evolution and labyrinthine visualization figures for the exponentially growing patterns presented in Chapter 6. Correspondence between the figures and the diseases they represent is given in Table B.1.

Table B.1: Exponential domain growth simulation results. Simulation results for polymicrogyria and lissencephaly are discussed in detail in Chapter 6.

(a) Polymicrogyria

| Growth Function | Figure Type | Normal ($R = 0.015$, $\omega = 115$) | PMG, enlarged LVs ($R = 0.021$, $\omega = 115$) | PMG, microcephaly, enlarged LVs ($R = 0.015$, $\omega = 150$) |
|---|---|---|---|---|
| Exponential | Prolate spheroid prepattern | Figs. 6.7a, B.1 | Figs. 6.7d, B.4 | Figs. 6.7g, B.7 |
| | Rectangular domain folding pattern | Figs. 6.7b, B.2 | Figs. 6.7e, B.5 | Figs. 6.7h, B.8 |
| | Prolate spheroid folding pattern | Figs. 6.7c, B.3 | Figs. 6.7f, B.6 | Figs. 6.7i, B.9 |

(b) Lissencephaly

| Growth Function | Figure Type | Normal ($R = 0.015$, $\omega = 115$) | NRS, LVs non-enlarged ($R = 0.005$, $\omega = 115$) | NRS, LVs enlarged ($R = 0.015$, $\omega = 30$) | Type I lissencephaly, normocephaly, enlarged LVs ($R = 0.021$, $\omega = 30$) |
|---|---|---|---|---|---|
| Exponential | Prolate spheroid prepattern | Figs. 6.11a, B.1 | Figs. 6.11d, B.10 | Figs. 6.11g, B.13 | Figs. 6.11j, B.16 |
| | Rectangular domain folding pattern | Figs. 6.11b, B.2 | Figs. 6.11e, B.11 | Figs. 6.11h, B.14 | Figs. 6.11k, B.17 |
| | Prolate spheroid folding pattern | Figs. 6.11c, B.3 | Figs. 6.11f, B.12 | Figs. 6.11i, B.15 | Figs. 6.11l, B.18 |

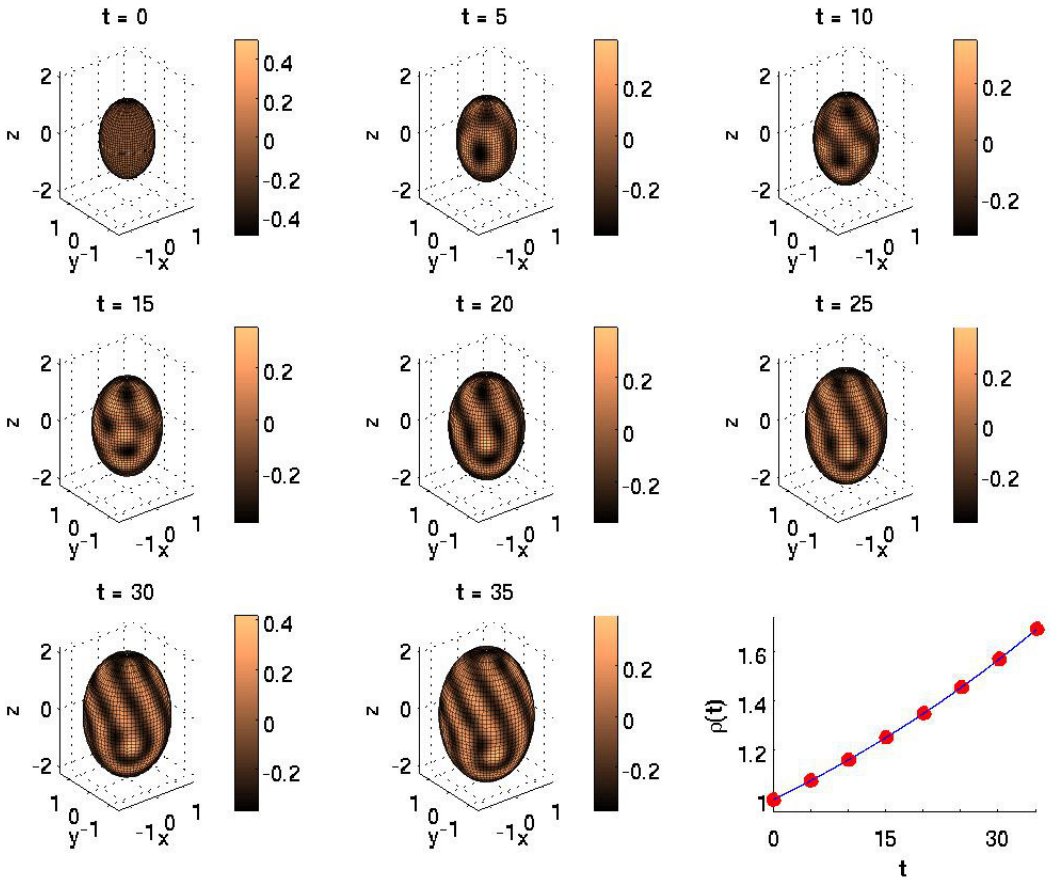


Figure B.1: Evolution of Turing pattern on an exponentially growing prolate spheroid representing normal cortical development. The pattern was generated by System (4.23) with $R = 0.015, \omega = 115$ and kinetics parameters listed on page 34. Red dots on the bottom right figure represent times at which the snapshots were taken. See also: animation.

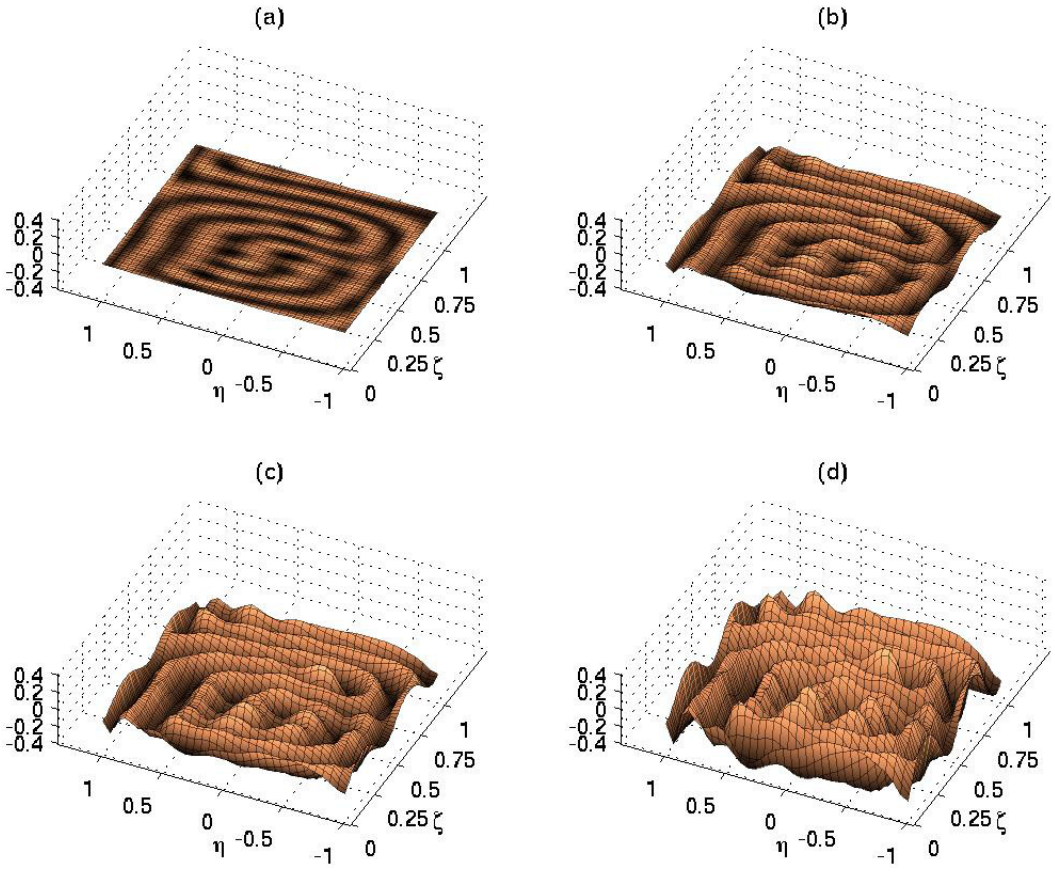


Figure B.2: Exponential growing domain Turing pattern as a prepattern for normal cortical fold development. Figures (a) through (d) provide a visualization of how a labyrinthine cortical folding pattern could develop from a genetic chemical Turing prepattern by plotting the activator concentration $u$ on the $z$-axis for $z = 0$, $z = \frac{u}{4}$, $z = \frac{u}{2}$, and $z = u$, respectively. The pattern represents normal cortical development and corresponds to the final pattern in Figure B.1. See also: animation.

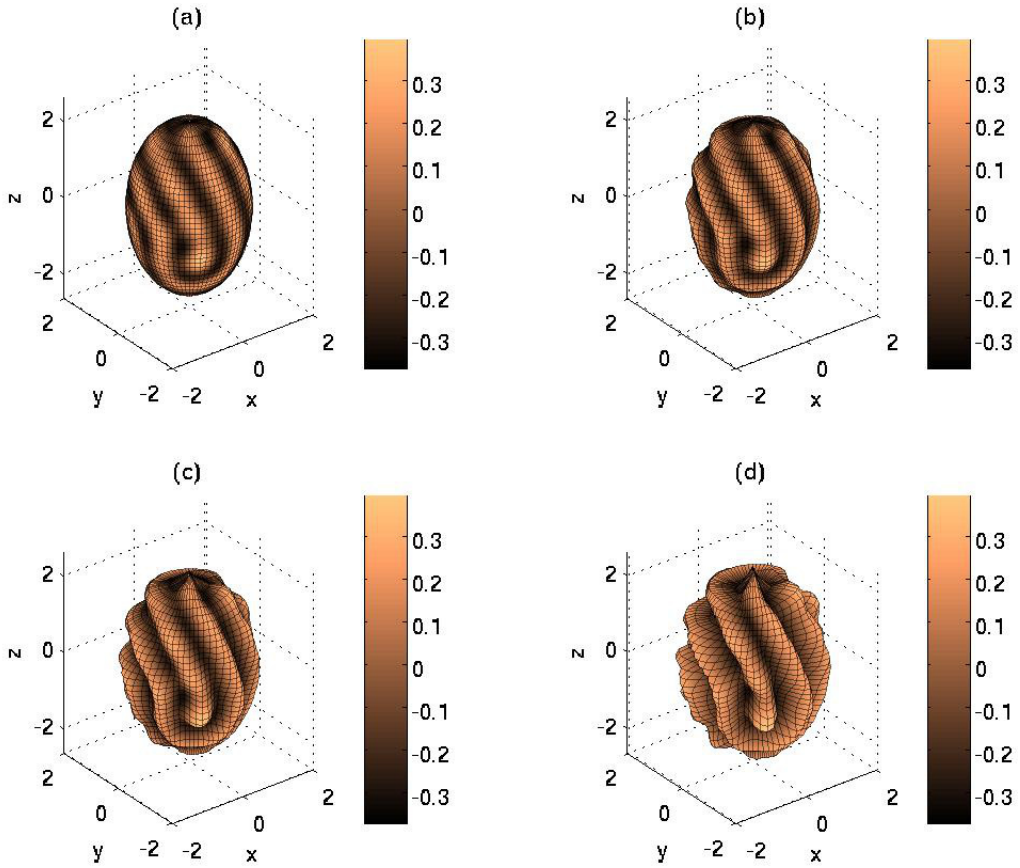


Figure B.3: Prolate spheroid visualization of exponentially growing domain Turing prepattern for normal cortical fold development. Projecting the images from Figure B.2 onto the corresponding prolate spheroidal domain gives a new way to visualize how a labyrinthine pattern representing normal cortical folding could develop from a chemical Turing prepattern (refer to Figure B.1 at $t = 35$). See also: animation.

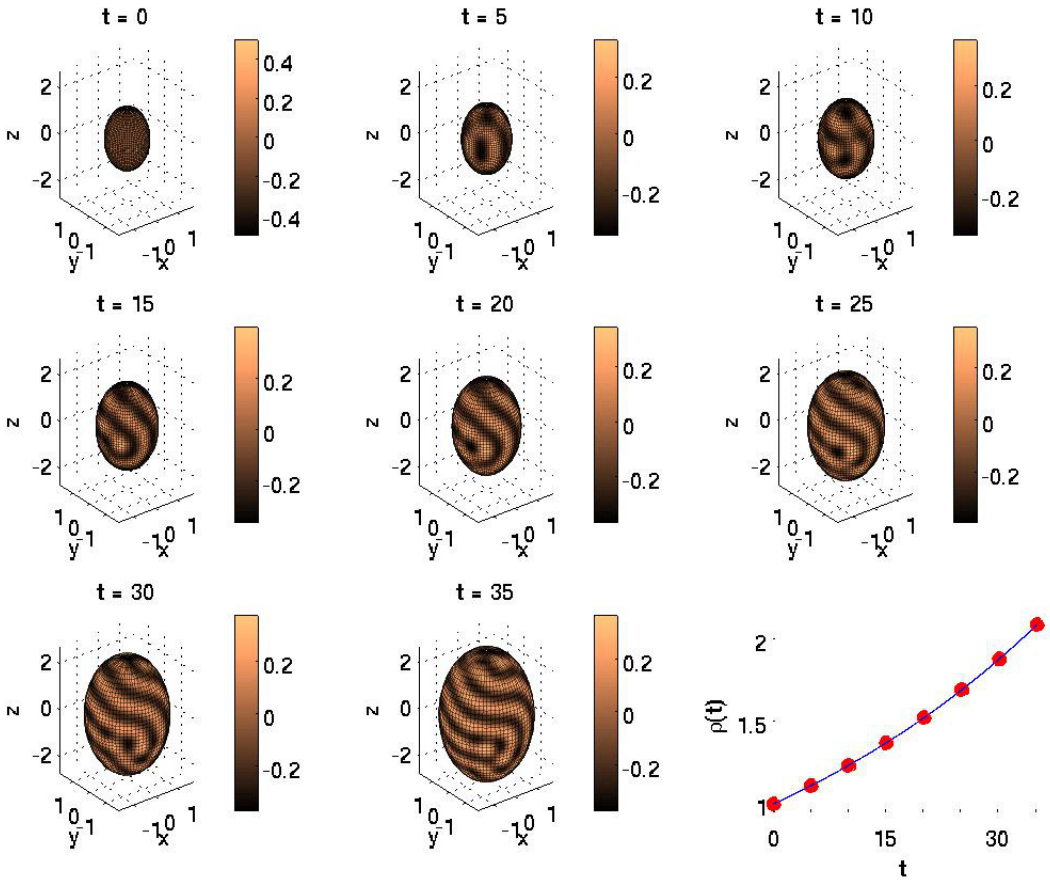


Figure B.4: Evolution of Turing pattern on an exponentially growing prolate spheroid representing polymicrogyria. The pattern was generated by System (4.23) with $R = 0.021, \omega = 115$ and kinetics parameters listed on page 34. The bottom right figure indicates when each snapshot was taken. See also: animation.

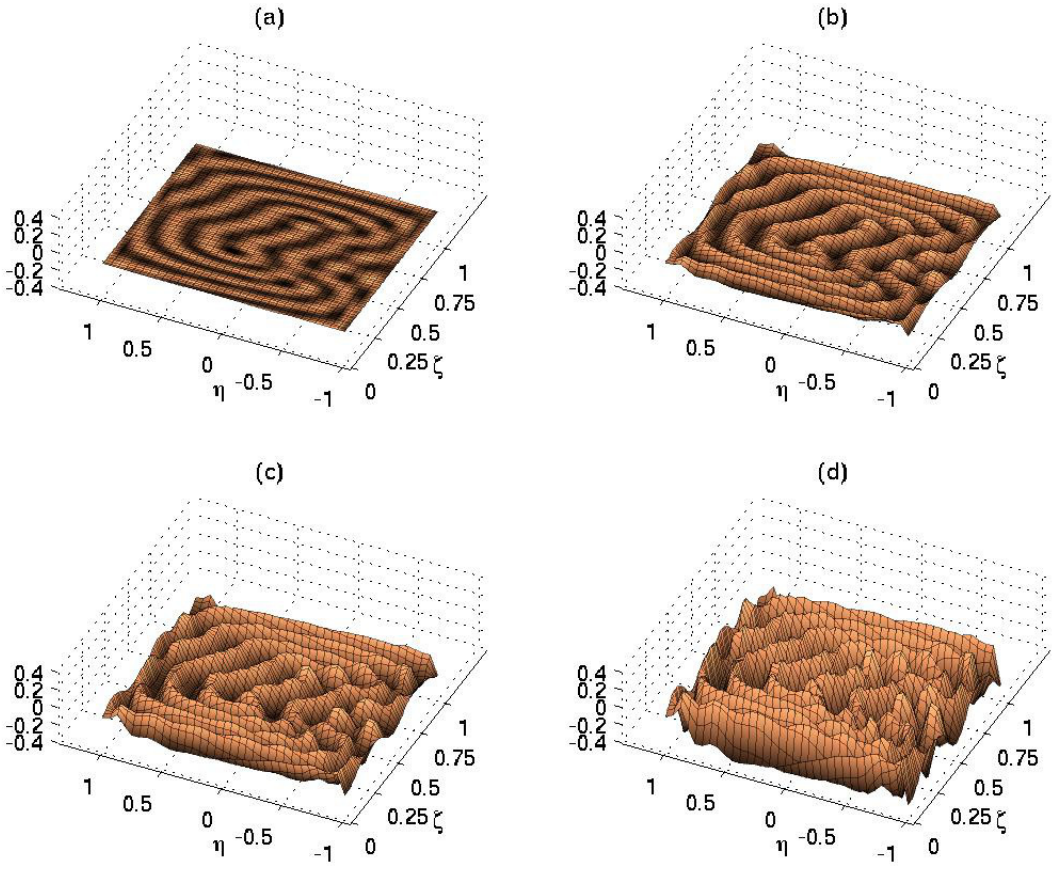


Figure B.5: Exponential growing domain Turing pattern as a prepattern for polymicrogyria. Figures (a) through (d) provide a visualization of how a labyrinthine cortical folding pattern could develop from a genetic chemical Turing prepattern by plotting the activator concentration $u$ on the $z$-axis for $z = 0$, $z = \frac{u}{4}$, $z = \frac{u}{2}$, and $z = u$, respectively. The pattern represents polymicrogyria and corresponds to the final pattern in Figure B.4. See also: animation.

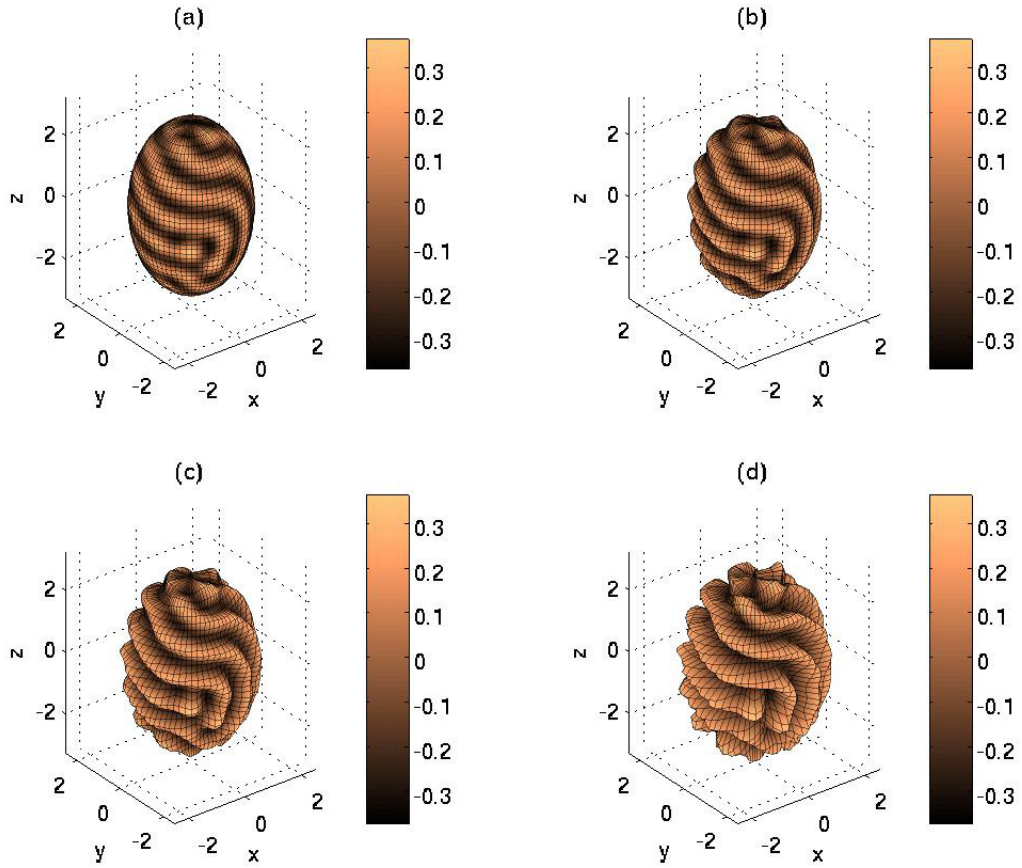


Figure B.6: Prolate spheroid visualization of exponentially growing domain Turing prepattern for polymicrogyria. Projecting the images from Figure B.5 onto the corresponding prolate spheroidal domain gives a new way to visualize how a labyrinthine pattern representing polymicrogyria could develop from a chemical Turing prepattern (refer to Figure B.4 at $t = 35$). See also: animation.

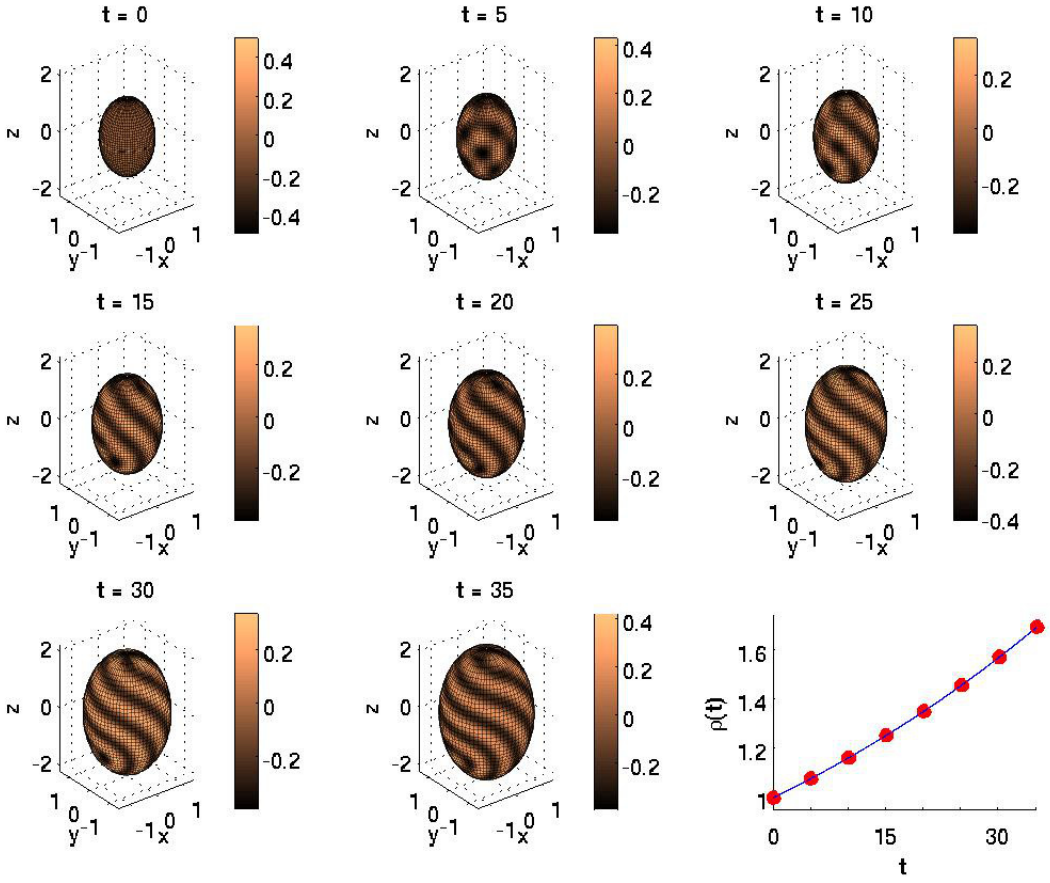


Figure B.7: Evolution of Turing pattern on an exponentially growing prolate spheroid representing polymicrogyria with microcephaly and enlarged lateral ventricles. The pattern was generated by System (4.23) with $R = 0.015, \omega = 150$ and kinetics parameters listed on page 34. The bottom right figure indicates when each snapshot was taken. See also: animation.

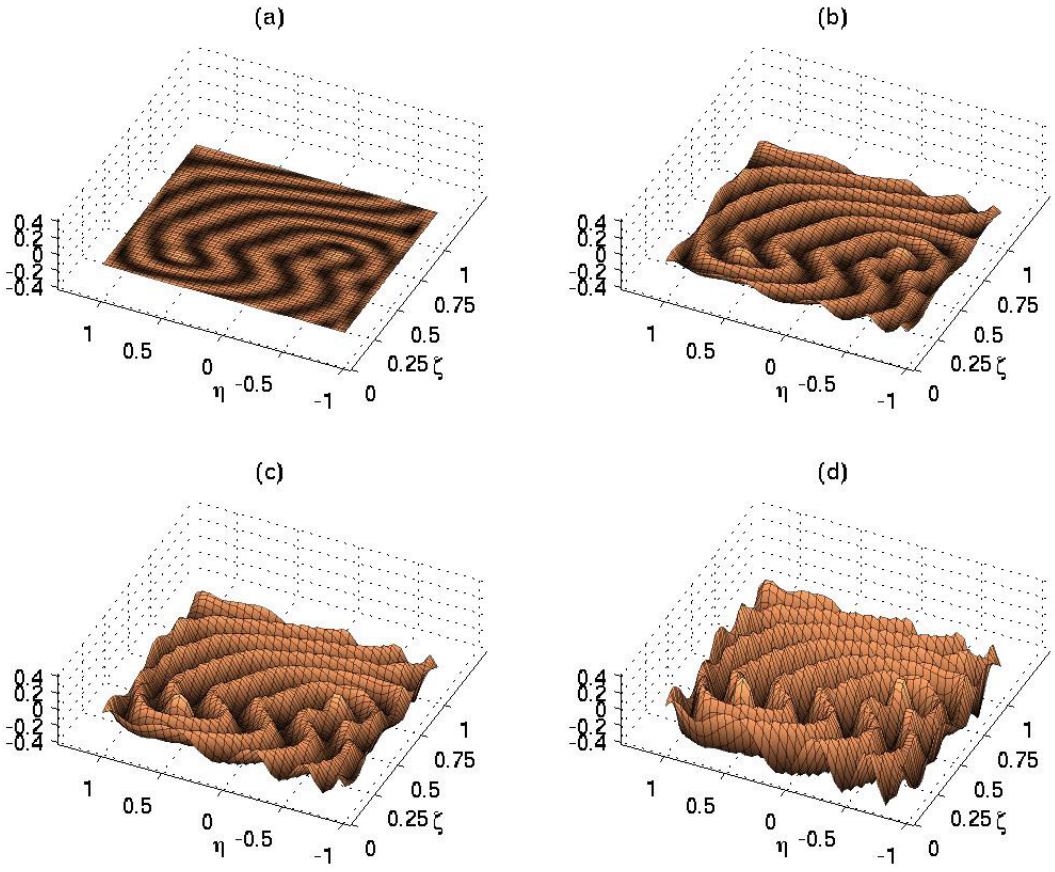


Figure B.8: Exponential growing domain Turing pattern as a prepattern for polymicrogyria with microcephaly and enlarged lateral ventricles. Figures (a) through (d) provide a visualization of how a labyrinthine cortical folding pattern could develop from a genetic chemical Turing prepattern by plotting the activator concentration $u$ on the $z$-axis for $z = 0$, $z = \frac{u}{4}$, $z = \frac{u}{2}$, and $z = u$, respectively. The pattern represents PMG with microcephaly and enlarged LVs and corresponds to the final pattern in Figure B.7. See also: animation.

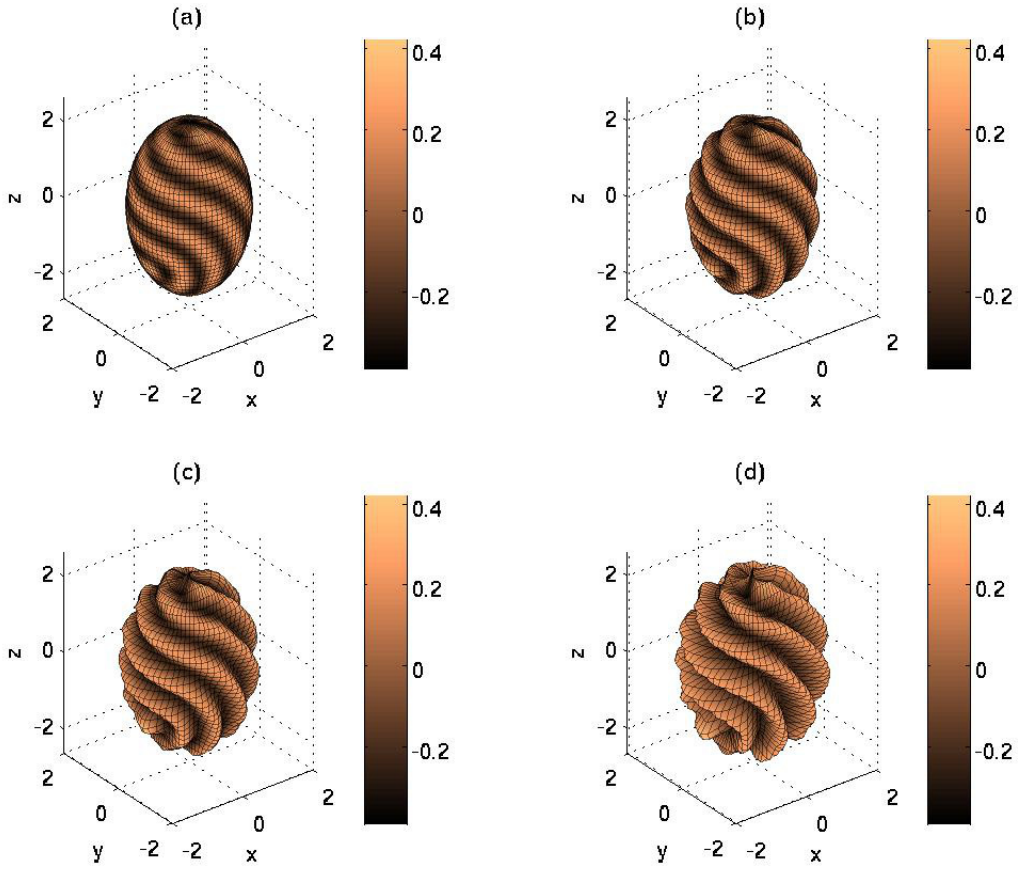


Figure B.9: Prolate spheroid visualization of exponentially growing domain Turing prepattern for polymicrogyria with microcephaly and enlarged lateral ventricles. Projecting the images from Figure B.8 onto the corresponding prolate spheroidal domain gives a new way to visualize how a labyrinthine pattern representing PMG with microcephaly and enlarged LVs could develop from a chemical Turing prepattern (refer to Figure B.7 at $t = 35$). See also: animation.

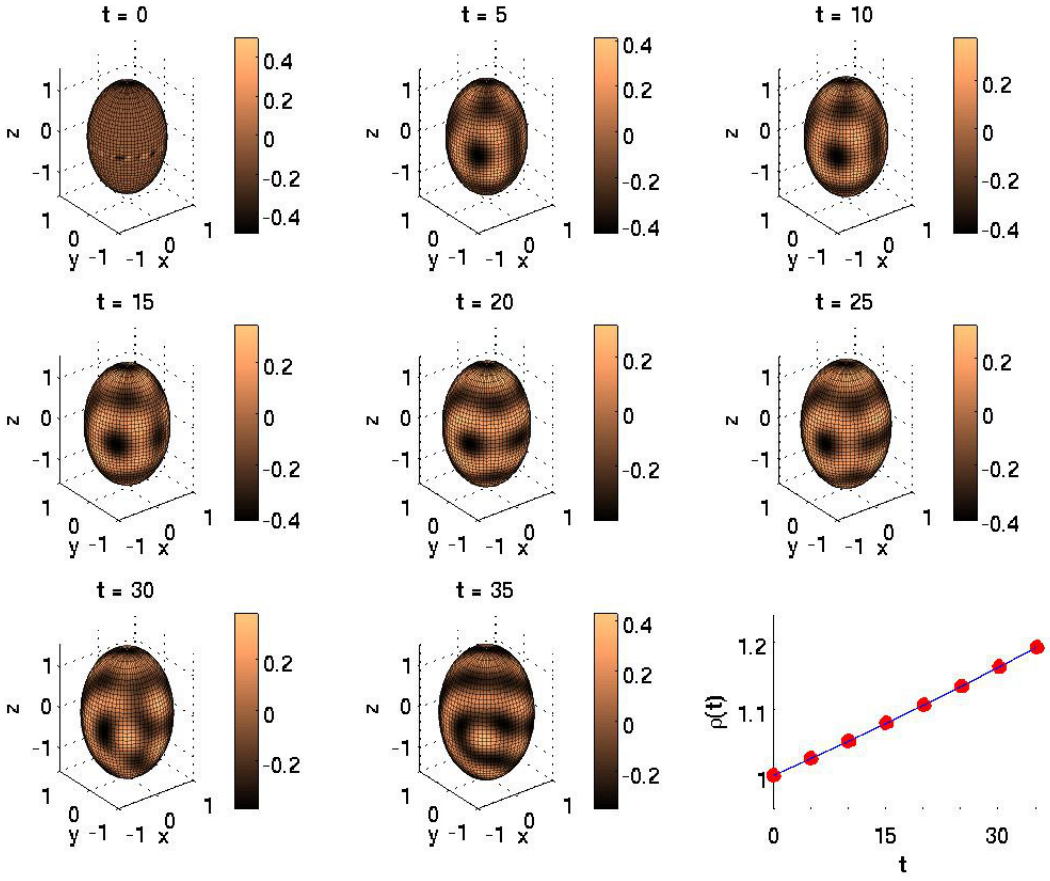


Figure B.10: Evolution of Turing pattern on an exponentially growing prolate spheroid representing the lissencephaly seen in Norman-Roberts Syndrome with non-enlarged lateral ventricles. The pattern was generated by System (4.23) with $R = 0.005, \omega = 115$ and kinetics parameters listed on page 34. The dots in the lower-right figure represent the time at which each snapshot was taken. See also: animation.

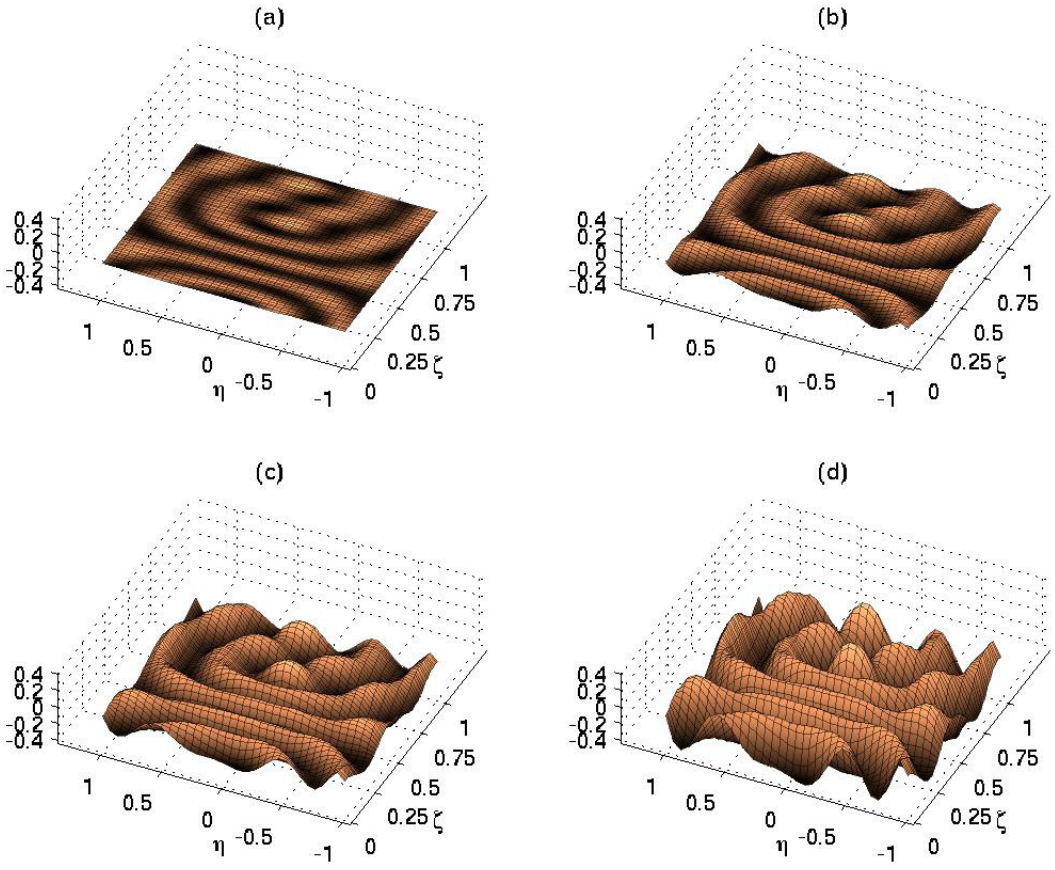


Figure B.11: Exponential growing domain Turing pattern as a prepattern for Norman-Roberts Syndrome with non-enlarged lateral ventricles. Figures (a) through (d) provide a visualization of how a labyrinthine cortical folding pattern could develop from a genetic chemical Turing prepattern by plotting the activator concentration $u$ on the $z$-axis for $z = 0$, $z = \frac{u}{4}$, $z = \frac{u}{2}$, and $z = u$, respectively. The pattern represents NRS with non-enlarged LVs and corresponds to the final pattern in Figure B.10. See also: animation.

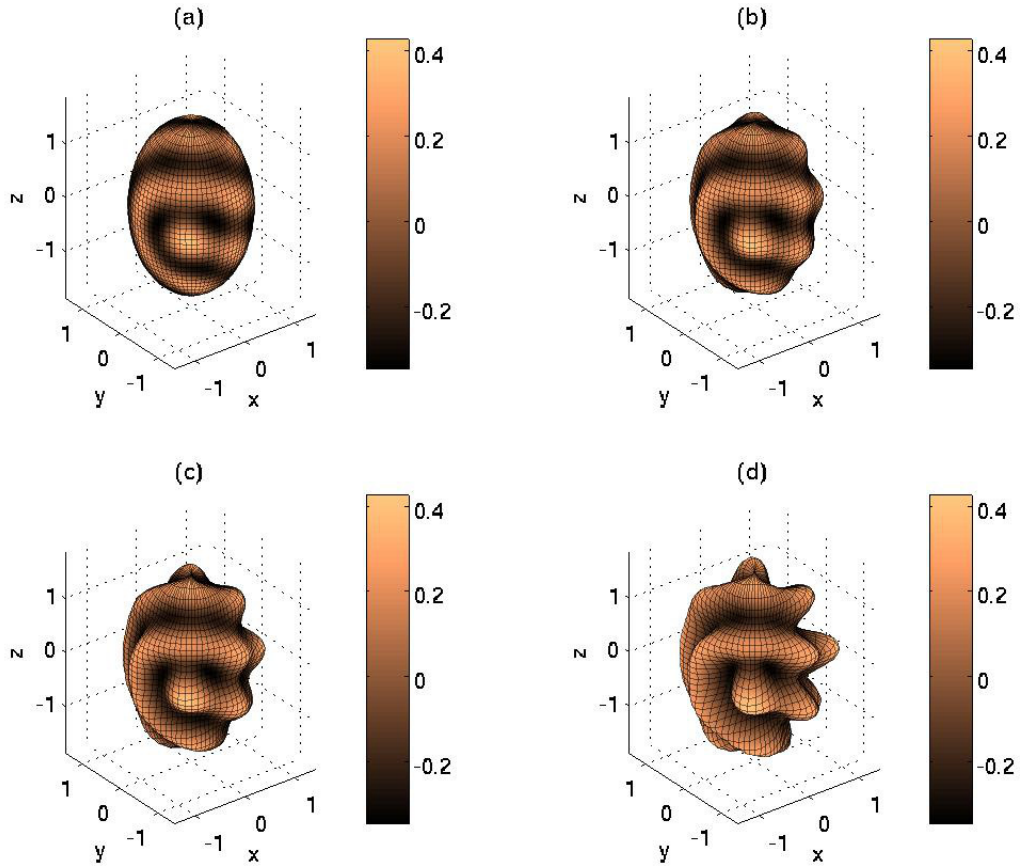


Figure B.12: Prolate spheroid visualization of exponentially growing domain Turing prepattern for Norman-Roberts Syndrome with non-enlarged lateral ventricles. Projecting the images from Figure B.11 onto the corresponding prolate spheroidal domain gives a new way to visualize how a labyrinthine pattern representing NRS with non-enlarged LVs could develop from a chemical Turing prepattern (refer to Figure B.10 at $t = 35$). See also: animation.

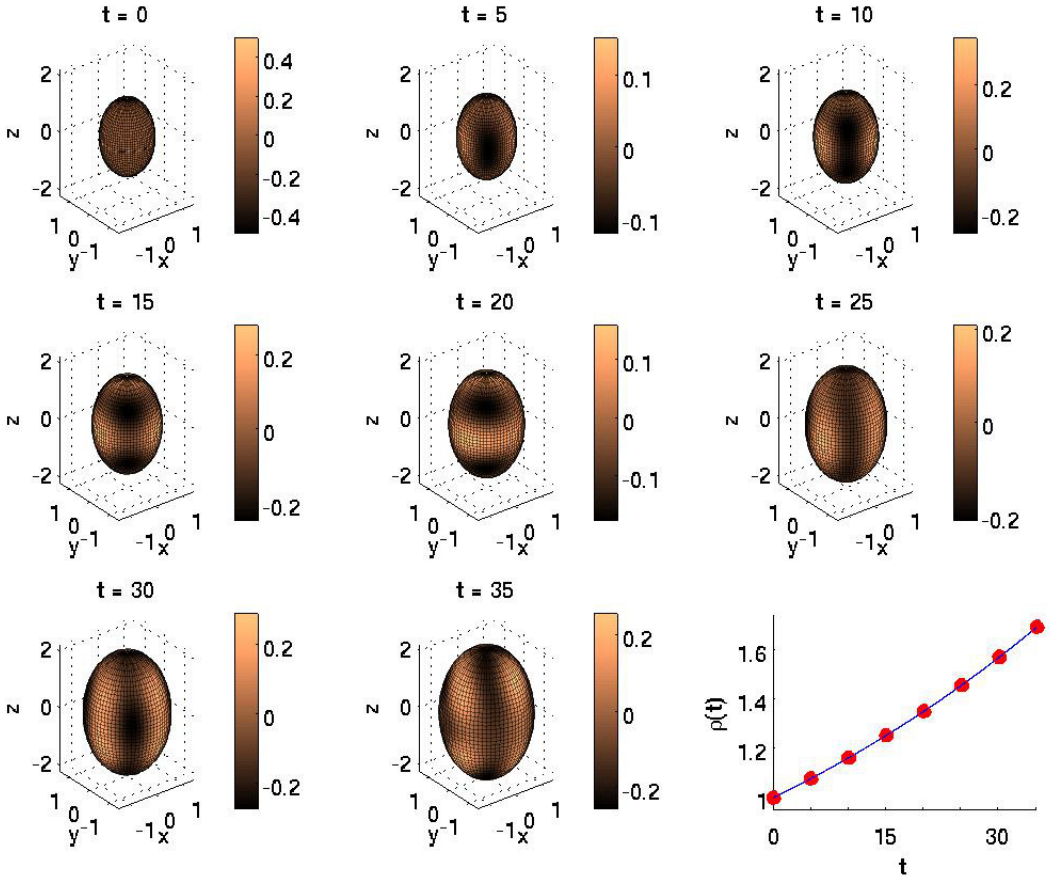


Figure B.13: Evolution of Turing pattern on an exponentially growing prolate spheroid representing the lissencephaly presented in Norman-Roberts Syndrome with enlarged lateral ventricles. The pattern was generated by System (4.23) with $R = 0.015, \omega = 30$ and kinetics parameters listed on page 34. The dots in the lower-right figure represent the time at which each snapshot was taken. See also: animation.

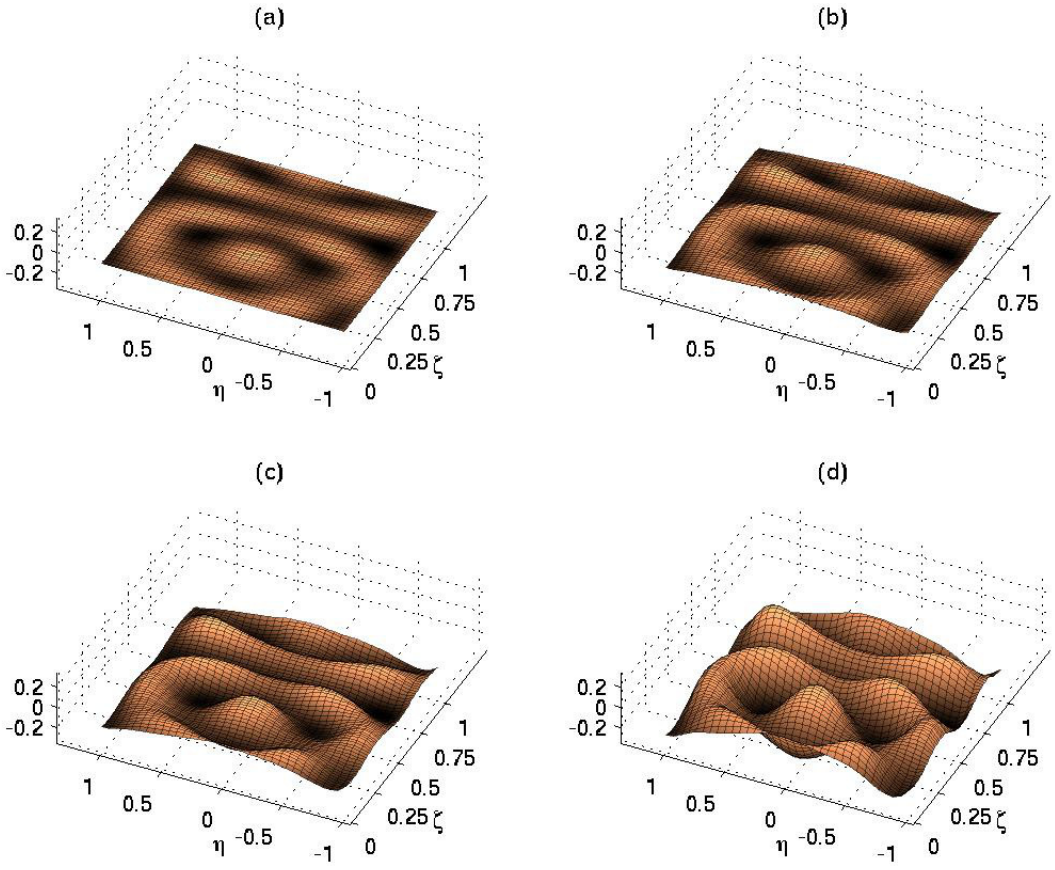


Figure B.14: Exponential growing domain Turing pattern as a prepattern for Norman-Roberts Syndrome with enlarged lateral ventricles. Figures (a) through (d) provide a visualization of how a labyrinthine cortical folding pattern could develop from a genetic chemical Turing prepattern by plotting the activator concentration $u$ on the $z$-axis for $z = 0$, $z = \frac{u}{4}$, $z = \frac{u}{2}$, and $z = u$, respectively. The pattern represents NRS with enlarged LVs and corresponds to the final pattern in Figure B.13. See also: animation.

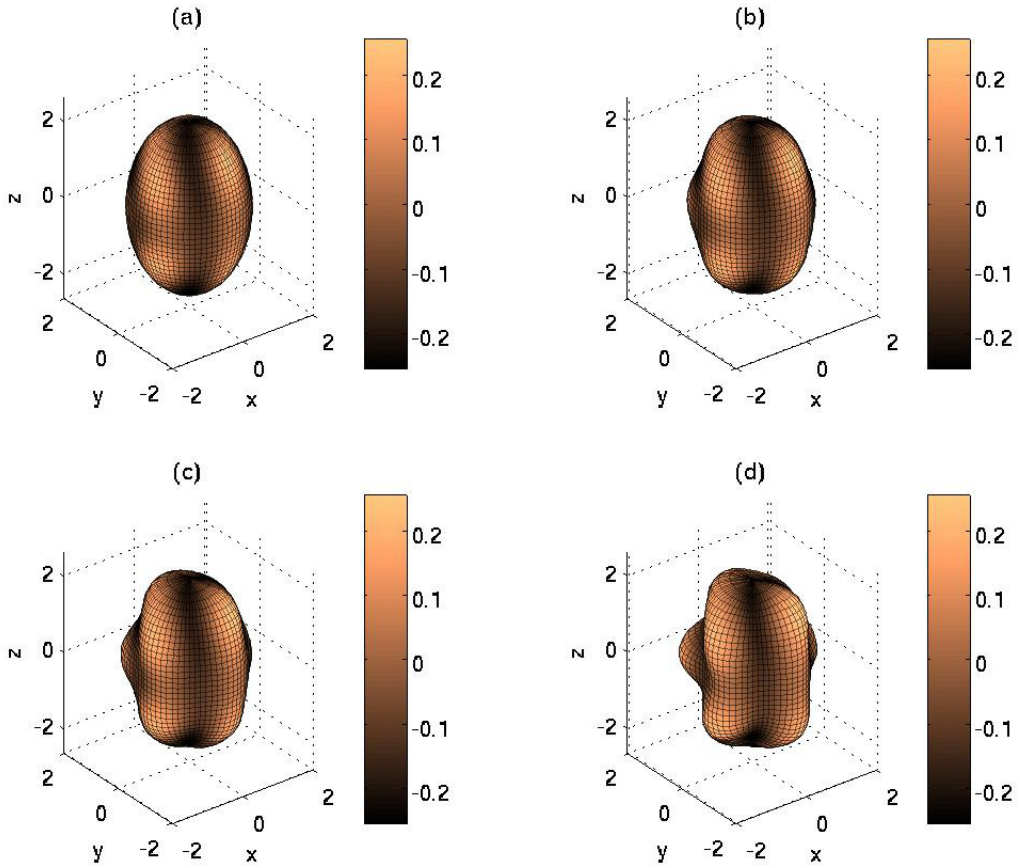


Figure B.15: Prolate spheroid visualization of exponentially growing domain Turing prepattern for Norman-Roberts Syndrome with enlarged lateral ventricles. Projecting the images from Figure B.14 onto the corresponding prolate spheroidal domain gives a new way to visualize how a labyrinthine pattern representing NRS with enlarged LVs could develop from a chemical Turing prepattern (refer to Figure B.13 at $t = 35$). See also: animation.

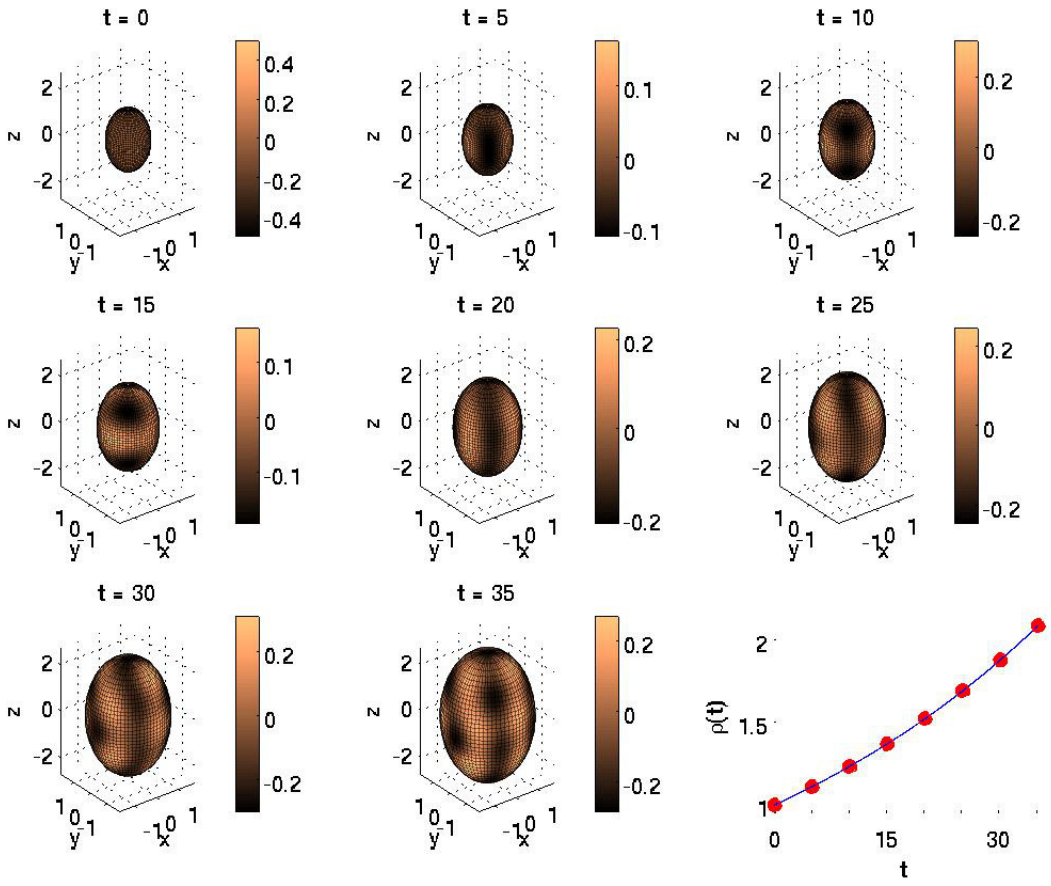


Figure B.16: Evolution of Turing pattern on an exponentially growing prolate spheroid representing normocephalic type I lissencephaly with enlarged lateral ventricles. The pattern was generated by System (4.23) with $R = 0.021, \omega = 30$ and kinetics parameters listed on page 34. The dots in the lower-right figure represent the time at which each snapshot was taken. See also: animation.

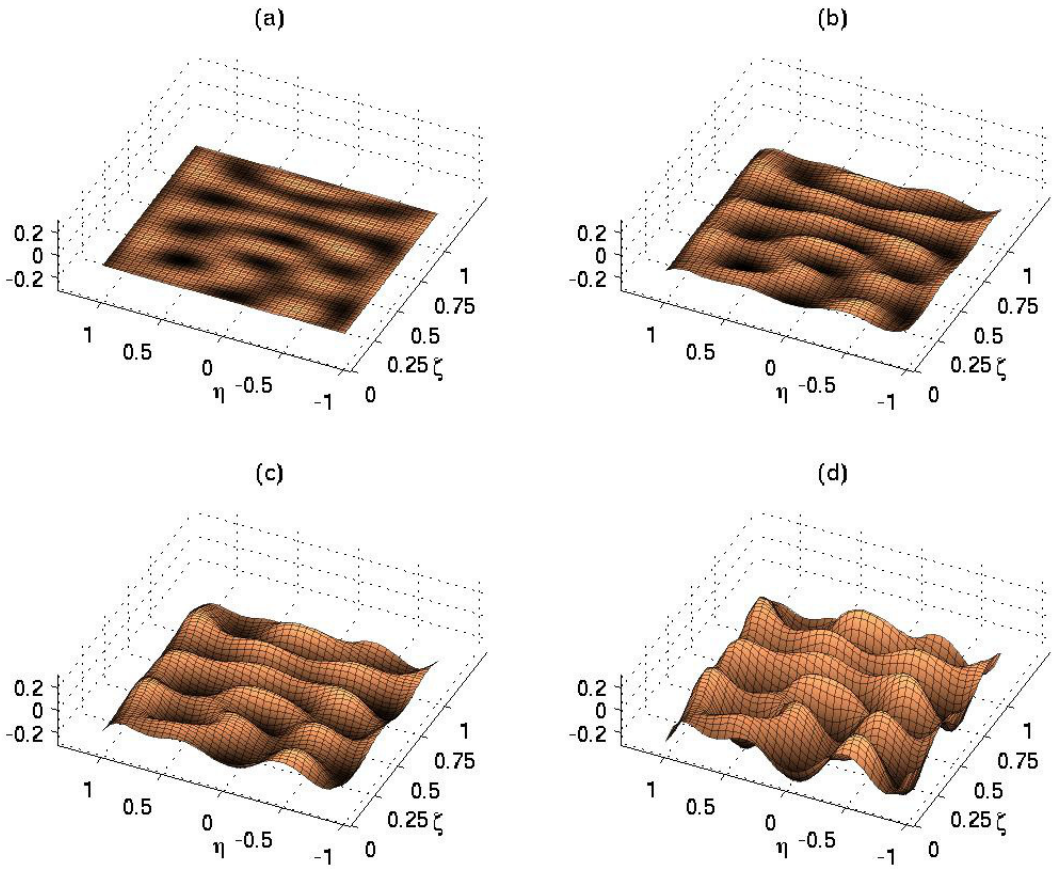


Figure B.17: Exponential growing domain Turing pattern as a prepattern for normocephalic type I lissencephaly with enlarged lateral ventricles. Figures (a) through (d) provide a visualization of how a labyrinthine cortical folding pattern could develop from a genetic chemical Turing prepattern by plotting the activator concentration $u$ on the $z$-axis for $z = 0$, $z = \frac{u}{4}$, $z = \frac{u}{2}$, and $z = u$, respectively. The pattern represents normocephalic type I lissencephaly with enlarged LVs and corresponds to the final pattern in Figure B.16. See also: animation.

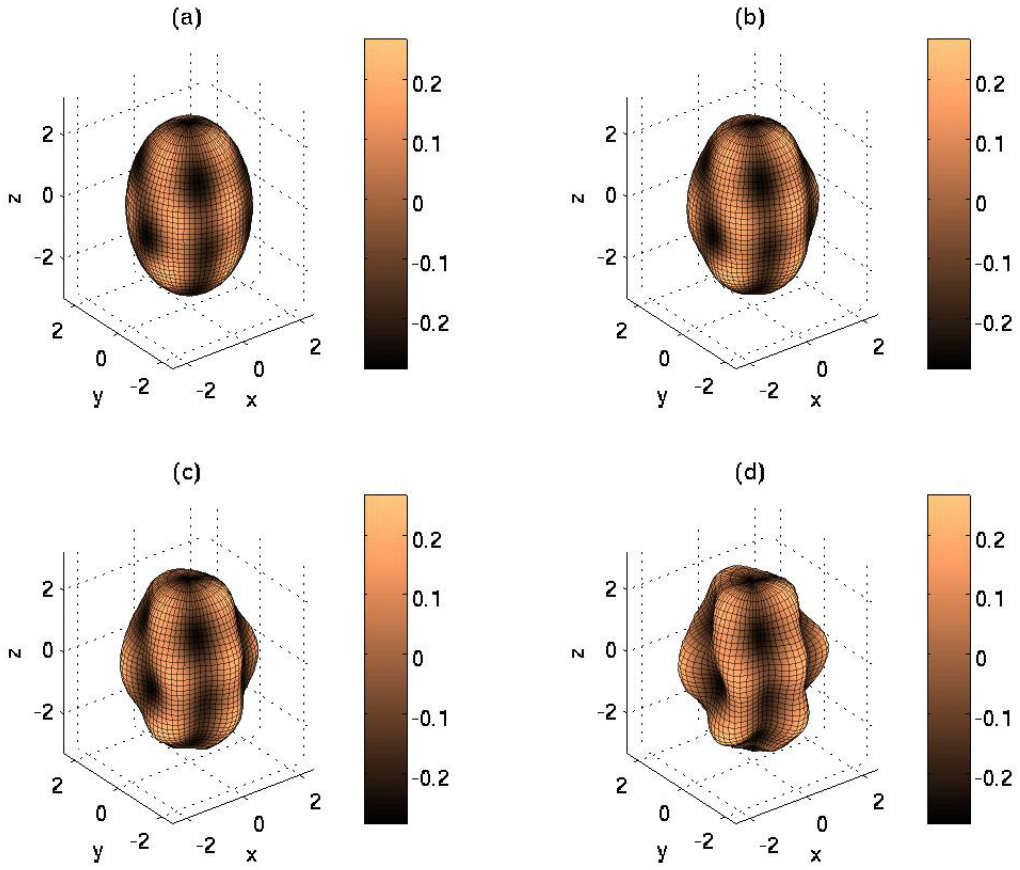


Figure B.18: Prolate spheroid visualization of exponentially growing domain Turing prepattern for normocephalic type I lissencephaly with enlarged lateral ventricles. Projecting the images from Figure B.17 onto the corresponding prolate spheroidal domain gives a new way to visualize how a labyrinthine pattern representing normocephalic type I lissencephaly with enlarged LVs could develop from a chemical Turing prepattern (refer to Figure B.16 at $t = 35$). See also: animation.

## B.2 Logistically Growing Model

This section contains the full pattern evolution and labyrinthine visualization figures for the logistically growing patterns presented in Chapter 6. Correspondence between the figures and the diseases they represent is given in Table B.2.

Table B.2: Logistic domain growth simulation results. Simulation results for polymicrogyria and lissencephaly are discussed in detail in Chapter 6.

(a) Polymicrogyria

| Growth Function | Figure Type | Normal ($R = 0.015$, $\omega = 115$) | PMG, enlarged LVs ($R = 0.021$, $\omega = 115$) | PMG, microcephaly, enlarged LVs ($R = 0.015$, $\omega = 150$) |
|---|---|---|---|---|
| Logistic | Prolate spheroid prepattern | Figs. 6.8a, B.19 | Figs. 6.8d, B.22 | Figs. 6.8g, B.25 |
| | Rectangular domain folding pattern | Figs. 6.8b, B.20 | Figs. 6.8e, B.23 | Figs. 6.8h, B.26 |
| | Prolate spheroid folding pattern | Figs. 6.8c, B.21 | Figs. 6.8f, B.24 | Figs. 6.8i, B.27 |

(b) Lissencephaly

| Growth Function | Figure Type | Normal ($R = 0.015$, $\omega = 115$) | NRS, LVs non-enlarged ($R = 0.005$, $\omega = 115$) | NRS, LVs enlarged ($R = 0.015$, $\omega = 30$) | Type I lissencephaly, normo-cephaly, enlarged LVs ($R = 0.021$, $\omega = 30$) |
|---|---|---|---|---|---|
| Logistic | Prolate spheroid prepattern | Figs. 6.12a, B.19 | Figs. 6.12d, B.28 | Figs. 6.12g, B.31 | Figs. 6.12j, B.34 |
| | Rectangular domain folding pattern | Figs. 6.12b, B.20 | Figs. 6.12e, B.29 | Figs. 6.12h, B.32 | Figs. 6.12k, B.35 |
| | Prolate spheroid folding pattern | Figs. 6.12c, B.21 | Figs. 6.12f, B.30 | Figs. 6.12i, B.33 | Figs. 6.12l, B.36 |

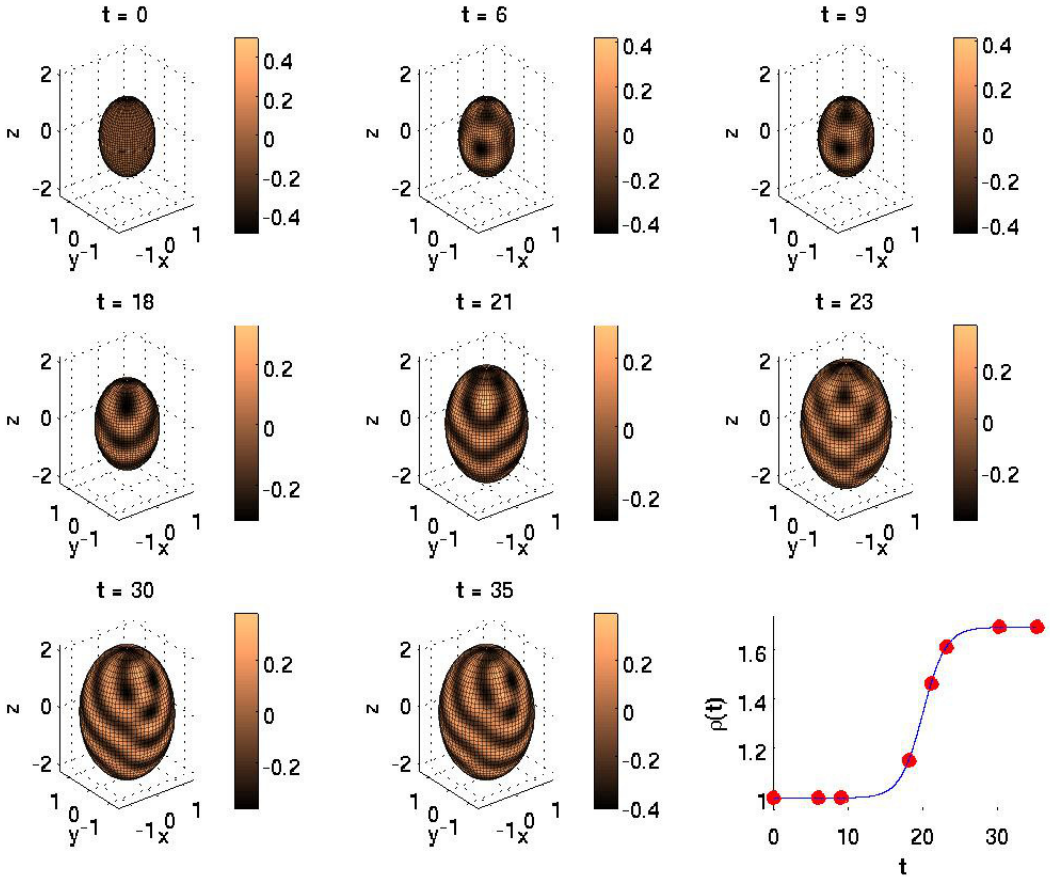


Figure B.19: Evolution of Turing pattern on a logistically growing prolate spheroid representing normal cortical development. The pattern was generated by System (5.5) with $R = 0.015, \omega = 115, t_{\text{final}} = 35, r = 0.6603, t_0 = 19.9258, K^\star = e^{Rt_{\text{final}}} - 1$ and kinetics parameters listed on page 34. The times at which the snapshots were taken are indicated as dots in the bottom right figure. See also: animation.

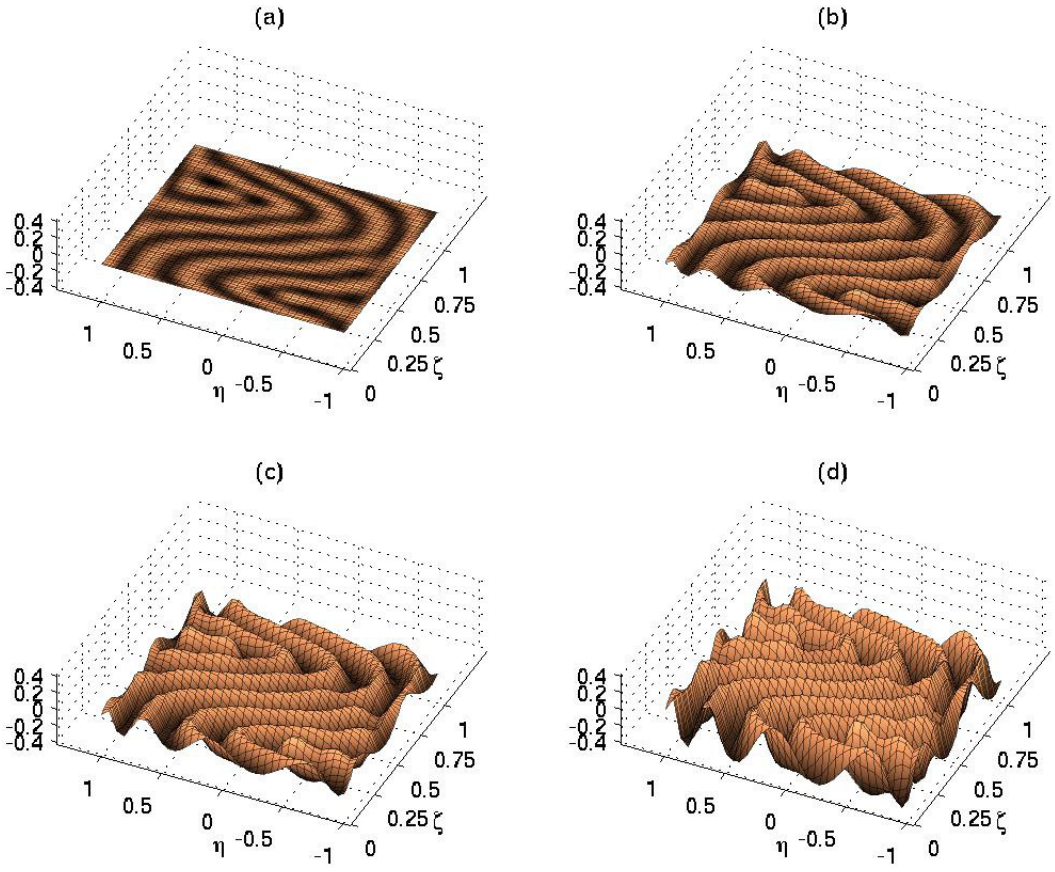


Figure B.20: Logistically growing domain Turing pattern as a prepattern for normal cortical fold development. Figures (a) through (d) provide a visualization of how a labyrinthine cortical folding pattern could develop from a genetic chemical Turing prepattern by plotting the activator concentration $u$ on the $z$-axis for $z = 0$, $z = \frac{u}{4}$, $z = \frac{u}{2}$, and $z = u$, respectively. The pattern represents normal cortical development and corresponds to the final pattern in Figure B.19. See also: animation.

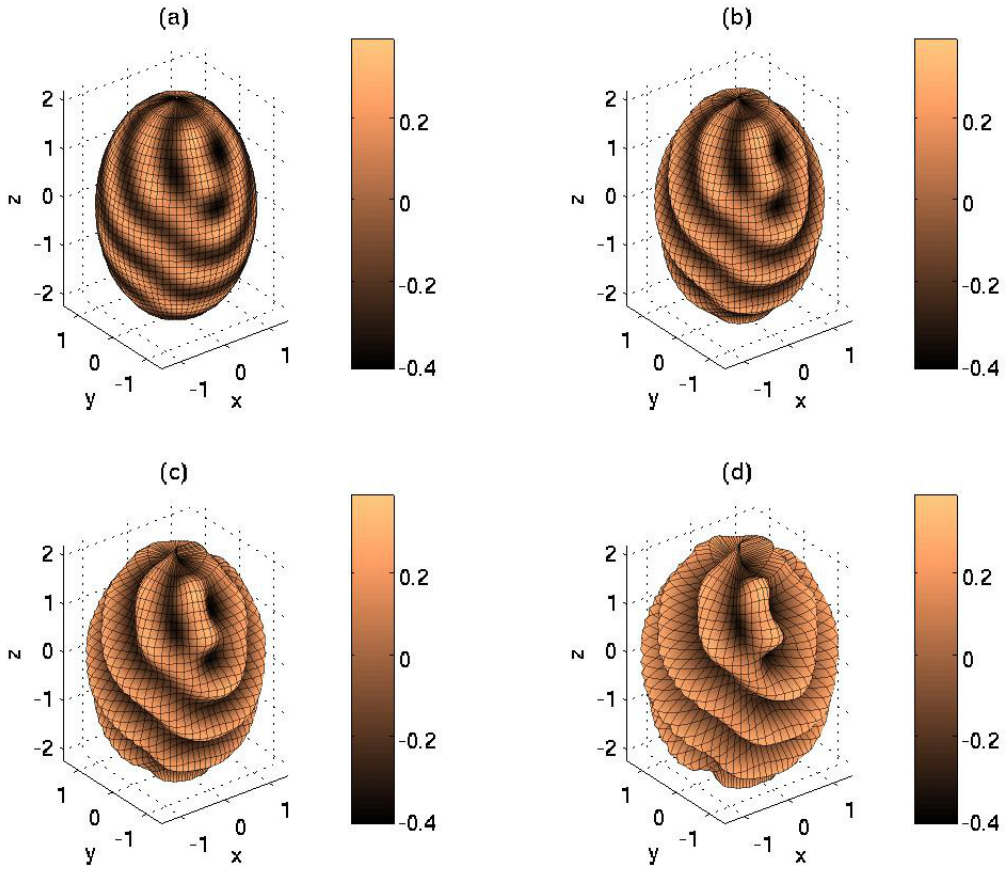


Figure B.21: Prolate spheroid visualization of logistically growing domain Turing prepattern for normal cortical fold development. Projecting the images from Figure B.20 onto the corresponding prolate spheroidal domain gives a new way to visualize how a labyrinthine pattern representing normal cortical folding could develop from a chemical Turing prepattern (refer to Figure B.19 at $t = 35$). See also: animation.

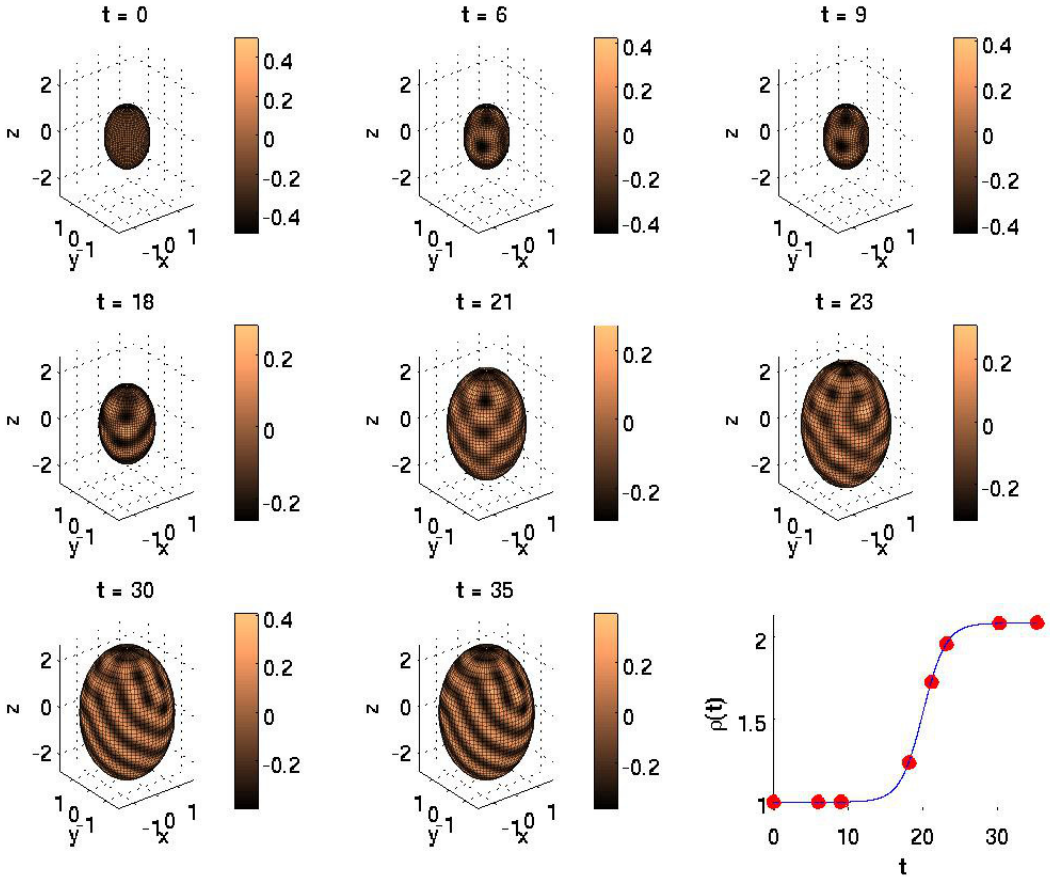


Figure B.22: Evolution of Turing pattern on a logistically growing prolate spheroid representing polymicrogyria. The pattern was generated by System (5.5) with $R = 0.021, \omega = 115, t_{\text{final}} = 35, r = 0.6603, t_0 = 19.9258, K^\star = e^{Rt_{\text{final}}} - 1$ and kinetics parameters listed on page 34. The bottom right figure uses dots to depict the times at which the snapshots were taken. See also: animation.

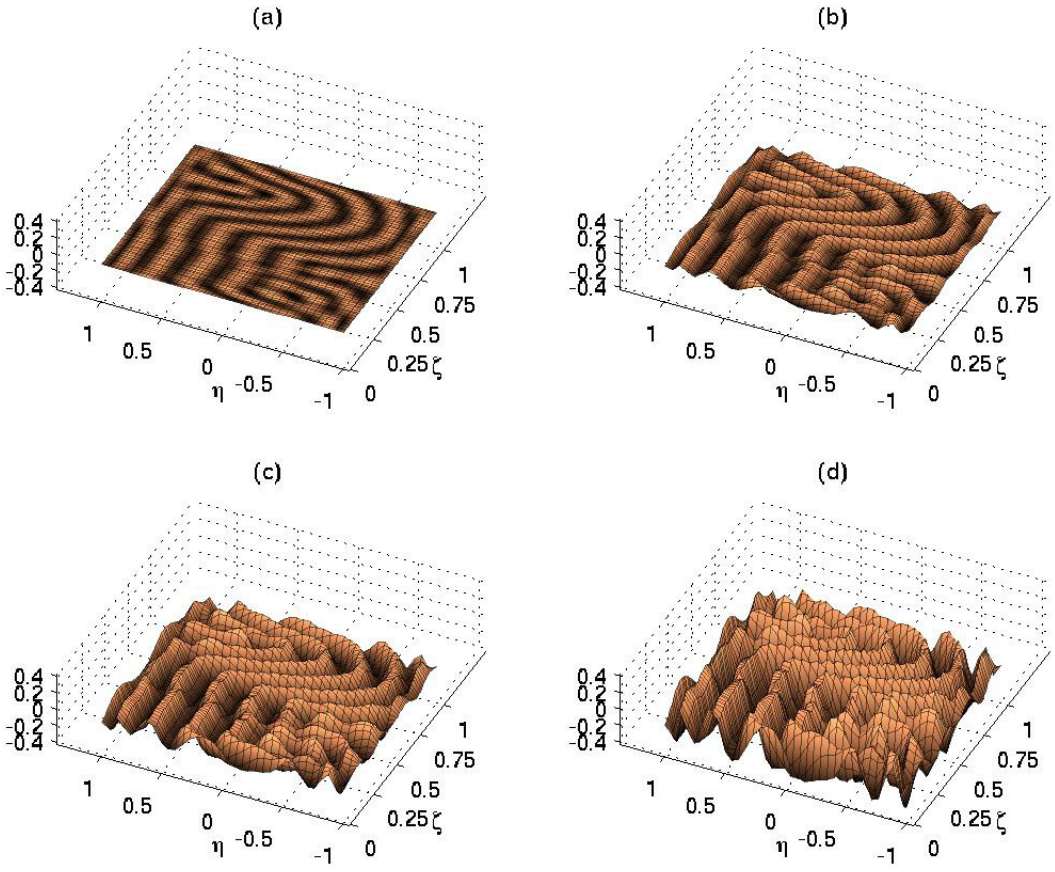


Figure B.23: Logistically growing domain Turing pattern as a prepattern for polymicrogyria. Figures (a) through (d) provide a visualization of how a labyrinthine cortical folding pattern could develop from a genetic chemical Turing prepattern by plotting the activator concentration $u$ on the $z$-axis for $z = 0$, $z = \frac{u}{4}$, $z = \frac{u}{2}$, and $z = u$, respectively. The pattern represents polymicrogyria and corresponds to the final pattern in Figure B.22. See also: animation.

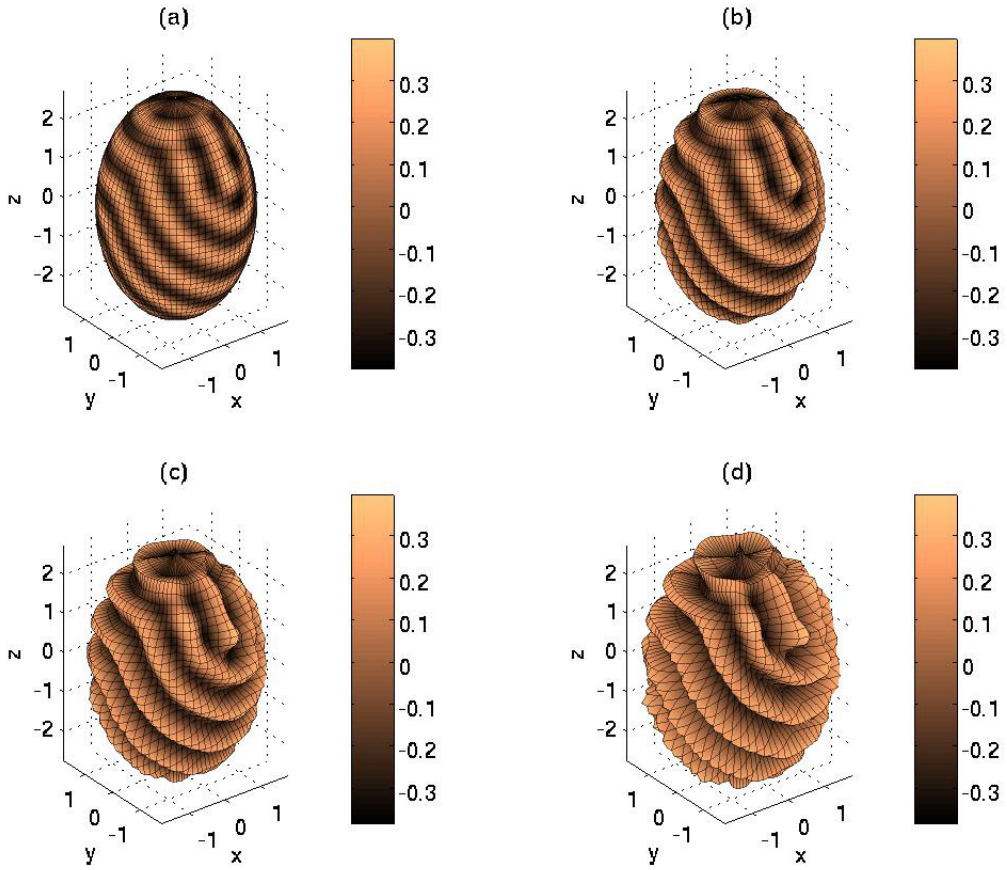


Figure B.24: Prolate spheroid visualization of logistically growing domain Turing prepattern for polymicrogyria. Projecting the images from Figure B.23 onto the corresponding prolate spheroidal domain gives a new way to visualize how a labyrinthine pattern representing polymicrogyria could develop from a chemical Turing prepattern (refer to Figure B.22 at $t = 35$). See also: animation.

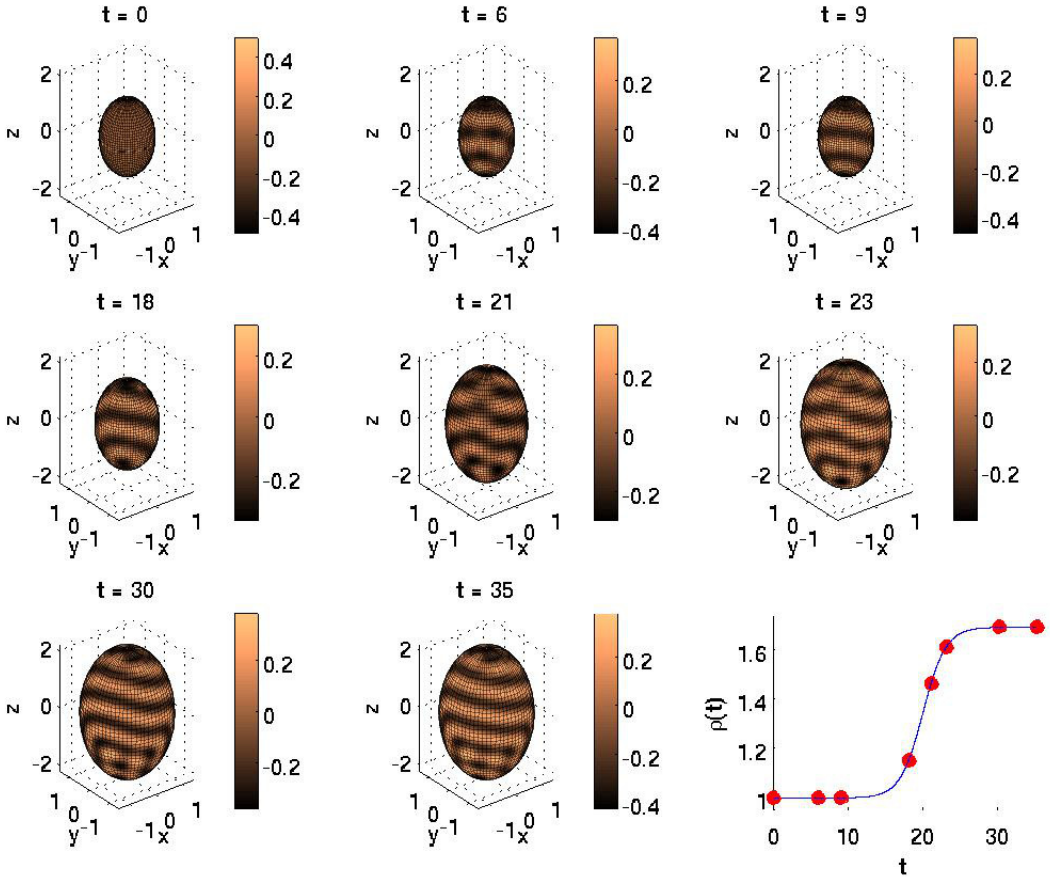


Figure B.25: Evolution of Turing pattern on a logistically growing prolate spheroid representing polymicrogyria with microcephaly and enlarged lateral ventricles. The pattern was generated by System (5.5) with $R = 0.015, \omega = 150, t_{\text{final}} = 35, r = 0.6603, t_0 = 19.9258, K^\star = e^{Rt_{\text{final}}} - 1$ and kinetics parameters listed on page 34. The bottom right figure uses dots to depict the times at which the snapshots were taken. See also: animation.

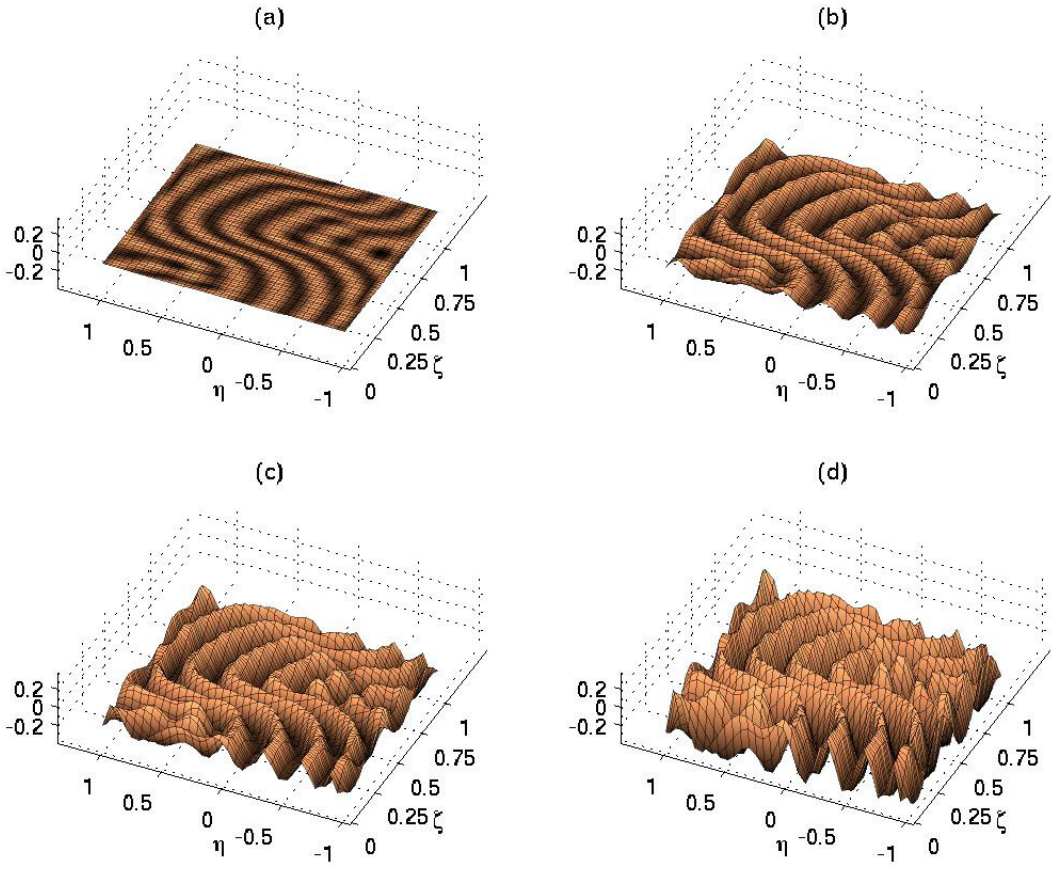


Figure B.26: Logistically growing domain Turing pattern as a prepattern for polymicrogyria with microcephaly and enlarged lateral ventricles. Figures (a) through (d) provide a visualization of how a labyrinthine cortical folding pattern could develop from a genetic chemical Turing prepattern by plotting the activator concentration $u$ on the $z$-axis for $z = 0$, $z = \frac{u}{4}$, $z = \frac{u}{2}$, and $z = u$, respectively. The pattern represents PMG with microcephaly and enlarged LVs and corresponds to the final pattern in Figure B.25. See also: animation.

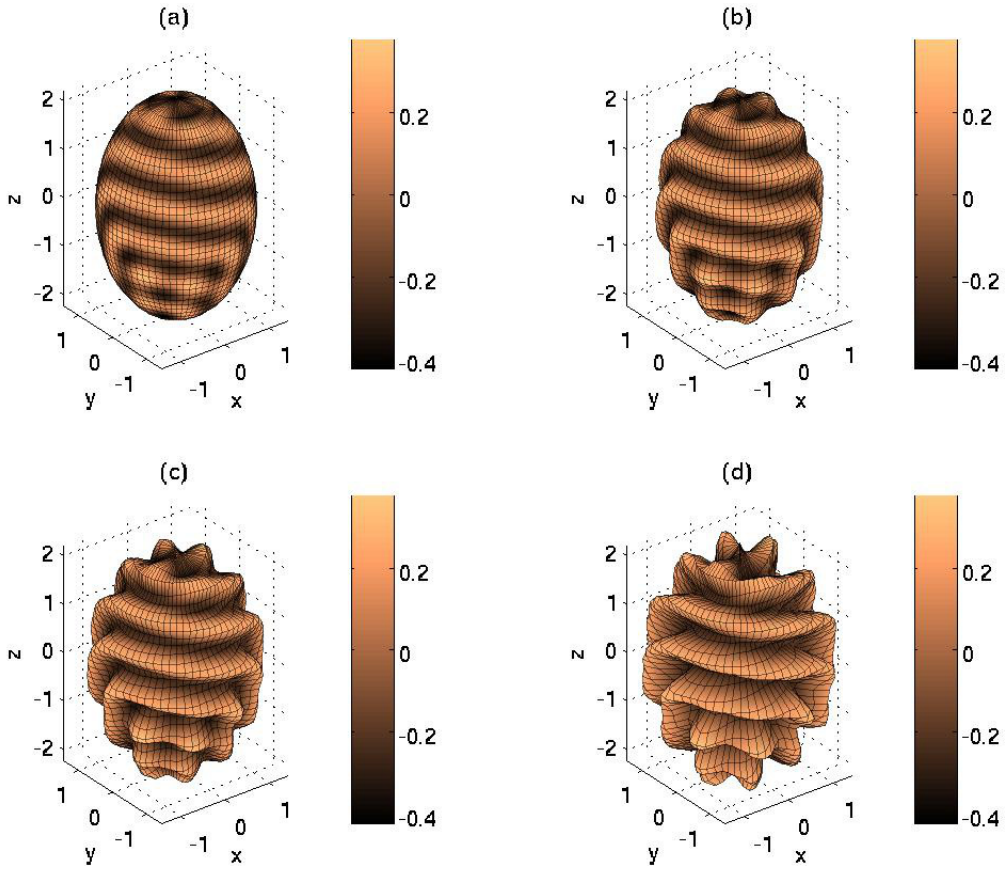


Figure B.27: Prolate spheroid visualization of logistically growing domain Turing prepattern for polymicrogyria with microcephaly and enlarged lateral ventricles. Projecting the images from Figure B.26 onto the corresponding prolate spheroidal domain gives a new way to visualize how a labyrinthine pattern representing PMG with microcephaly and enlarged LVs could develop from a chemical Turing prepattern (refer to Figure B.25 at $t = 35$). See also: animation.

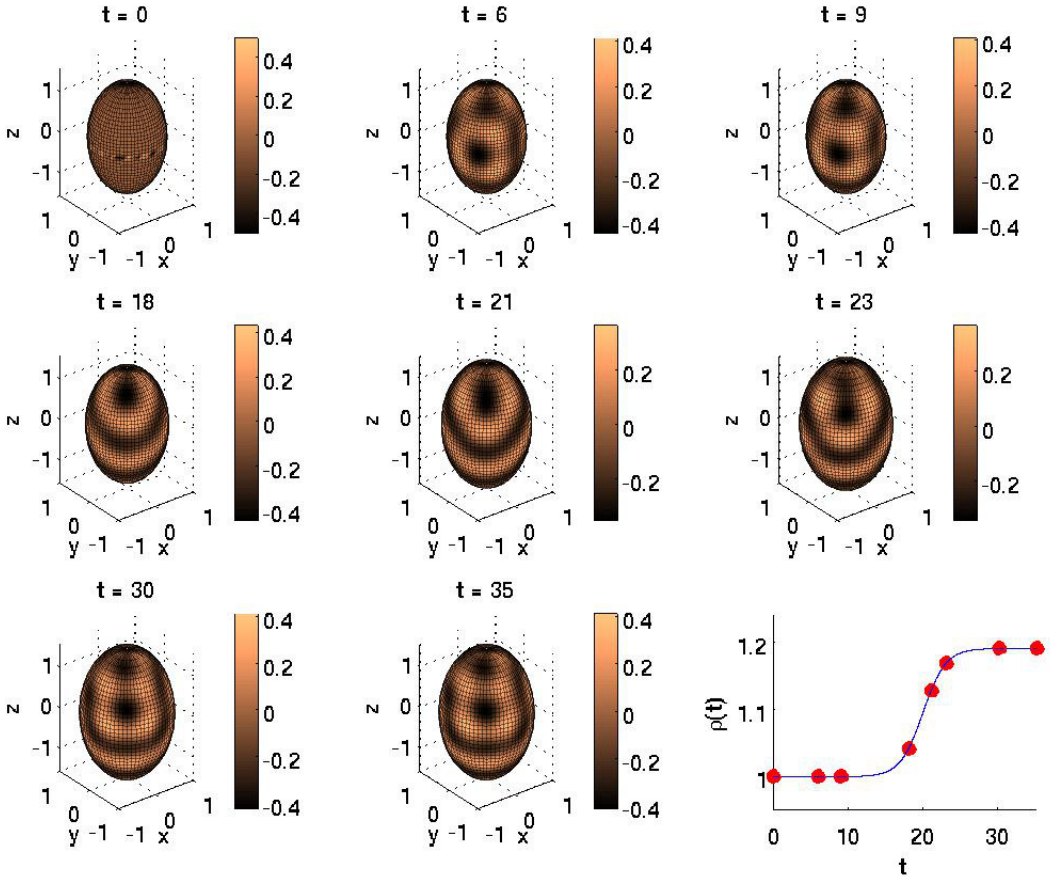


Figure B.28: Evolution of Turing pattern on a logistically growing prolate spheroid representing the lissencephaly seen in Norman-Roberts Syndrome with non-enlarged lateral ventricles. The pattern was generated by System (5.5) with $R = 0.005, \omega = 115, t_{\text{final}} = 35, r = 0.6603, t_0 = 19.9258, K^\star = e^{Rt_{\text{final}}} - 1$ and kinetics parameters listed on page 34. Dots in the bottom right figure correspond to the time at which each snapshot was taken. See also: animation.

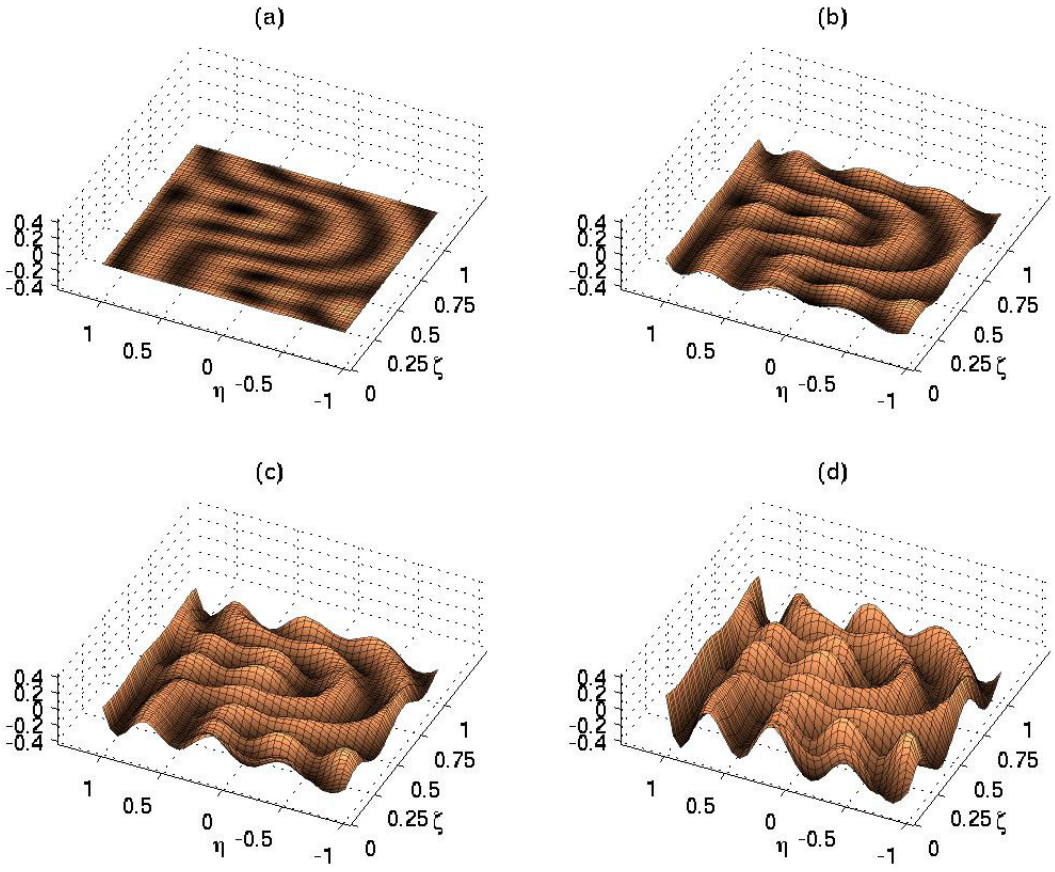


Figure B.29: Logistically growing domain Turing pattern as a prepattern for Norman-Roberts Syndrome with non-enlarged lateral ventricles. Figures (a) through (d) provide a visualization of how a labyrinthine cortical folding pattern could develop from a genetic chemical Turing prepattern by plotting the activator concentration $u$ on the $z$-axis for $z = 0$, $z = \frac{u}{4}$, $z = \frac{u}{2}$, and $z = u$, respectively. The pattern represents NRS with non-enlarged LVs and corresponds to the final pattern in Figure B.28. See also: animation.

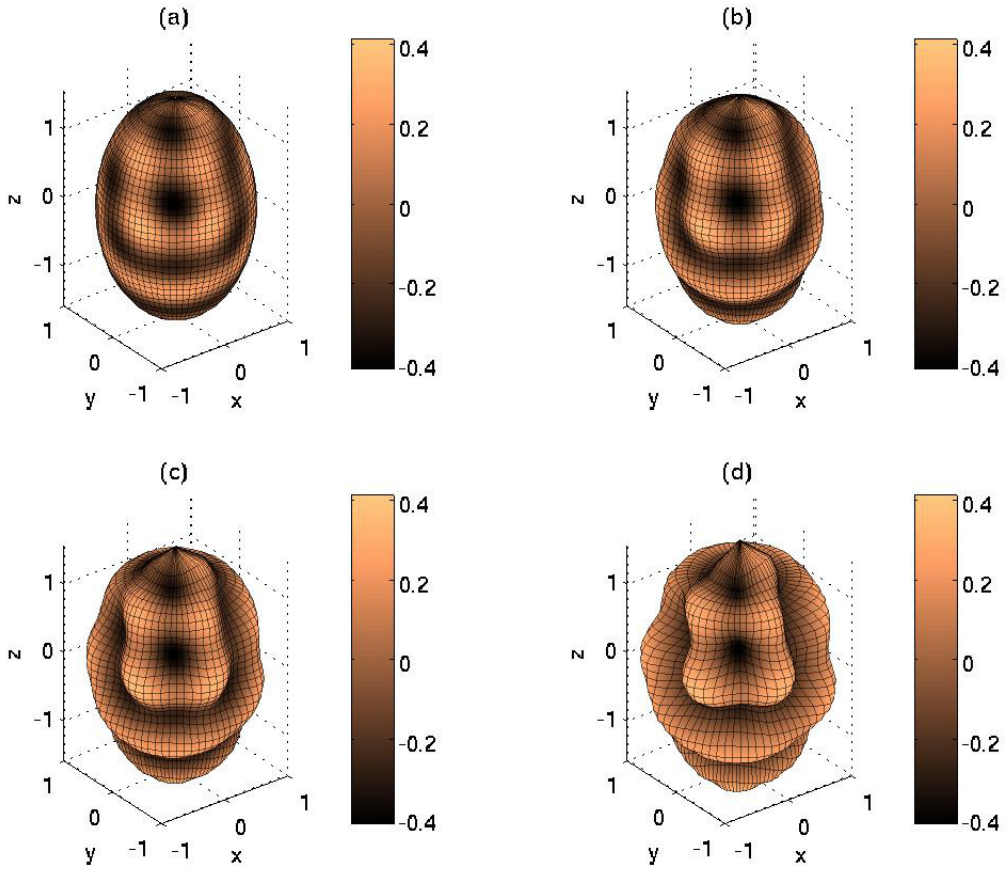


Figure B.30: Prolate spheroid visualization of logistically growing domain Turing prepattern for Norman-Roberts Syndrome with non-enlarged lateral ventricles. Projecting the images from Figure B.29 onto the corresponding prolate spheroidal domain gives a new way to visualize how a labyrinthine pattern representing NRS with non-enlarged LVs could develop from a chemical Turing prepattern (refer to Figure B.28 at $t = 35$). See also: animation.

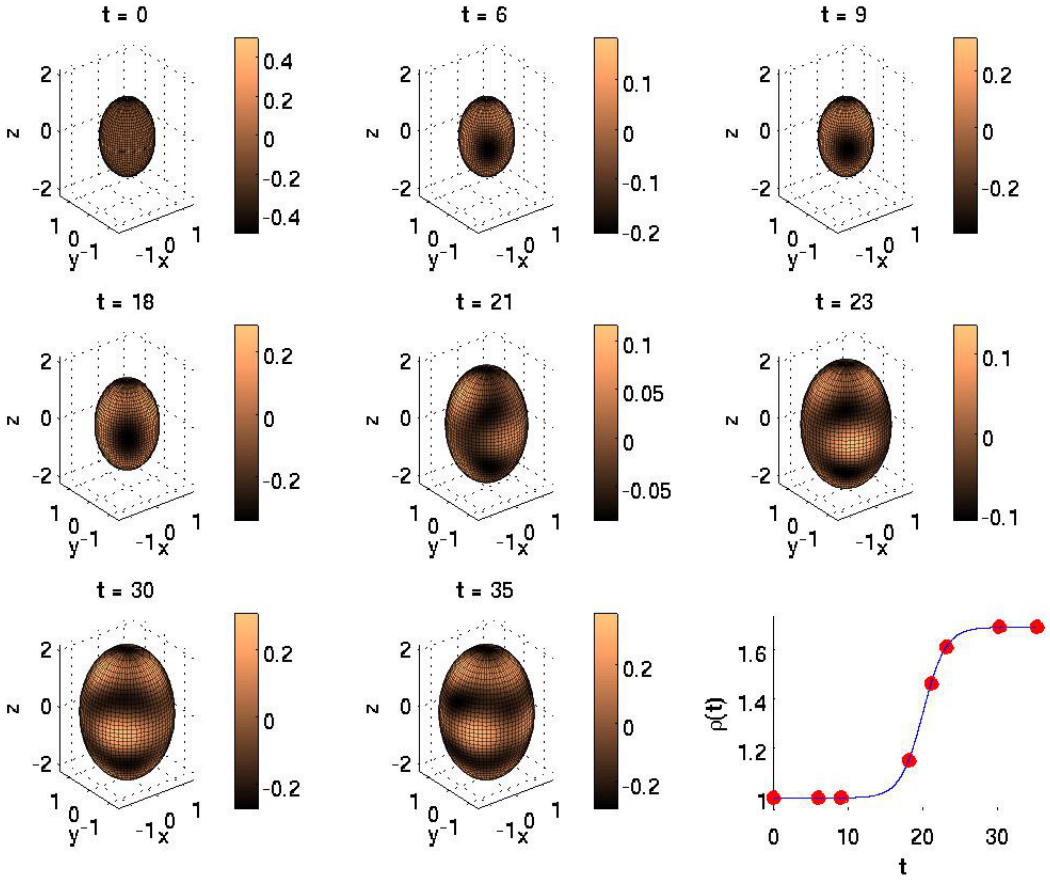


Figure B.31: Evolution of Turing pattern on a logistically growing prolate spheroid representing the lissencephaly presented in Norman-Roberts Syndrome with enlarged lateral ventricles. The pattern was generated by System (5.5) with $R = 0.015, \omega = 30, t_{\text{final}} = 35, r = 0.6603, t_0 = 19.9258, K^\star = e^{Rt_{\text{final}}} - 1$ and kinetics parameters listed on page 34. Dots in the bottom right figure correspond to the time at which each snapshot was taken. See also: animation.

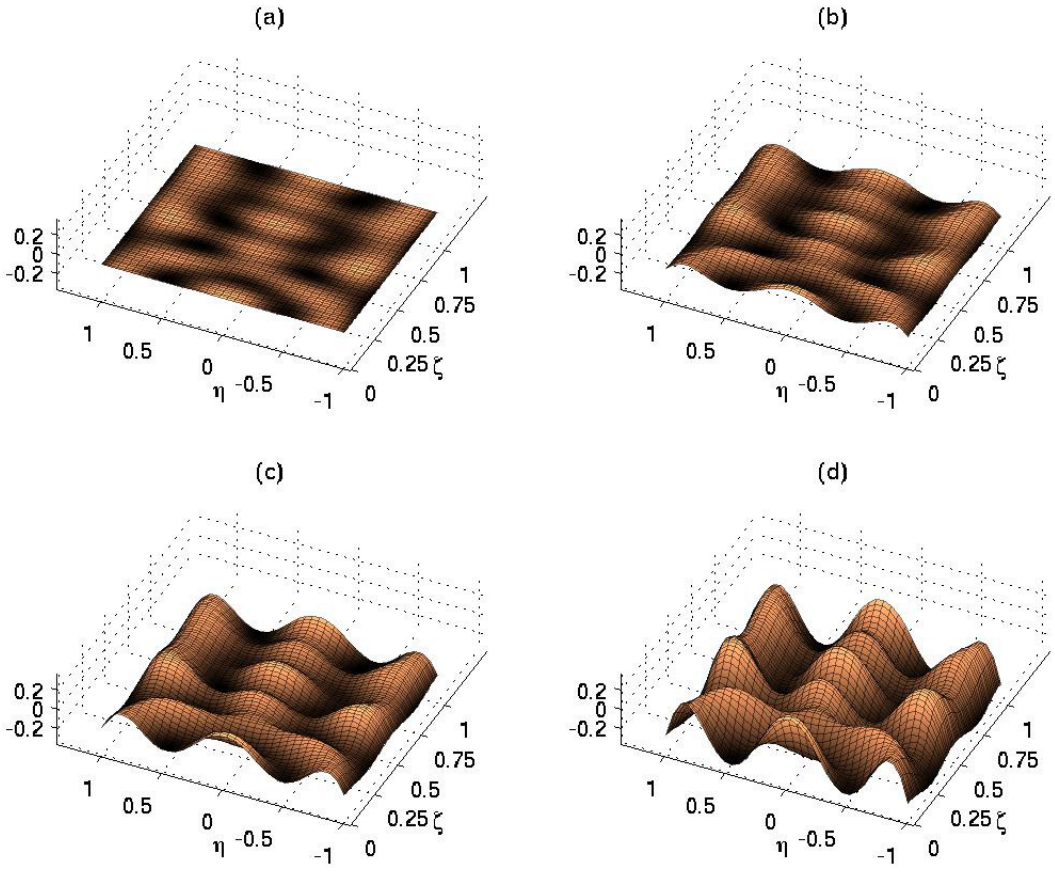


Figure B.32: Logistically growing domain Turing pattern as a prepattern for Norman-Roberts Syndrome with enlarged lateral ventricles. Figures (a) through (d) provide a visualization of how a labyrinthine cortical folding pattern could develop from a genetic chemical Turing prepattern by plotting the activator concentration $u$ on the $z$-axis for $z = 0$, $z = \frac{u}{4}$, $z = \frac{u}{2}$, and $z = u$, respectively. The pattern represents NRS with enlarged LVs and corresponds to the final pattern in Figure B.31. See also: animation.

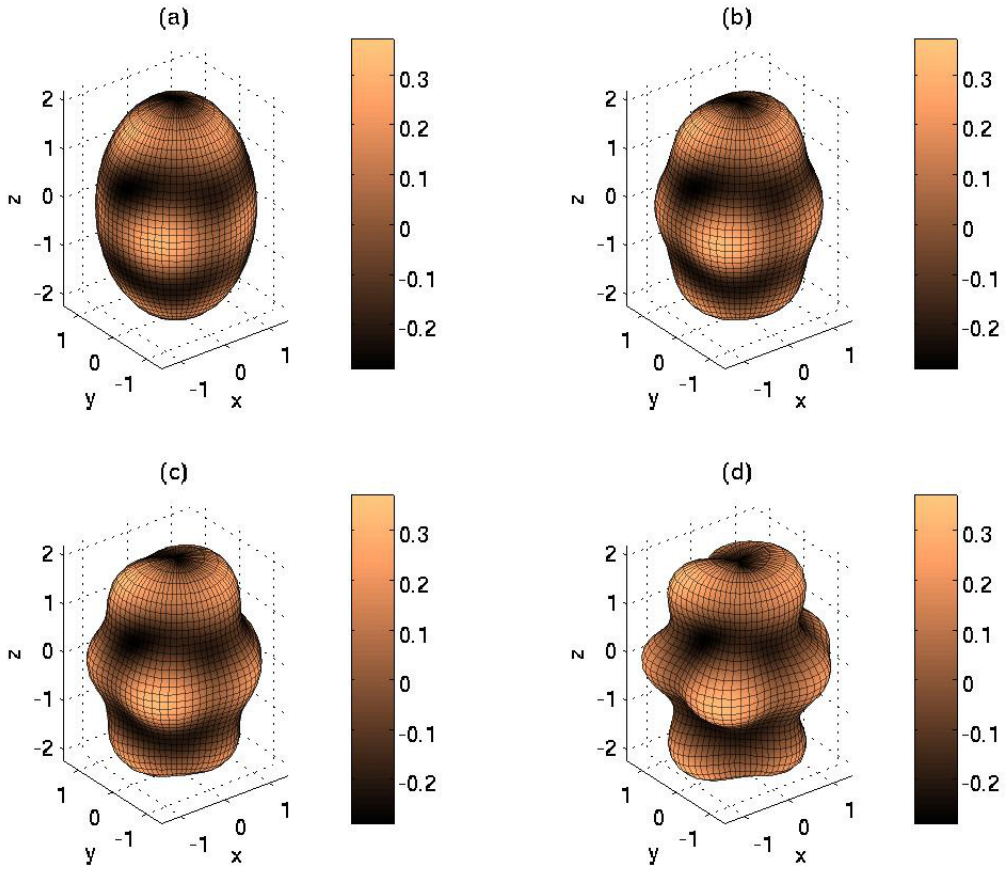


Figure B.33: Prolate spheroid visualization of logistically growing domain Turing prepattern for Norman-Roberts Syndrome with enlarged lateral ventricles. Projecting the images from Figure B.32 onto the corresponding prolate spheroidal domain gives a new way to visualize how a labyrinthine pattern representing NRS with enlarged LVs could develop from a chemical Turing prepattern (refer to Figure B.31 at $t = 35$). See also: animation.

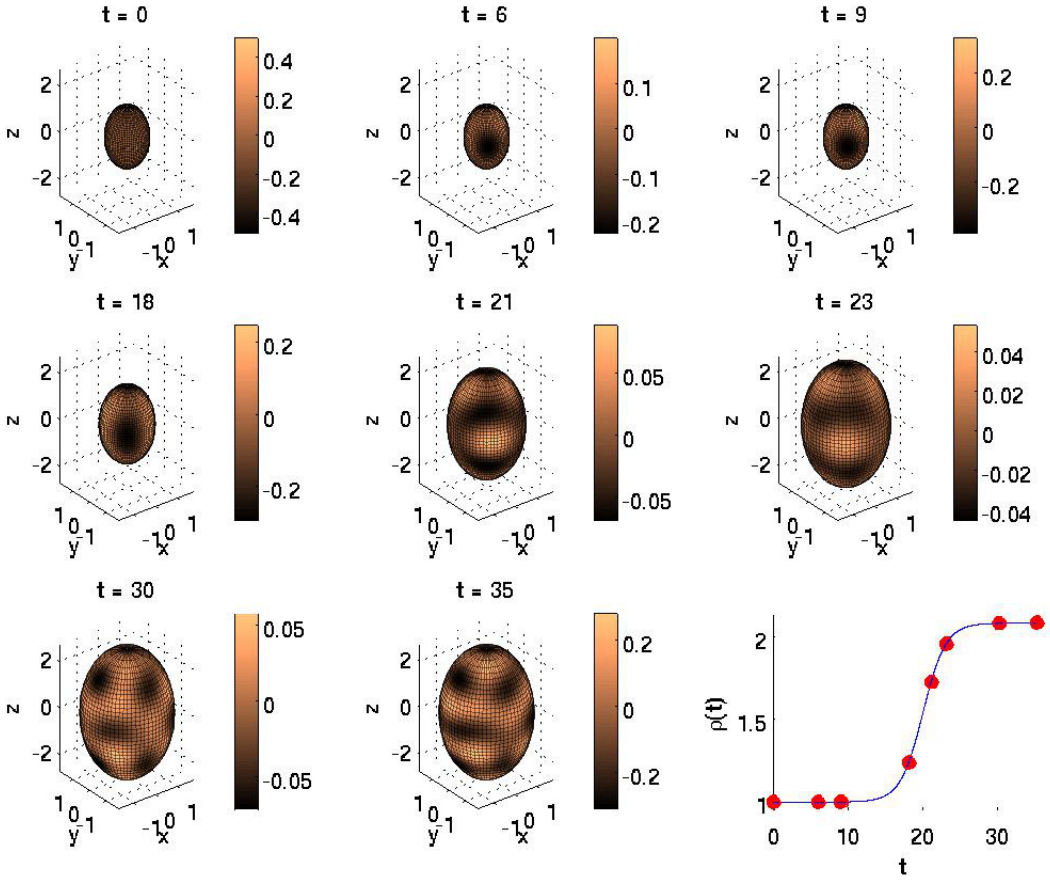


Figure B.34: Evolution of Turing pattern on a logistically growing prolate spheroid representing normocephalic type I lissencephaly with enlarged lateral ventricles. The pattern was generated by System (5.5) with $R = 0.021, \omega = 30, t_{\text{final}} = 35, r = 0.6603, t_0 = 19.9258, K^\star = e^{Rt_{\text{final}}} - 1$ and kinetics parameters listed on page 34. Dots in the bottom right figure correspond to the time at which each snapshot was taken. See also: animation.

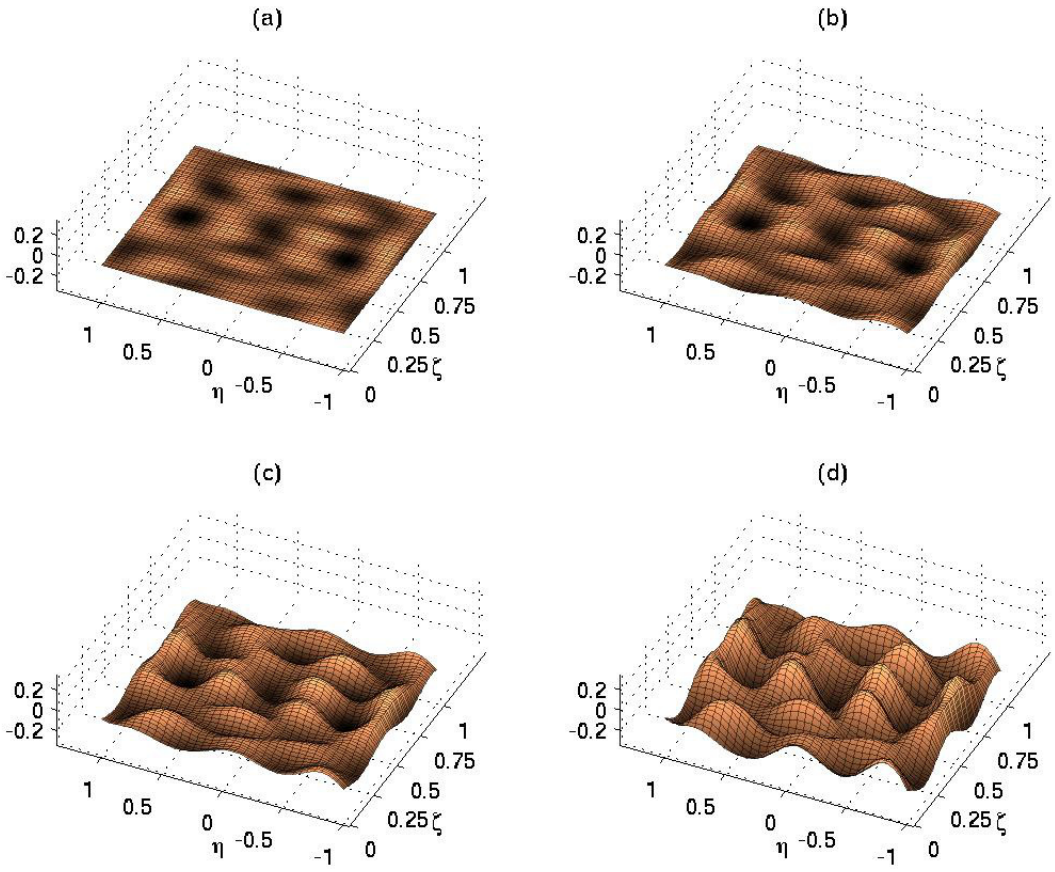


Figure B.35: Logistically growing domain Turing pattern as a prepattern for non-microcephalic type I lissencephaly with enlarged lateral ventricles. Figures (a) through (d) provide a visualization of how a labyrinthine cortical folding pattern could develop from a genetic chemical Turing prepattern by plotting the activator concentration $u$ on the $z$-axis for $z = 0$, $z = \frac{u}{4}$, $z = \frac{u}{2}$, and $z = u$, respectively. The pattern represents normocephalic type I lissencephaly with enlarged LVs and corresponds to the final pattern in Figure B.34. See also: animation.

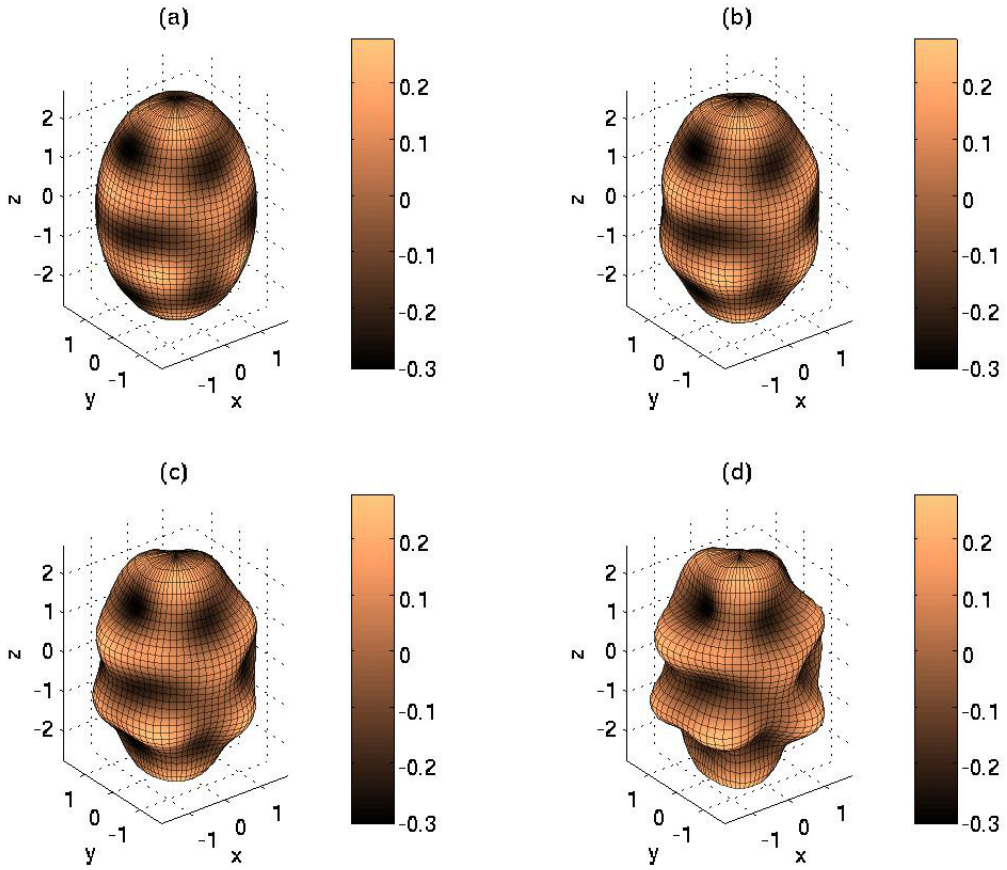


Figure B.36: Prolate spheroid visualization of logistically growing domain Turing prepattern for normocephalic type I lissencephaly with enlarged lateral ventricles. Projecting the images from Figure B.35 onto the corresponding prolate spheroidal domain gives a new way to visualize how a labyrinthine pattern representing normocephalic type I lissencephaly with enlarged LVs could develop from a chemical Turing prepattern (refer to Figure B.34 at $t = 35$). See also: animation.

# REFERENCES


[1] M. Akam. Making stripes inelegantly. *Nature*, 341:282–283, 1989. 3.1.2

[2] J.A. Anstrom, C.R. Thore, D.M. Moody, V.R. Challa, S.M. Block, and W.R. Brown. Germinal matrix cells associate with veins and a glial scaffold in the human fetal brain. *Dev Brain Res*, 160:96–100, 2005. 2.1.3

[3] H. Baier and F. Bonhoeffer. Attractive axon guidance molecules. *Science*, 265:1541–1542, 1994. 2.3.2

[4] A.J. Barkovich. Current concepts of polymicrogyria. *Neuroradiology*, 52:479–487, 2010. 6, 6.3.1, 6.3

[5] A.J. Barkovich, R.I. Kuzniecky, G.D. Jackson, R. Guerrini, and W.B. Dobyns. A developmental and genetic classification for malformations of cortical development. *Neurology*, 65:1873–1887, 2005. 6.3.2, 6.3.2

[6] I. Barrass, E.J. Crampinn, and P.K. Maini. Mode transitions in a model reactiondiffusion system driven by domain growth and noise. *B Math Biol*, 68:981–995, 2006. 3.1.3

[7] R.A. Barrio. Turing systems: A general model for complex patterns in nature. *Electron J Theor Phys*, 4(15):1–26, 2007. 3.2

[8] R.A. Barrio, R.E. Baker, B. Vaughan, K. Tribuzy, M.R. deCarvalho, R. Bassanezi, and P.K. Maini. Modeling the skin pattern of fishes. *Phys Rev E*, 79(3):031908–1–031908–11, 2009. 4.3

[9] R.A. Barrio, C. Varea, J.L. Aragon, and P.K. Maini. A two-dimensional numerical study of spatial pattern formation in interacting Turing systems. *B Math Biol*, 61(3):483–505, 1999. 3.1.3, 3.2, 4.2, 4.3, A.3, A.3

[10] H.G. Blaas, S.H. Eik-Nes, T. Kiserud, and L.R. Hellevik. Early development of the hindbrain: a longitudinal ultrasound study from 7 to 12 weeks of gestation. *Ultrasound Obst Gyn*, 5:151–160, 1995. 6.2.1

[11] H. Caksen, O. Tuncer, E. Kirimi, J.P. Fryns, A. Uner, O. Unal, A. Cinal, and D. Odabas. Report of two Turkish infants with Norman-Roberts syndrome. *Genet Counsel*, 15(1):9–17, 2004. 6.3.2, 6.10

[12] R.S. Cantrell and C. Cosner. The effects of spatial heterogeneity in population dynamics. *J Math Biol*, 29:315–338, 1991. 5

[13] J.H.E. Cartwright. Labyrinthine Turing pattern formation in the cerebral cortex. *J Theor Biol*, 217:97–103, 2002. 1, 2.3, 2.3.2, 2.15, 6.1, 6.5

[14] V. Castets, E. Dulos, J. Boissonade, and P. Dekepper. Experimental evidence of a sustained Turing-type nonequilibrium chemical pattern. *Phys Rev Lett*, 64(24):2953–2956, 1990. 3.1.3

[15] B.S. Chang, X. Piao, A. Bodell, L. Basel-Vanagaite, R. Straussberg, W.B. Dobyns, B. Qasrawi, R.M. Winter, A.M. Innes, T. Voit, P.E. Grand, A.J. Barkovich, and C.A. Walsh. Bilateral frontoparietal polymicrogyria: Clinical and radiological features in 10 families with linkage to chromosome 16. *Ann Neurol*, 53:596–606, 2003. 6.3.1, 6.3.1, 6.3

[16] M.A.J. Chaplain, M. Ganesh, and I.G. Graham. Spatio-temporal pattern formation on spherical surfaces: numerical simulation and application to solid tumour growth. *J Math Biol*, 42:387–423, 2001. 4.3, 4.4, 6.1, 7.1

[17] M. Colombani, M. Chouchane, G. Pitelet, L. Morales, P. Callier, J.P. Pinard, L. Lion-Francois, C. Thauvin-Robinet, F. Mugneret, F. Huet, L. Guibaud, and L. Faivre. A new case of megalencephaly and perisylvian polymicrogyria with post-axial polydactyly and hydrocephalus: MPPH syndrome. *Eur J Med Genet*, 49:466–471, 2006. 6.3.1, 6.3

[18] L. Dalton. Biological evidence for Turing patterns. *Biomed Comput Rev*, 3(2):2–3, 2007. 3

[19] J. Dubois, M. Benders, A. Cachia, F. Lazeyras, R. Ha-Vinh-Leuchter, S.V. Sizonenko, C. Borradori-Tolsa, J.F. Mangin, and P.S. Huppi. Mapping the early cortical folding process in the preterm newborn brain. *Cereb Cortex*, 18:1444–1454, 2008. 2.6, 2.1.3

[20] I.R. Epstein and I. Lengyel. Turing structures. Progress toward a room temperature, closed system. *Physica D*, 84:1–11, 1995. 3

[21] B. Ermentrout. Stripes or spots? Nonlinear effects in bifurcation of reaction-diffusion equations on the square. *P Roy Soc Lond A Mat*, 434(1891):413–417, 1991. 3.2, 4.3, A.3

[22] D.C. Van Essen. A tension-based theory of morphogenesis and compact wiring in the central nervous system. *Nature*, 385(6614):313–318, 1997. 1, 2.2, 2.2.4, 2.14, 7.2

[23] R.A. FitzHugh. Thresholds and plateaus in the Hodgkin-Huxley nerve equations. *J Gen Physiol*, 43:867–896, 1960. 2.3.2

[24] R.A. FitzHugh. Impluses and physiological states in theoretical models of nerve membrane. *Biophys J*, 1:445–466, 1961. 2.3.2

[25] K. Flammer. *Spheroidal Wave Functions*. Stanford University Press, Palo Alto, 1957. 3.3, A.5, A.5, A.5, A.2

[26] The Endowment for Human Development. The endowment for human development, 2010. URL: http://www.ehd.org/prenatal-images-index.php [Last accessed: February 17, 2010]. 2.1.2, 2.3, 6.1, 6.1

[27] C. Freudenrich. How your brain works. URL: http://www.howstuffworks.com /brain.htm [Last accessed: January 18, 2010]. 2.2, 2.7

[28] C. Garel, E. Chantrel, H. Brisse, M. Elmaleh, D. Luton, J.F. Oury, G. Sebag, and M. Hassan. Fetal cerebral cortex: Normal gestational landmarks identified using prenatal MR imaging. *Am J Neuroradiol*, 22:184–189, 2001. 1, 2.6, 2.1.3

[29] G. Geng, L.A. Johnston, E. Yan, J.M. Britto, D.W. Smith, D.W. Walker, and G.F. Egan. Biomechanisms for modelling cerebral cortical folding. *Med Image Anal*, 13(6):920–930, 2009. 2.3, 2.18, 2.3.5, 6.5

[30] P.A. Georgala, C.B. Carr, and D.J. Price. The role of Pax6 in forebrain development. *Dev Neurobiol*, 71(8):690–709, 2011. 2.1.1

[31] A. Gierer and H. Meinhardt. A theory of biological pattern formation. *Kybernetik*, 12:30–39, 1972. 3.1

[32] J. Gjorgjieva and J. Jacobsen. Turing patterns on growing spheres: The exponential case. *Discrete Cont Dyn S Suppl 2007*, pages 436–445, 2007. 4.1, 4.3, 7.1

[33] O.A. Glenn. Normal development of the fetal brain by MRI. *Semin Perinatol*, 33:208–219, 2009. 2.1.3

[34] G.J. Goodhill and J.S. Urbach. Theoretical analysis of gradient detection by growth cones. *J Neurobiol*, 41:230–241, 1999. 2.3.2

[35] R. Guerrini and C. Marini. Genetic malformations of cortical development. *Exp Brain Res*, 173:322–333, 2006. 2.1.3, 2.6, 6.3.1

[36] P.E. Hansen, M.C. Ballesteros, K. Soila, L. Garcia, and J.M. Howard. MR imaging of the developing human brain. Part 1. Prenatal development. *Radiographics*, 13:21–36, 1993. 6.1, 6.2.1

[37] C.C. Hilgetag and H. Barbas. Role of mechanical factors in the morphology of the primate cerebral cortex. *PLoS Comput Biol*, 2(3):146–159, 2006. 2.2.4

[38] M. Hill. UNSW embryology, 2009. URL: http://embryology.med.unsw.edu.au/Notes /neuron5.htm [Last accessed: February 17, 2010]. 2.1.2, 2.3, 6.1, 6.1

[39] S.E. Hong, Y.Y. Shugart, D.T. Huang, S. Al Shahwan, P.E. Grant, J.O'B. Hourihane, N.D.T. Martin, and C.A. Walsh. Autosomal recessive lissencephaly with cerebellar hypoplasia is associated with human RELN mutations. *Nat Genet*, 26:93–96, 2000. 6.3.2

[40] Seattle Children's Hospital. Hydrocephalus, 2013. URL: www.seattlechildrens.org/medical-conditions/chromosomal-genetic-conditions/hydrocephalus [Last accessed: March 22, 2013]. 6.3

[41] J. Hsia, W.J. Holtz, D.C. Huang, M. Arcak, and M.M. Maharbiz. A feedback quenched oscillator produces Turing patterning with one diffuser. *PLoS Comput Biol*, 8(1):e1002331, 2012. 3

[42] M.K. Hurdal and D.A. Striegel. Modelling cortical folding pattern formation of the brain with a Turing system. *18th World IMACS/MODSIM Congress*, pages 664–670, 2009. 2.3.1

[43] J. Jacobsen. Personal communication, July 27, 2011. 4.3

[44] Y. Kinoshita, T. Okudera, E. Tsuru, and A. Yokota. Volumetric analysis of the germinal matrix and lateral ventricles performed using MR images of postmortem fetuses. *Am J Neuroradiol*, 22:382–388, 2001. 2.1.3, 2.4, 2.5, 2.6, 5.1, 5.1, 6.2.2

[45] A. Kriegstein, S. Noctor, and V. Martinez-Cerdeno. Patterns of neural stem and progenitor cell division may underlie evolutionary cortical expansion. *Nat Rev Neurosci*, 7(11):883–890, 2006. 1, 2.1.2, 2.1.3, 2.6, 2.2, 2.2.1, 2.9, 2.10, 2.2.3, 2.13, 7.1, 7.3

[46] P.M. Kulesa, G.C. Cruywagen, S.R. Lubkin, P.K. Maini, J. Sneyd, M.W.J. Ferguson, and J.D. Murray. On a model mechanism for the spatial patterning of teeth primordia in the alligator. *J Theor Biol*, 180:287–296, 1996. 5

[47] J. Lefevre and J.F. Mangin. A reaction-diffusion model of human brain development. *PLoS Comput Biol*, 6(4):e1000749, 2010. 2.6, 2.1.3, 2.3.3, 2.16, 6.2.1, 6.5, 7.2

[48] T. Leppänen. *Spatial Pattern Formation in Turing Systems*. Master's thesis, Helsinki University of Technology, 2003. A.3

[49] T. Leppänen. *Computational Studies of Pattern Formation in Turing Systems*. PhD thesis, Helsinki University of Technology, 2004. 4.3, A.3

[50] T. Leppänen, M. Karttunen, R.A. Barrio, and K. Kaski. Morphological transitions and bistability in Turing systems. *Phys Rev E*, 70:066202, 2004. 4.3

[51] K. Letinic, Z. Zoncu, and P. Rakic. Origin of GABAergic neurons in the human neocortex. *Nature*, 417:645–649, 2002. 2.1.3, 2.6

[52] R.J. Leventer, R. Guerrini, and W.B. Dobyns. Malformations of cortical development and epilepsy. *Dialogues Clin Neurosci*, 10:47–62, 2008. 6.3.2

[53] D.C. Lie, S.A. Colamarino, H.J. Song, L. Desire, H. Mira, A. Consiglio, E.S. Lein, S. Jessberger, H. Lansford, A.R. Dearie, and F.H. Gage. *Wnt* signalling regulates adult hippocampal neurogenesis. *Nature*, 437:1370–1375, 2005. 2.2.3

[54] A. Madzvamuse. Stability analysis of reaction-diffusion systems with constant coefficients on growing domains. *Int J Dyn Diff Eqn*, 1(4):250–262, 2008. 3.2

[55] P. Maini. Mathematical models in morphogenesis. In V. Capasso and O. Diekmann, editors, *Mathematics Inspired by Biology*, pages 151–189. Springer, Martina Franca, Italy, 1997. 3.1.3, A.1

[56] P.K. Maini. Personal communication, October 21, 2010. A.3

[57] P.K. Maini, R.E. Baker, and C.M. Chuong. The Turing model comes of molecular age. *Science*, 314:1397–1398, 2006. 3.1.1, 3.1.2

[58] P.K. Maini, T.E. Woolley, R.E. Baker, E.A. Gaffney, and S.S. Lee. Turing's model for biological pattern formation and the robustness problem. *Interface Focus*, 2:487–496, 2012. 3.1.3

[59] J.F. Mangin, E. Jouvent, and A. Cachia. In-vivo measurement of cortical morphology: means and meanings. *Curr Opin Neurol*, 23:359–367, 2010. 2.6, 2.1.3

[60] D.G. Meyers. *Psychology*. Worth, New York, 2006. 2.1

[61] K.W. Morton and D.F. Mayers. *Numerical Solution of Partial Differential Equations: An Introduction*. Cambridge, Cambridge, UK, 2nd edition, 2005. 4.3

[62] J.D. Murray. How the leopard gets its spots. *Sci Am*, 258(3):80–87, 1988. 3.1.1, 6.1, 7.3

[63] J.D. Murray. *Mathematical Biology II*. Springer, New York, 3rd edition, 2003. 3, 3.1, 3.1.1, 3.2, 4.1.3, 5, 6.1, 7.3, A.1, A.2, A.3

[64] J.S. Nagumo, S. Arimoto, and S. Yoshizawa. An active pulse transmission line simulating nerve axon. *Proc IREE Aust*, 50:2061–2070, 1962. 2.3.2

[65] F. Natacci, M.F. Bedeschi, A. Righini, F. Inverardi, T. Rizzuti, C. Boschetto, F. Triulzi, R. Spreafico, C. Frassoni, and F. Lalatta. Norman-Roberts syndrome: Characterization of the phenotype in early fetal life. *Prenatal Diag*, 27:568–572, 2007. 6, 6.3.2, 6.3.2, 6.9

[66] S.C. Noctor, V. Martinez-Cerdeno, L. Ivic, and A.R. Kriegstein. Cortical neurons arise in symmetric and asymmetric division zones and migrate through specific phases. *Nat Neurosci*, 7(2):136–144, 2004. 2.1.2, 2.1.4, 2.2.2

[67] J. Nolte. *The Human Brain: An Introduction to its Functional Anatomy*. Mosby, St. Louis, 5th edition, 2002. 2.1.4

[68] M.G. Norman, M. Roberts, J. Sirois, and L.J.M. Tremblay. Lissencephaly. *Can J Neurol Sci*, 3:39–46, 1976. 6, 6.3.2

[69] University of Wisconsin and Michigan State Comparative Mammalian Brain Collections. Comparative mammalian brain collections. URL: http://www.brainmuseum.org/ [Last accessed: February 17, 2010]. 2.1

[70] I. Pascual-Castroviejo, S.I. Pascual-Pascual, J. Viano, V. Martinez, and R. Palencia. Unilateral polymicrogyria: A common cause of hemiplegia of prenatal origin. *Brain Dev-Jpn*, 23:216–222, 2001. 6.3.1, 6.3

[71] X. Piao, R.S. Hill, A. Bodell, B.S. Chang, L. Basel-Vanagaite, R. Straussberg, W.B. Dobyns, B. Qasrawi, R.M. Winter, A.M. Innes, T. Voit, M.E. Ross, J.L. Michaud, J.C. Descarie, A.J. Barkovich, and C.A. Walsh. G protein-coupled receptor-dependent development of human frontal cortex. *Science*, 303:2033–2036, 2004. 6.3.1, 6.3.1

[72] R.G. Plaza, F. Sanchez-Garduno, P. Padilla, R.A. Barrio, and P.K. Maini. The effect of growth and curvature on pattern formation. *J Dyn Differ Equ*, 16(4):1093–1121, 2004. 3.2, A.1, A.2

[73] A. Pontious, T. Kowalczyk, C. Englund, and R.F. Hevner. Role of intermediate progenitor cells in cerebral cortex development. *Dev Neurosci-Basel*, 30:24–32, 2008. 2.2.2, 2.2.3, 7.2

[74] P. Rakic. Specification of cerebral cortical areas. *Science*, 241(4862):170–176, 1988. 2.1.2, 2.2.1, 2.2.1

[75] P. Rakic. A small step for the cell, a giant leap for mankind — a hypothesis of neocortical expansion during evolution. *Trends Neurosci*, 18:383–388, 1995. 2.1.2, 2.1.3, 2.6, 2.1.4, 2.2.1, 6.1

[76] P. Rakic. Developmental and evolutionary adaptations of cortical radial glia. *Cereb Cortex*, 13(6):541–549, 2003. 2.8, 2.1.4

[77] P. Rakic. Less is more: Progenitor death and cortical size. *Nat Neurosci*, 8(8):981–982, 2005. 2.2.1, 7.2

[78] J. Schakenberg. Simple chemical reaction systems with limit cycle behaviour. *J Theor Biol*, 81(3):389–400, 1979. 3.1.3

[79] C. Sergi, S Zoubaa, and M Schiesser. Norman-Roberts syndrome: Prenatal diagnosis and autopsy findings. *Prenatal Diag*, 20:505–509, 2000. 6, 6.3.2, 6.3.2

[80] L. Sherwood. *Human Physiology: From Cells to Systems*. Thomson Brooks/Cole, Belmont, 5th edition, 2004. 2.1, 2.1.1, 2.1.2, 2.1.4

[81] H. Shiratori and H. Hamada. The left-right axis in the mouse: from origin to morphology. *Development*, 133:2095–2104, 2006. 3.1.3

[82] S. Sick, S. Reinker, J. Timmer, and T. Schlake. Hair follicle spacing through a reaction-diffusion mechanism. *Science*, 314:1447–1450, 2006. 3.1, 3.1.2

[83] J. Stewart. *Calculus: Early Transcendentals*. Thomson, Belmont, 6th edition, 2008. A.1.1

[84] W.A. Strauss. *Partial Differential Equations: An Introduction*. John Wiley & Sons, New York, 1st edition, 1992. A.1.2, A.2.1

[85] D.A. Striegel. *Modeling the Folding Pattern of the Cerebral Cortex*. PhD thesis, Florida State University, 2009. 2.3.1, A.3, A.5

[86] D.A. Striegel and M.K. Hurdal. Chemically based mathematical model for development of cerebral cortical folding patterns. *PLoS Comput Biol*, 5(9):e1000524, 2009. 1, 2.3, 2.3.1, 4.3, 4.4, 6.1, 6.1, 6.5, 7.1

[87] L. Sztriha and M. Nork. Bilateral frontoparietal polymicrogyria and epilepsy. *Pediatr Neurol*, 22:240–243, 2000. 6.3.1

[88] M. Tessier-Lavigne and C.S. Goodman. The molecular biology of axon guidance. *Science*, 274:1123–1133, 1996. 2.3.2

[89] D. Thomas. Artificial enzyme membranes, transport, memory, and oscillatory phenomena. In D. Thomas and J.P. Kernevez, editors, *Analysis and Control of Immobilized Enzyme Systems*, pages 115–150. Springer, New York, 1975. 3.1.3

[90] G. Toole and M.K. Hurdal. Growth in a Turing model of cortical folding. *Biomath*, 1:1209252, 2012. 4, 4.3, 6, 6.2.1

[91] G. Toole and M.K. Hurdal. Turing models of cortical folding on exponentially and logistically growing domains. *Computers and Mathematics with Applications*, accepted 2013. 4, 5, 6

[92] G. Toole and M.K. Hurdal. Turing systems on an exponentially growing domain. *J Dyn Differ Equ*, in submission. 4

[93] R. Toro and Y. Burnod. A morphogenetic model for the development of cortical convolutions. *Cereb Cortex*, 15:1900–1913, 2005. 2.17, 2.3.4, 6.5

[94] P Tracqui, G.C. Cruywagen, D.E. Woodward, G.T. Bartoo, J.D. Murray, and E.C. Alvord Jr. A mathematical model of glioma growth: The effect of chemotherapy on spatio-temporal growth. *Cell Proliferat*, 28:17–31, 1995. 5

[95] A.M. Turing. The chemical basis of morphogenesis. *Philos T Roy Soc B*, B 237:37–72, 1952. 3, 3.1, 3.1.3, 6.1, 7.3

[96] B. van der Pol and J. van der Mark. The heart beat considered as a relaxation oscilation, and an electrical model of the heart. *Philos Mag*, 6(38):763–775, 1928. 2.3.2

[97] C. Varea, J.L. Aragon, and R.A. Barrio. Turing patterns on a sphere. *Phys Rev E*, 60(4):4588–4592, 1999. 4.3, 7.2

[98] C. Varea, D. Hernandez, and R.A. Barrio. Soliton behaviour in a bistable reaction diffusion model. *J Math Biol*, 54:797–813, 2007. 3.2

[99] C. Venkataraman, T. Sekimura, E.A. Gaffney, P.K. Maini, and A. Madzvamuse. Modeling parr-mark pattern formation during the early development of Amago trout. *Phys Rev E*, 84:041923, 2011. 4.3

[100] J. Wei and M. Winter. Flow-distributed spikes for schnakenberg kinetics. *J Math Biol*, 64:211–254, 2012. 3.1.3

[101] E.W. Weisstein. Eccentricity. URL: http://mathworld.wolfram.com/Eccentricity.html [Last accessed: February 25, 2013]. A.5

[102] E.W. Weisstein. Prolate spheroidal coordinates. URL: http://mathworld.wolfram.com/ProlateSpheroidalCoordinates.html [Last accessed: February 25, 2013]. A.5, A.5

[103] N. Zecevic, Y. Chen, and R. Filipovic. Contributions of cortical subventricular zone to the development of the human cerebral cortex. *J Comp Neurol*, 491:109–122, 2005. 2.1.3, 2.6

[104] S. Zeki. *Vision of the Brain*. Wiley, Hoboken, 1993. 2.1

# BIOGRAPHICAL SKETCH

Gregory Toole grew up in Washington Township, New Jersey, a New York City suburb in the northeastern part of the state. After graduating from Westwood High School in 2004, he attended college at the University of Scranton. Gregory graduated summa cum laude in 2008 with a Bachelor's degree in Biomathematics and minors in Spanish, Mathematics, and Biology, earning the Excellence in Biomathematics award for his graduating class. Gregory then attended graduate school at Florida State University, where he received the University Fellowship, College of Arts & Sciences Teaching Fellowship, and the Department of Mathematics Distinguished Teaching Assistant Award. He earned his Master's degree in Mathematics in 2010 and his doctorate in Mathematics in 2013, both under the advisement of Dr. Monica K. Hurdal.